

Mode-locked Pulses in Passive Coherent Beam Combining Fiber Laser Arrays

by

Chao Zhang

A dissertation submitted in partial fulfillment
of the requirements for the degree of
Doctor of Philosophy
(Electrical Engineering)
in The University of Michigan
2013

Doctoral Committee:

Professor Herbert G. Winful, Chair
Professor Almantas Galvanauskas
Professor Peter D. Miller
Professor Stephen C. Rand

© Chao Zhang 2013

For my family and friends

ACKNOWLEDGEMENTS

First, I would like to express my deepest respect and gratitude to my advisor, Professor Herbert G. Winful, for his crucial guidance over my Ph.D. years. Through his constructive support and rigorous academic attitude, I have learned how to grow as a professional researcher. As an expert in setting the correct pace for students in their research progress, he always inspires me great ideas at the key milestones. Without his patient assistance, I would not have chance to explore diverse topics and thoughts while digging into the cores of the problems. I want to extend my appreciation for his friendly smiles, making me more confident in both research and life.

My special thanks also go to Professor Almantas Galvanauskas, for his invaluable advice and feedback on my project from multiple aspects, which have motivated my research work stepping farther and deeper in physical insights. I would like to thank Professor Stephen C. Rand for his continuous encouragement and accessible affability every time we talk about research, teaching, or life. I would like to express gratitude to Professor Peter D. Miller for contributing helpful discussions regarding to my research and thesis.

I would like to sincerely thank Dr. Tsai-wei Wu for many inspiring suggestions on simulation coding and thank Dr. Wei-zung (Wayne) Chang for long time discussions on experimental applications. They are more than research collaborators, but also mentors assisting me on the growth my professional development. I am also indebted to I-Ning Hu and Cheng Zhu for all the collaboration and effective discussions in the

research.

I enjoy my teaching life a lot as the Graduate Student Instructor in 7 semesters in Department of Electrical Engineering and Computer Science. I am extremely grateful to Professor Winful, Professor Rand, Professor Fawazz Ulaby, Professor Mark Kushner, Professor Anthony Grbic, Professor Mahta Moghaddam and Professor Wei Lu who I have cooperated with in my teaching. From them I learned from the professional academic skills, practical and flexible teaching methods, to their high devotion to duty.

I wish to thank all my friends in and outside Ann Arbor who had accompanied me through all these years. I really cherish and appreciate their friendships. I would like to specially thank Dr. Hongwei Liao, Dr. Sung-Liang Chen, Dr. Chenji Gu, Dr. Xiwen Zhang, Yue Zhang and Ming Lin for their invaluable advice on my academic and professional development.

Last but not the least, I appreciate the unconditional love and endless support from my family. No matter what kind of difficulties and challenges I have in my life, they always provide the greatest strength giving me confidence and encouragement.

TABLE OF CONTENTS

DEDICATION	ii
ACKNOWLEDGEMENTS	iii
LIST OF FIGURES	viii
LIST OF TABLES	xiii
CHAPTER	
I. Introduction	1
1.1 Background review on high power pulses in fiber lasers	1
1.2 Thesis Outline	4
II. Mode-Locking in Passive Coherent Beam Combining	8
2.1 Introduction	8
2.2 Background on passive coherent beam combining	9
2.2.1 Array structures of fiber laser cavities	10
2.2.2 The dynamical model for passive coherent beam combining	13
2.2.3 Array modes and spectral beating	15
2.2.4 Coherent beam combining results in cw operation	18
2.3 Background on mode locking	19
2.3.1 Active and passive mode locking	20
2.3.2 Saturable absorber modeling	24
2.3.3 Simulation results for a single fiber laser	26
2.4 Simultaneous beam combining and mode locking	27
2.4.1 Linear model	27
2.4.2 Comparison with experimental results	30
2.5 Influence of nonlinearity	34
2.6 Four-channel beam combining	35
2.6.1 CW operation	37

2.6.2	Four-channel beam combining and mode locking in fibers with incommensurate or commensurate lengths	38
2.6.3	Combining efficiency in four channel beam combining	41
2.7	Conclusion	46
III.	Dissipative Solitons in Fiber Laser Array With Normal Dispersion	47
3.1	Introduction	47
3.2	Theory of dissipative solitons	49
3.2.1	Solitons and dissipative solitons	49
3.2.2	Wave breaking	51
3.2.3	Comparison with similaritons	52
3.3	Quantitative model of dissipative solitons	54
3.3.1	Cubic-quintic complex Ginzburg-Landau equation	54
3.3.2	Nonlinear Schrödinger equation	55
3.3.3	Simulation result for a single Yb-doped fiber laser	57
3.4	Dissipative solitons in fiber laser arrays	59
3.4.1	Comparisons between positive and negative GVD	61
3.4.2	Effects of nonlinearity	62
3.5	Pulse train operation	64
3.5.1	Pulse repetition rate	65
3.5.2	Frequency Comb	67
3.5.3	A new approach to a robust pulse train with high repetition rate	68
3.5.4	Discussion on the results	71
3.6	Conclusion	73
IV.	Tunneling in Directional Couplers [138]	74
4.1	Introduction	74
4.2	Power distribution in directional couplers	76
4.3	Evanescent waves	80
4.4	Power transportation in Frustrated Total Internal Reflection (FTIR)	83
4.4.1	Analytical wave field derivation	84
4.4.2	Power tunneling through the barrier	87
4.5	Goos-Hänchen shift	89
4.5.1	Stationary-phase method	90
4.5.2	Energy flux method	92
4.5.3	Causality in lateral propagation	97
4.6	Tunneling group delay for pulses	100
4.6.1	Energy dwell time and self-interference time	101
4.6.2	Group delay	102
4.7	Conclusion	104

V. Summary and Future work	107
5.1 Summary	107
5.2 Future Work	108
APPENDIX	110
BIBLIOGRAPHY	119

LIST OF FIGURES

<u>Figure</u>		
2.1	The structure of a Michelson bidirectional cavity.	10
2.2	The structure of a Mach-Zehnder ring cavity.	11
2.3	The tree structure of a fiber laser cavity (Michelson).	12
2.4	The structure of a Fabry-Pérot resonator cavity.	16
2.5	The spectral beating and array modes. (a) the longitudinal modes in one fiber. (b) the longitudinal modes in the other fiber with a different cavity length. (c) from spectral beating, the array modes are the frequency components strengthened by the interference when coherently combining, which coincide with the common longitudinal modes for both fibers.	17
2.6	(a): The spectral profile (blue, solid lines) at Port 2 of two-channel beam combining with lengths 8.053 m and 8.071 m in the absence of a saturable absorber; the phase difference $\Delta\phi$ between two adjacent longitudinal modes around the array modes (green crosses). (b): The related temporal profile at Port 2 for one roundtrip time. Note the fast oscillation with a frequency of about 5.56 GHz.	19
2.7	The comparison of cw output and pulsed output. Top: spectral intensity profile. Lower left: temporal profile with random mode phases. Lower right: temporal profile with modes with a fixed phase relationship.	21
2.8	The power transmittance curve for instantaneous power passing through the SESAM.	26

2.9	The simulation results for one mode-locked single fiber laser with a fast saturable absorber. (a) The spectral profile (green plots). The phase differences $\Delta\phi$ between two adjacent modes (red crosses) are almost constant. (b) The temporal pulse.	28
2.10	The Michelson interferometer structure for mode locking of two coupled fiber lasers. There is an angle cleave at Port 1 while a saturable absorber (SA) mirror is connected to the output port 2 to provide feedback and a mode locking mechanism.	29
2.11	The spectral profile (a) of two-channel beam combining and mode locking with fiber lengths 8.053m and 8.071m at Port 2 without nonlinearity. A saturable absorber partial mirror is used at Port 2. In the zoomed figure (b), the phase difference between two adjacent longitudinal modes is also plotted (green crosses). The phase difference $\Delta\phi$ remains at around 1.31π for the frequencies around the array mode.	30
2.12	The temporal profile at Port 2 of two fiber beam combining and mode locking with lengths 8.053m and 8.071m without nonlinearity. The figures are zoomed in from (a) one roundtrip time to (c) one single pulse.	31
2.13	The pulse packet output for the Mach-Zehnder ring cavity structure shown in Fig. 5, in the absence of nonlinearity. The length differences between two channels are (a) 5.1 mm, (b) 3.5 mm and (c) 2.1 mm respectively.	32
2.14	Comparison between simulation results (left) and the experimental results of Lhermite et. al. [8] (right) for (a) $\Delta L' = 5.1$ mm, (b) $\Delta L' = 3.5$ mm, and (c) $\Delta L' = 2.1$ mm. The corrected pulse separations are included in parentheses on the experimental plots. Experimental figure used by permission.	33
2.15	The time series (left) as well as intensity autocorrelation traces (right) for increased nonlinearity γ , with (a) $\Delta L' = 5.1$ mm, (b) $\Delta L' = 3.5$ mm, and (c) $\Delta L' = 2.1$ mm	35
2.16	Frequency spectra (blue, solid curves) and spectral phase (green crosses) in two-fiber-laser beam combining and mode locking for $\gamma=0.004\text{m}^{-1}\text{W}^{-1}$, with (a) $\Delta L' = 5.1$ mm, (b) $\Delta L' = 3.5$ mm, and (c) $\Delta L' = 2.1$ mm.	36
2.17	The structure of four-element fiber laser array with tree structure.	37

2.18	The spectrum in log scale (a) and temporal profile for one roundtrip time (b) for four-channel combining without saturable absorber. The four fiber lengths are independently randomly selected: 8.000 m, 8.011 m, 8.024 m and 8.041 m. Here the Kerr nonlinearity is $0.003 \text{ m}^{-1}\text{W}^{-1}$	38
2.19	The spectral (a) and temporal profiles (b) for four-channel coupling with saturable absorber and with $0.003 \text{ m}^{-1}\text{W}^{-1}$ Kerr nonlinearity. The fiber lengths are 8.000 m, 8.011 m, 8.024 m and 8.041 m. (b) denotes one roundtrip time and it is further zoomed to (c) and (d).	39
2.20	The spectral (a, b) and temporal (c, d, e) profiles for four-channel combining with saturable absorber and with $0.003 \text{ m}^{-1}\text{W}^{-1}$ Kerr nonlinearity. Here the four fiber lengths 8.050 m, 8.260 m, 8.200 m and 8.530 m are carefully designed for a 30 mm GCD for their differences.	40
2.21	The spectral (a) and temporal (b, c, d) profiles for four-channel combining with saturable absorber and with $0.003 \text{ m}^{-1}\text{W}^{-1}$ Kerr nonlinearity. The fiber lengths 8.000 m, 8.015 m, 8.040 m and 8.060 m are designed for a 5 mm GCD for their differences, which is in between the trivial 1 mm and non-commensurate 30 mm.	42
2.22	(a) The measured inter-cavity phase differences between points A and B, points A and C and points A and D, at the time points when there is a mode-locked pulse. (b) A temporal pulse packet from incommensurate lengths. At the time when a pulse is generated, the four channels maintain a good relative phase relationship for high efficiency.	44
2.23	The temporal plots for the observation on points A, B, C, and D respectively, i.e. the entrances of the directional couplers. The y-axis represents the temporal optical intensities in each fiber.	45
3.1	The theoretical solution of CQGLE with several possible different pulse shapes.	55
3.2	Some simulation results of our dynamic NLSE model. $\gamma = 0.005\text{m}^{-1}\text{W}^{-1}$ for (a) and $0.003\text{m}^{-1}\text{W}^{-1}$ for (b) and (c). $\beta_2 = 0.023\text{ps}^2/\text{m}$ for (a), $0.075\text{ps}^2/\text{m}$ for (b), $0.24\text{ps}^2/\text{m}$ for (c). $P_{SA} = 9.3\text{W}$ for (a) and (b), 0.93W for (c).	57
3.3	The structure of a ring cavity. A fiber amplifier is modeled with positive GVD, Kerr nonlinearity, gain saturation and spectral filtering. One end of the fiber connects to a lumped saturable absorber.	58

3.4	Simulation results for a single channel Yb-doped fiber. (a) The spectrum. (b) The pulse packet in the roundtrip time window. (c) The pulse profile with instantaneous frequency. (d) The transform-limited pulse.	58
3.5	The Mach-Zehnder interferometer structure for mode locking of two coupled fiber lasers. There is an angle cleave at one port while a saturable absorber is connected to the other output port to provide feedback and a mode locking mechanism.	59
3.6	Simulation results for a two-channel fiber laser array with $\gamma = 0.003\text{m}^{-1}\text{W}^{-1}$ and $\beta_2 = 0.023\text{ps}^2/\text{m}$. (a) The spectrum. (b) The pulse packet in the roundtrip time window. (c) The pulse profile with instantaneous frequency. (d) The transform-limited pulse.	60
3.7	Simulation results from a two-channel Er-doped fiber laser cavity in anomalous dispersion. (a) The spectrum. (b) The pulse packet in the roundtrip time window. (c) The pulse profile with instantaneous frequency. (d) The transform-limited pulse.	61
3.8	Simulation results for $\gamma = 0.0015\text{m}^{-1}\text{W}^{-1}$. (a) The spectrum. (b) The pulse packet in the roundtrip time window. (c) The pulse profile with instantaneous frequency. (d) The transform-limited pulse.	63
3.9	Simulation results for $\gamma = 0.0045\text{m}^{-1}\text{W}^{-1}$. (a) The spectrum. (b) The pulse packet in the roundtrip time window. (c) The pulse profile with instantaneous frequency. (d) The transform-limited pulse.	64
3.10	Increase the pulse repetition rate. (a) Harmonic mode locking multiplies the number of pulses circulating in the cavity. (b) An external etalon is used for spectral elimination.	66
3.11	Illustration of an infinitely long pulse train profile in temporal and spectral domains. (a) In time domain, it is a convolution of a single pulse shape envelope and an infinitely long pulse train with Dirac delta functions. (b) In frequency domain, it is the product of the spectral envelope of a single pulse and an infinitely long frequency comb, as a Fourier transform from (a). Red arrows denote Fourier transform.	68
3.12	Pulse train results from two-channel beam combining for fiber lengths 4.53m and 5.00m. (a) The spectrum and its zoom. Each circle denotes a longitudinal mode. (b) The temporal profile in a full roundtrip time. (c) The chirped output pulse. (d) The compressed pulse.	69
3.13	A comparison of Fig. 3.12 with commensurate lengths 4.50m and 5.00m (They are integer times of the difference 0.50m).	71

3.14	Illustration of a finite pulse train profile in temporal and spectral domains. (a) In time domain, it is a convolution of a single pulse shape envelope and a finite (also amplitude modulated) pulse train with Dirac delta functions. (b) In frequency domain, it is the product of the spectral envelope of a single pulse and a finite long frequency comb, as a Fourier transform from (a). Red arrows denote Fourier transform.	72
4.1	Upper: the structure of a directional coupler where two fiber cores with higher refractive indices are very close and parallel to each other. Lower: the single transverse mode in each fiber core tunnels to and gets coupled into the other core.	77
4.2	Two solution forms of electromagnetic equations: (a) Propagating wave. (b) Evanescent wave.	81
4.3	An example of TE wave patterns. (a) Propagating wave. E , H , k meets right-hand rule. (b) Evanescent wave. E is linearly polarized but H is elliptically polarized.	82
4.4	Geometry of the frustrated total internal reflection. The two cladding regions are separated by a fiber core with lower refractive index.	85
4.5	The power flux chart for FTIR. There is a Goos-Hänchen shift between the incident wave and the reflected/transmitted wave.	93
4.6	FTIR ray figure of beam combining in a directional coupler, where s is the Goos-Hänchen shift for FTIR and s' is the Goos-Hächen shift for TIR.	105

LIST OF TABLES

Table

2.1	Parameter values used in simulations.	27
2.2	Comparison on combining efficiencies for different setup.	43
3.1	Comparison between Yb-doped and Er-doped fiber laser arrays, with positive and negative GVD parameters respectively.	62
3.2	Comparison among different nonlinearity parameters.	63

CHAPTER I

Introduction

1.1 Background review on high power pulses in fiber lasers

Fiber lasers use doped optical fibers as gain media for light generation. Although the gain parameter may be not as high as in solid-state lasers, the unparalleled advantage of a fiber laser is that the gain media length can be kilometers long without occupying too much space since fibers can be coiled and the light is well shielded inside fibers. It also avoids any requirement for alignment and thus becomes possible to scale up to a large size array. Other highlights of fiber lasers include a very high surface-to-volume ratio for thermal management, good diffraction-limited beam quality for single-mode lasers, and superior pumping efficiency to operate with small pump powers [1–3], which attract researchers with many possible potential applications. In the recent decade, there are rapid developments on high-power fiber amplifiers and lasers with output powers on the order of 100 Watts [4–8]. On the other hand, mode-locked laser pulses with both high peak intensities and high energies are extremely important for a number of emerging applications in multiple disciplines, such as micro-machining, atom interactions, cellular dynamics, and medical surgery [3, 9]. Their high requirement on laser average powers, pulse peak intensities and pulse energies exceeds the capability of most current fiber lasers [10, 11].

The performance of a fiber laser is limited by nonlinear effects such as stimulated

Raman scattering (SRS), stimulated Brillouin scattering (SBS), self-phase modulation (SPM), and four-wave mixing (FWM) [2, 12]. Although these phenomena may be beneficial in some situations, e.g. soliton/dissipative soliton generation [13–19], self-similar propagation [20–23], and Raman lasers [24–26], they prevent fiber lasers from achieving high peak powers. The SPM may also cause possible wave-breaking [27–30] and affect mode-locked pulse quality in nonlinear fibers with high peak intensity. A large-mode-area fiber distributes the power in a larger cross section and hence reduces the light intensities per area, avoiding some unwanted nonlinear effects. Nevertheless, a too large fiber core diameter introduces many higher order modes while in many practical applications we need single mode fiber for a high quality of beams.

There are mainly three types of techniques to overcome these bottlenecks for fiber lasers. The first one is suppressing some unnecessary nonlinear effects such as SBS. SBS is one of the phenomena caused by the electrostrictive nonlinearity [2, 12]. The acoustic phonons get generated out of the optical wave in the fiber laser, and thus creating a grating that modulates the optical index [31, 32]. The photons lose a small amount of energy and get red-shifted after backward scattering. The coupling of these two antiparallel propagating modes further increases the reflection from the index grating. Above a certain threshold, such acoustic grating by SBS reflects most of the incident power, especially for long fibers. So far, transverse variations of the fiber acoustic indices [33–35] or longitudinal temperature variations [36, 37] have been proven to be effective in suppressing SBS effect.

The second approach is building a fiber laser array and coherently combining the output beams from each single fiber [38–46]. One more restriction in a fiber laser array, however, is that we have to make certain these coherent beams will be in phase for constructive interference, not canceling each other. The methods in building such an array of fiber lasers are mainly active beam combining with extra control circuits and signal processors, and passive beam combining where the light

itself can be stabilized at the status with maximal output powers and minimal losses without any external controls. Compared with active devices controlling the signal phase, passive devices usually use a composite Michelson interferometric resonator to interfere the longitudinal modes from each channel. The advantages of passive beam combining include simplifying the cavity complexity, reducing the size of the structure for integration, and saving the economic cost. Its major difficulty is to maintain a perfect phase relationship between all channels, which directly relates to the combining efficiency.

Chirped pulse amplification with stretching and compressing is the third approach and it has been already applied widely [47–49]. By chirping the pulse in dispersive fibers, we can temporally separate its spectral components and stretch its time duration by a large factor, without changing too much the total energy it carries. Thus the pulse peak intensity decreases by the same amount and some unwanted nonlinear effects can be therefore circumvented in fibers. After exiting the fiber, the pulse gets compressed again by compensating the dispersion with a prism or a pair of gratings for example. As a result, near bandwidth-limited pulses are obtained with the high peak pulse intensity restored. Such technique is well known and broadly used in applications.

Another drawback for fiber lasers is its limited pump absorption per unit length and limited gain, making it difficult to realize very short resonators for mode-locked lasers with gigahertz-level pulse repetition rate. Multi-gigahertz pulse trains with short pulses and low amplitude noise have many potential applications in high-capacity telecommunication systems, photonic switching devices, electro-optic sampling and for clocking and synchronizing [9, 50–52]. To enhance the repetition rate for a fiber laser, there are at least three conventional methods including shortening the cavity length, harmonic mode locking [3, 53–58], and external Fabry-Pérot cavities [59–61]. It is seen that coherent beam combining provides one more option towards

the high repetition rate without extra devices or designs. The nature of coherent beam combining determines a high repetition rate which is also easy to tune, by simply adjusting the length difference among channels [62–64].

In order to navigate further toward the goal of diffraction-limited high power pulses from a fiber laser, all these three types of solutions need be used together. In this thesis, we focus on the passive coherent beam combining in a fiber laser array and show that simultaneous passive coherent beam combining and mode locking are very helpful in achieving a pulse packet, with both high peak pulse intensities and high repetition rate. To further increase the pulse energy as well as make it more robust and resistant to wave breaking, pulse trains of dissipative solitons are produced in normal dispersion regime. Last but not the least, directional couplers, the key part used for coherent beam combining, are explored with its unique physics principle: light wave tunneling through an optical barrier.

1.2 Thesis Outline

In Chapter II, we introduce our dynamic model for simultaneously passive coherent beam combining and mode locking based on Nonlinear Schrödinger equation (NLSE). Models for different cavity resonators and different saturable absorbers are presented, in addition to NLSE and gain saturation equation for our simulation model. To check the validity of the model, experiments are reproduced numerically with our model and similar results are achieved. With a comparison among cw operated coherent beam combining, mode-locked single fiber laser, and mode-locked and beam combined fiber laser array, it is concluded that the coherent beam combining scales up the power from a single channel, and mode locking produces short pulses for a high peak power at the same time. Nonlinearity perturbs the mode-locked pulses by self-phase modulation (SPM) and is the cause for possible wave breaking.

Because the fibers of the array have different lengths, each fiber has its own lon-

gitudinal modes and there is spectral beating in the beam combined fiber array. The modes nearby the common longitudinal modes, named as array modes, are enhanced and almost all other modes disappear. The array mode separation is inversely proportional to the fiber length difference. In the fiber laser array, it is the array modes that determine the output to be a pulse packet instead of a single pulse. The density of modes decreases quickly with increasing of the number of combined channels. However, a nice shaped pulse packet with a uniform pulse separation is still possible when the lengths of all channels are commensurate.

In Chapter III, the lasing wavelength is switched to normal dispersion region, in order to generate dissipative solitons which exist in non-conservative environment. With both amplitude and phase balances, dissipative solitons in normal dispersion are more stable and robust to wave breaking than conventional optical solitons. It should be noted that dissipative solitons can also exist in anomalous dispersion regime, however, the chirp in normal dispersion makes the pulse more stable until the nonlinear phase overcomes the chirp bandwidth [65, 66]. Amplitude modulations such as saturable absorption and spectral filtering in the cavity are important for dissipative soliton generation with normal dispersion. Cubic-quintic complex Ginzburg-Landau equation (CQGLE) is frequently used to model the dissipative pulses in a single fiber laser, however, this model is not very suitable for fiber laser arrays with only one lumped saturable absorber to mode lock all channels. Here we use our generalized NLSE model by taking all these effects into consideration for the dissipative soliton simulation, and get numerical results similar to the analytical solution by CQGLE.

With coherent beam combining, the power is scaled up and we are able to get a stable pulse train of dissipative solitons that is robust to wave breaking. As an advantage to several conventional methods in increasing the pulse repetition rate by additional control or devices, passive coherent beam combining can naturally lead to a frequency comb because of the array modes, and hence produce a pulse train whose

repetition rate is high and tunable by changing the fiber length difference. A pulse train with uniform pulse interval can be generated from beam combined dissipative solitons. Incommensurate fiber lengths result in an amplitude modulation on the pulse train, which otherwise has a uniform amplitude with commensurate lengths.

Chapter IV provides a deep insight to directional couplers, the key device used in passive coherent beam combining. By putting two parallel fibers together in a very short distance, the mode power inside each fiber may exchange and couple to the other. Therefore the transform matrix can be derived out of coupled-mode theory. On the other hand, the fundamental physics of optical coupling is frustrated internal total reflection (FTIR). Total internal reflection (TIR) confines the light inside a fiber core and the wave becomes evanescent outside the core. However, TIR can be frustrated when another fiber core is so close that the evanescent wave has not been completely decayed, and therefore the power can tunnel through the barrier to the other core. It is seen that although an evanescent wave has no time-averaged energy flux along its decaying direction, the power transportation is carried by the interference of two evanescent eigenmodes across the barrier.

In the tunneling dynamics, the group delay time between a pulse peak entering and exiting the barrier through tunneling is an interesting topic. It appears “superluminal” since it saturates with the increase of tunneling distance as Hartman effect. During tunneling process, the incident energy first gets temporarily stored either as evanescent waves in the barrier, or as the self-interference between incident and reflected waves, and then gets released as reflected or transmitted waves. With the concept of the dwell time inside barrier and the self-interference time in front of the barrier, the physics of a group delay is revealed as a sum of these two time, i.e. the time for total energy storage before releasing. On the longitudinal direction of tunneling, the group delay is not actually related to any velocities of propagation.

During the group delay time, the energy’s release position also gets laterally shifted

from its entrance to the barrier. Such lateral displacement is named as Goos-Hänchen shift. Besides the stationary phase method, we calculate it by energy flux method, with better insights on physical meaning. Such shift is divided into two parts, the barrier's energy dwell time multiplied by its lateral energy velocity, and the self-interference energy storage time multiplied by its lateral energy velocity. Unlike the longitudinal tunneling process, the Goos-Hänchen shift is caused by energy propagation. Here we prove both energy velocities are causal and hence it does not violate special relativity.

Chapter 5 provides the brief summary of overall work and some advice for future work.

CHAPTER II

Mode-Locking in Passive Coherent Beam Combining

2.1 Introduction

Passive coherent beam combining is under intensive investigation as a means of scaling up the output power of fiber lasers [39, 42, 43, 46, 67, 68]. One common approach is to use 50:50 couplers to combine fiber amplifiers pair-wise in a tree structure to form an interferometric composite cavity. The coherently phased output is the result of the system selecting the modes that minimize the overall loss in the composite cavity. To date, most of the beam combining experiments based on this approach have used cw lasers and there is very little data on their dynamic behavior under Q-switching [69] or mode locking [62] conditions. Since mode locking enables the creation of high-peak power short pulses from a single fiber laser [70], the possibility of further power scaling through passive combining of several mode-locked lasers is worthy of investigation.

In this chapter we present a detailed dynamical model of passive coherent beam combining in the presence of a saturable absorber. Our results show, in agreement with experiment [62], that the presence of a saturable absorber leads to the generation of packets of mode-locked pulses from the coherently-combined lasers. Within each

packet the periodicity of the pulse train can be controlled by varying the length difference between the fibers. Repetition rates of hundreds of gigahertz are readily obtained for short enough length differences. The combining efficiency is high for two lasers but does drop as the number of lasers is increased, a phenomenon also seen in cw beam-combining [46, 67]. Our work represents, to the best of our knowledge, the first modeling study of simultaneous beam combining and mode locking of lasers.

2.2 Background on passive coherent beam combining

Along the path of developing high power with fiber lasers, the nonlinearity associated with the third-order susceptibility $\chi^{(3)}$ limits the power output from a fiber laser [2, 12]. When the power carried by a fiber is high, the strong optical field interacts with fiber materials and induces a nonlinear polarization field leading to some nonlinear optical phenomena such as self-phase modulation (SPM), stimulated Raman scattering (SRS), stimulated Brillouin scattering (SBS) and four-wave mixing (FWM). Because of the existence of these nonlinear effects, the power carried by a single fiber laser is limited and it is difficult to reach higher power outputs from a single fiber laser. In order to solve the bottleneck to output high powers, there is much current interest in passive coherent beam combining in laser arrays, adding up the output power from multiple fiber amplifiers.

To beam combine the fields of several amplifying fibers into a high power and diffraction-limited beam, discrete 50:50 directional couplers are used to create an interferometric system of coupled amplifier pairs. For a coherent combining, it requires that the phases from two input channels of the directional coupler to be in a particular relationship, so that there can be a constructive interference at one output port and a destructive interference at the other output port. Then most power from two input channels get combined together coherently and the loss is reduced to minimum [40, 71–76]. The combining is passive because the combining is done passively by

50:50 directional couplers. Beginning with spontaneous emission, the laser system stabilizes to the state with the minimal loss after many roundtrips. The phase relationship between two channels is automatically selected and maintained by the laser system, without the need for active control. Passive coherent beam combining scales up the output power from single fiber lasers into a fiber laser array.

2.2.1 Array structures of fiber laser cavities

For a fiber laser array, there are several different designs on the cavity resonator, including Michelson bidirectional cavity and Mach-Zehnder unidirectional cavity.

An example of a bidirectional Michelson cavity is shown in Fig. 2.1. One directional coupler is used to combine two channels and it is a Michelson interferometer structure except that both arms are replaced by rare-earth-doped fibers. In such structure, the light wave bounces forth and back in the cavity as bidirectional. The 50:50 directional coupler acts like a beam splitter. The two input arms of the directional coupler are connected to two fiber channels and one of the two output arms is connected with a partial reflector to provide feedback to the system. The other output arm connects with an angle cleave to leak any power through it. The continuous-wave pump beams are launched into each active fiber by a wavelength division multiplexer (WDM).

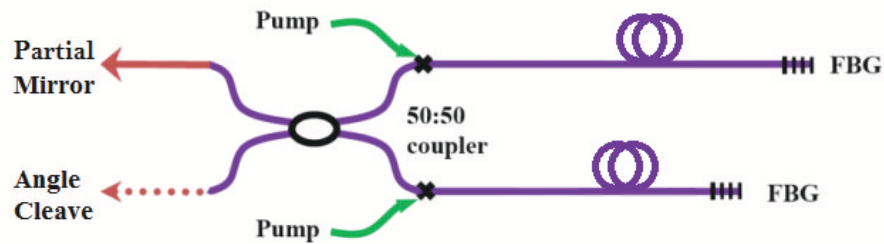


Figure 2.1: The structure of a Michelson bidirectional cavity.

Besides bidirectional cavities, there are unidirectional ones where light travels only in one-way inside the ring cavity. This is guaranteed by an optical isolator in the

roundtrip path as shown in Fig. 2.2. In this case, two directional couplers are used at both ends of the cavity. It simulates a Mach-Zehnder interferometer, which has advantage that each of the well separated light paths is traversed only once compared with the bidirectional Michelson interferometer. In such unidirectional ring cavities, although there is one more 50:50 directional coupler, the light goes in one-way and the possibility of interference between the forward and backward going wave has been ruled out, hence the modeling is simpler. On the other hand, a careful dynamic analysis from Ref. [45] shows that such interference effect even in a directional cavity is very small, because the magnitudes of forward and backward going lights are not in the same order for a most common 4% partial reflection. So no matter whether we use bidirectional Michelson cavities or unidirectional Mach-Zehnder cavities, it does not affect the validity of our conclusion in coherent beam combining. However, with the same fiber lengths, the roundtrip time for the light to traverse in a ring cavity is only a half of the bidirectional cavity, and this character will be useful for pulse trains discussed in Chapter 3.

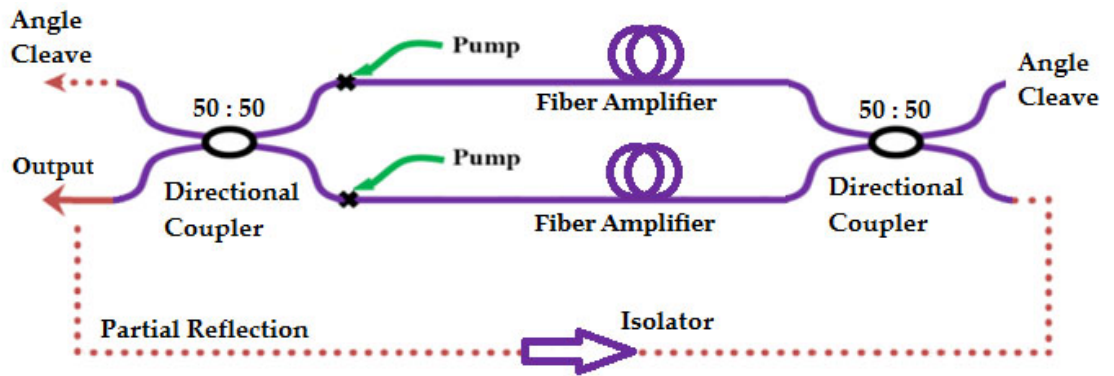


Figure 2.2: The structure of a Mach-Zehnder ring cavity.

In either type of cavity, the waves are generated from the individual fiber amplifiers and then add on or cancel out with each other at the coupler outputs accordingly. The interferometer structures allow two channels to have different lengths. At the very beginning the spontaneous wave phases from two fibers are independent and in-

coherent. As the laser oscillation grows up, the phase relationship with most feedback increases faster than others and it finally dominates. The mechanism is the same.

To scale up to a higher number of elements in the array, the structure is organized like a tree in Fig. 2.3 in a binary tree style. Take Michelson bidirectional cavity for an example, two fiber amplifiers are connected via a directional coupler to form a pair, and two pairs can be coupled with another directional coupler again for a new pair, and so on. Among all directional couplers, only one output port from the root level has partial reflection and all others are with angle cleaves. The combining principle in each level is similar and recursive. Therefore, it is seen that a large scale fiber laser array with passive coherent beam combining could be built up in a tree structure.

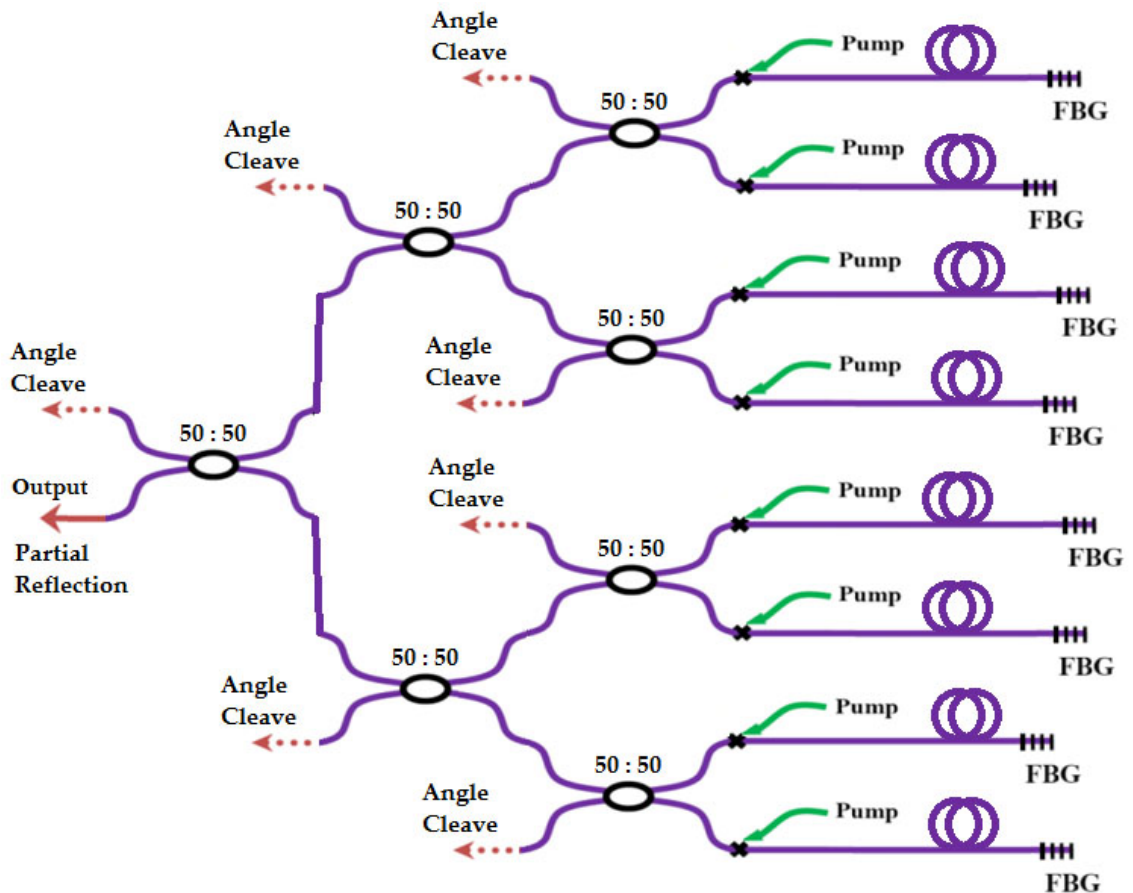


Figure 2.3: The tree structure of a fiber laser cavity (Michelson).

2.2.2 The dynamical model for passive coherent beam combining

Here we use a model by Wu et al. [44], using the amplifying Nonlinear Schrödinger Equation (NLSE) to incorporate the multiple longitudinal modes and allow for the natural selection of the resonant array modes with the minimum loss.

Assuming single polarization, the coherent optical waves in each active fiber are governed by the NLSE in conjunction with the rate equation for the population inversion. It is a propagation model that takes into account many cavity parameters such as gain saturation, Kerr nonlinearity, group velocity dispersion (GVD), and the loss dispersion of spectral filters. The two independent single mode fibers are coupled discretely by a directional coupler as shown in Fig. 2.2. In each active fiber, the NLSE can be written as

$$\frac{\partial E}{\partial z} = \frac{1}{2}(g - \alpha)E - \beta_1 \frac{\partial E}{\partial t} + \frac{1}{2}(\beta_2 - ib) \frac{\partial^2 E}{\partial t^2} + i\gamma|E|^2 E, \quad (2.1)$$

on propagation coordinate z , where $E(z, t)$, g , α , β_1 , β_2 , and γ represent the slowly varying envelope of the electric field in the oscillating cavity, the saturated gain, the cavity linear loss, the inverse of group velocity, the group velocity dispersion (GVD), and the non-resonant Kerr nonlinearity respectively. The dispersion loss parameter b provides distributed spectral filtering along the fiber amplifier. Here the electric field amplitudes E are after normalizations so that $|E|^2$ represents power.

At the same time, we have the dynamic rate equation for population inversion of the fiber laser:

$$\frac{\partial \Delta N}{\partial t} = R_p(t) - \frac{\Delta N}{\tau_{up}} - \frac{\sigma|E|^2}{h\nu A_{eff}} \Delta N, \quad (2.2)$$

where ΔN and $R_p(t)$ refers to the population inversion and the pumping rate in a fiber. In the right hand side of eq. (2.2), the second term has a physical meaning of the process of excited population relaxation with upper-state lifetime τ_{up} , and the third term describes the laser gain saturation at high intensity fields, where σ is the

sum of absorption and emission cross sections, $h\nu$ is the energy per photon, and A_{eff} is the effective fiber cross section area.

The rate equation is dynamic, suitable for any situations no matter whether it is in steady state or not. In this thesis, we mainly focus on the stable results in steady states, without Q-switched instabilities. Therefore we make a further simplification on the dynamic rate equation. A typical roundtrip time for a fiber length in tens of meters is a few hundreds of nanoseconds, while the upper level population relaxation τ_{up} is approximately ten milliseconds for Er-doped and one millisecond for Yb-doped fiber lasers. The gain recovery time, is also quite long and is of order milliseconds for Er-doped fibers [77, 78]. Hence the roundtrip traversal occurs in a time much faster than the recovery dynamics of population inversion, and we may consider these slow variables as quasi-static during a roundtrip calculation. The difference in time scales allows one to make approximations by setting the time derivative in the rate equation to zero. Eq. (2.2) could be simplified to a gain saturation equation:

$$g = 2\sigma\Delta N = \frac{g_0}{1 + \frac{\int_0^T |E|^2 dt}{TP_{sat}}}, \quad (2.3)$$

by assuming $g_0 = 2\sigma R_p(t)\tau_{up}$ as the unsaturated gain and $P_{sat} = h\nu A_{eff}/(\sigma\tau_{up})$ as the saturation power. T denotes for a computation window which is usually selected as the roundtrip time over the mean fiber length because of the periodicity. For unidirectional cavities, the roundtrip time is $n\bar{L}/c$, and it is $2n\bar{L}/c$ for bidirectional ones.

The unidirectional Mach-Zehnder model separates the backward and forward paths and hence describes quite accurately the behavior of a ring fiber laser. For a bidirectional Michelson cavity, the partial reflectivity at the output port is typically around 4%, and hence the backward going wave is always much weaker than the forward one [44, 45]. The standing wave effects and cross-saturation by backward waves

can be safely neglected. So we may still only consider the forward propagating waves in Eq. (2.1).

As a four port device with two input and two output ports, the transfer matrix of an ideal lossless 50:50 directional coupler is modeled as:

$$\frac{1}{\sqrt{2}} \begin{pmatrix} 1 & -i \\ -i & 1 \end{pmatrix}, \quad (2.4)$$

as a result from coupled-mode theory. More detailed discussions about the directional couplers will be included in Chapter IV.

As a numerical algorithm for solving partial differential equations, the standard split-step Fourier methods (SSFM) treats the linear terms in spectral domain and the nonlinear terms in temporal domain. It has been extensively used as an effective method for simulating the behavior of nonlinear pulse propagation in fibers because of the separate treatment. By this algorithm, the cavity is divided into discrete split steps and the wave field need be transformed between temporal and spectral domain a few times per split step. All longitudinal modes within the calculation bandwidth are sampled as frequency points for the wave field, and its temporal profile could be calculated from Fast Fourier Transformation (FFT). In this thesis we also use SSFM to handle the multi-longitudinal-mode nature of continuous-wave fiber lasers.

2.2.3 Array modes and spectral beating

The frequencies of laser operation are not only determined by the gain material that the laser is constructed from, i.e. the gain bandwidth, but also by the size of the optical resonant cavity. Take a linear 1-D Fabry-Pérot resonator as shown in Fig. 2.4 for an example. The optical wave bouncing between mirrors will form standing waves. Based on the boundary conditions, only those frequency modes with vacuum wavelengths $\lambda_m = 2nL/m$ can exist, where n is the refractive index and m is any posi-

tive integer. The corresponding frequencies f_m are longitudinal modes of the resonant cavity. Therefore the separation between the m th and $m + 1$ th modes is determined by $\Delta f = c/(2nL)$. Usually there are thousands to millions of such oscillating longitudinal modes in a laser cavity. In a cw laser, each mode oscillates independently with randomly distributed phases, affected by many factors such as thermal changes. There is no fixed phase relationship among these longitudinal modes. The constructive or destructive interference between these unlocked modes can lead to some random intensity fluctuations, however, since the number of modes is huge, the output tends to stabilize with small fluctuations, making it cw.

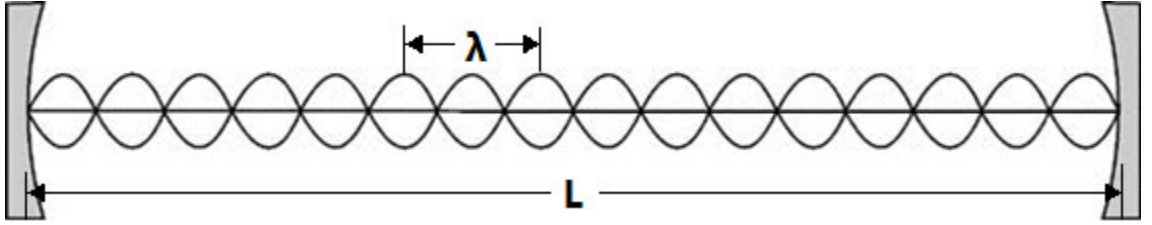


Figure 2.4: The structure of a Fabry-Pérot resonator cavity.

In agreement with experimental observations, our model shows efficient coherent beam combining without the need for interferometric control of fiber lengths. Each combined fiber in the array has its own length, and its own set of longitudinal modes. In order to get resonant in the whole array, the laser system chooses automatically only the longitudinal modes which are common for all the combined active fibers, and such common modes are named as the array modes [44, 45]. Other frequency modes which are not the common array modes are unstable with relatively high losses. And only the modes with least total roundtrip loss will exist in the steady state. Therefore, the spectral power which was carried by almost all longitudinal modes within the gain bandwidth is now focused into these array modes. Since they are the common longitudinal modes, the array modes are less dense and look as a comb spectrum modulation with a fixed beating frequency, such phenomenon is described as

Vernier's effect. The frequency of spectral beating is exactly the separation between two adjacent array modes, which is given by $\Delta f = c/(n\Delta L)$ for a unidirectional ring cavity with two channels, and $\Delta f = c/(2n\Delta L)$ for a bidirectional one. Here n is the refractive index for fiber cores.

From Vernier's effect, spectral beating exists as long as the fiber lengths are not the same in a coherently beam combined fiber laser array. It is the spectral beating who reduces the number and the density of modes in the array from a single fiber laser. For single-transverse-mode fiber lasers, the power per longitudinal mode can be significantly increased by the coherent beam combining between channels.

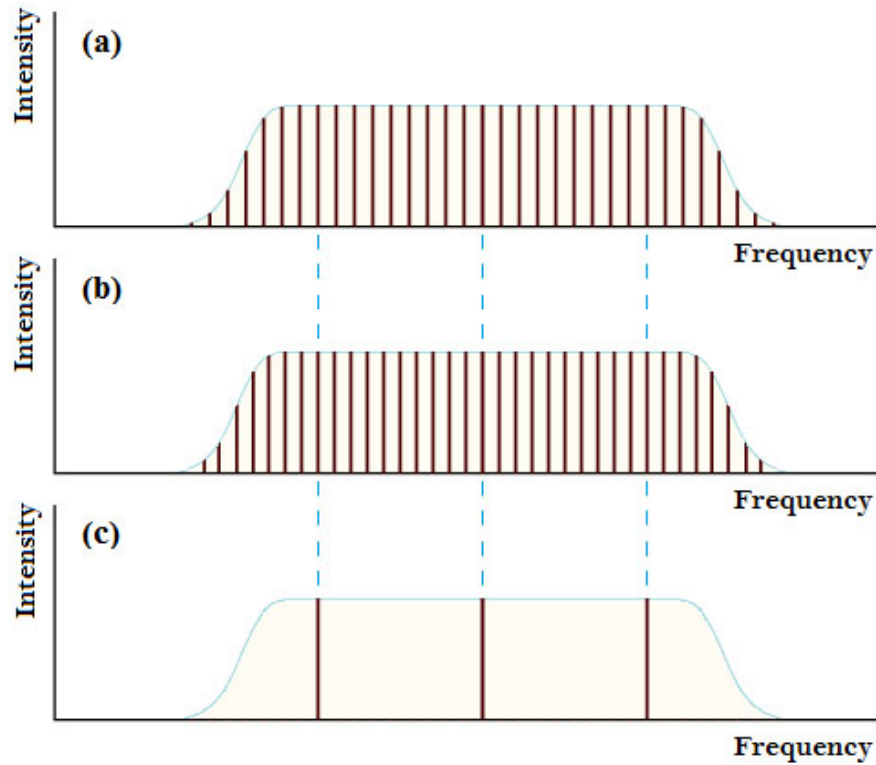


Figure 2.5: The spectral beating and array modes. (a) the longitudinal modes in one fiber. (b) the longitudinal modes in the other fiber with a different cavity length. (c) from spectral beating, the array modes are the frequency components strengthened by the interference when coherently combining, which coincide with the common longitudinal modes for both fibers.

On the other hand, the reduction of the number of longitudinal modes determines

the scaling-up limit of the coherent beam combining. The more fiber channels to be combined, the less common array modes there are. The coherent beam combining ability saturates when there is only one longitudinal mode which is common for all channels within gain bandwidth. Beyond that limit, the efficiency of the coherent combination will drop hugely and the increase of the number of active fibers will not further increase the power per array mode nor the total power output. That is to say, the additional fiber cannot be coherently beam combined for cw operation, and additional powers will leak through the angle cleave ports of the directional couplers.

2.2.4 Coherent beam combining results in cw operation

All the active fibers we used in this thesis are doped with erbium as the gain medium. The fields evolve from an initial noise distribution and we examine the output after about 2000 round trips in fiber cavities with lengths of about 8 meters. Each round trip contains 24 discrete spatial steps.

In cw operation, the output is continuous with a spectrum that shows a beating between the individual frequency combs of the individual lasers. As seen in Fig. 2.6, the spectrum consists of array modes spaced approximately by the beat frequency $\Delta f = c/(2n\Delta L) = 5.56$ GHz, where n is the index and ΔL is the length difference between the two channels. Each of the frequency “spikes” is actually an envelope of about 100-MHz full width at half maximum (FWHM) that contains a few single-cavity longitudinal modes. The phase difference between two adjacent longitudinal modes is randomly distributed from 0 to 2π , indicating that there is no phase locking among the lasing modes. In the time domain we see the high frequency oscillation representing the complex beating between these modes with random phases. The combining efficiency is very high, with 99.97% of the power emerging from the output port and only 0.03% from the loss port with angle cleave. The beam combining process selects the modes with minimum loss.

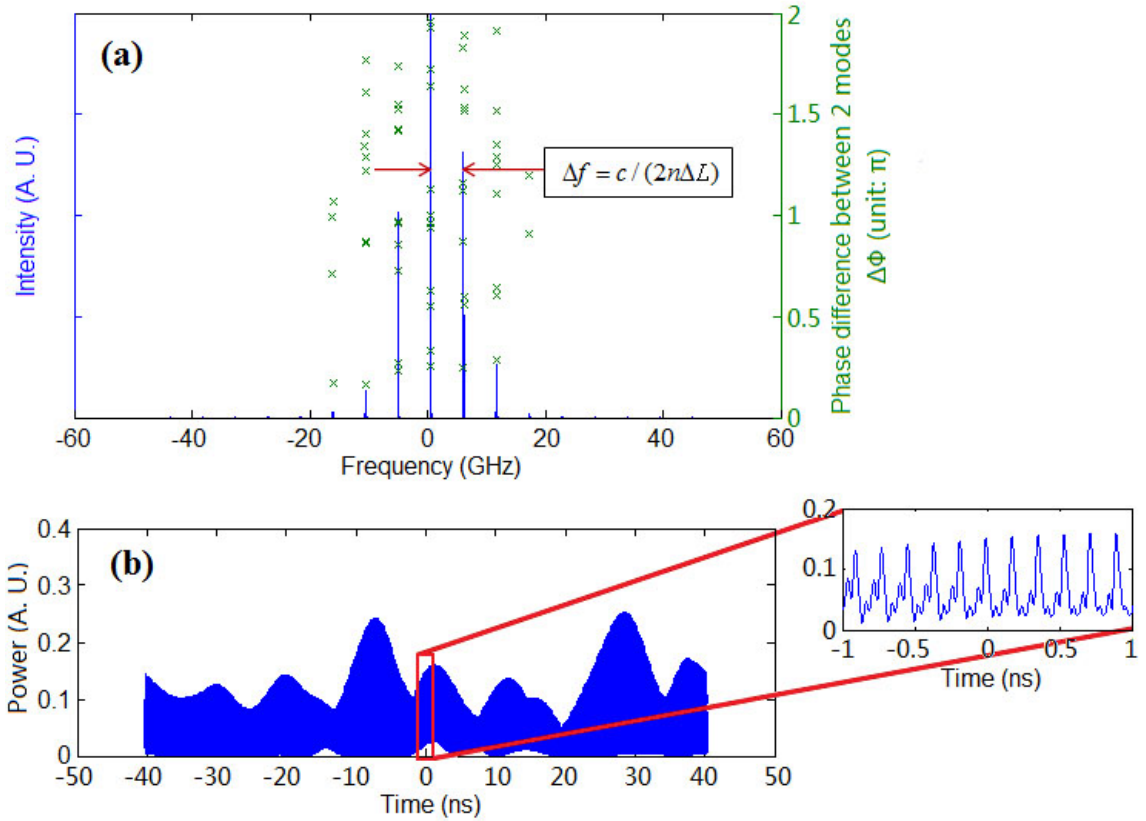


Figure 2.6: (a): The spectral profile (blue, solid lines) at Port 2 of two-channel beam combining with lengths 8.053 m and 8.071 m in the absence of a saturable absorber; the phase difference $\Delta\phi$ between two adjacent longitudinal modes around the array modes (green crosses). (b): The related temporal profile at Port 2 for one roundtrip time. Note the fast oscillation with a frequency of about 5.56 GHz.

2.3 Background on mode locking

As an approach to ultrafast laser pulses, mode locking has been widely applied in laser operation. The core idea of mode locking is to lock the laser cavity's longitudinal modes with a fixed phase relationship. Interference between these phase-locked longitudinal modes results in a pulsating laser output [9, 70, 79–85]. Either an active element, e.g. an optical modulator, or a nonlinear passive element, e.g. a saturable absorber, is inserted in the laser resonance cavity, converting the laser's continuous-

wave (cw) output into periodical ultrafast pulses. Because of the cavity boundary conditions in the steady state, the pulse parameters remain stable and almost constant after circulating every round trip.

Instead of the random oscillations seen in cw operation with many independent modes, when there is a fixed phase relationship, these longitudinal modes can be phase-locked to a common phase at some particular place that moves back and forth inside the cavity. Such phase-locking allows for the formation of a narrow pulse centered on the exact position of their common phase, i.e. the mode-locked pulse. At positions other than the common phase, the fields destructively interfere, and there will be no longer cw outputs in the cavity. The constructive interference of the laser modes occurs periodically every roundtrip, producing one mode-locked intense burst per roundtrip. In mode locking operation, the pulse duration depends on how many modes are locked together with a fixed phase relationship [2, 86, 87]. If there are N modes locked, the mode-locked bandwidth is approximately $N\Delta f$. In the transform limit, the pulse duration is inversely proportional to the bandwidth. The roundtrip time, which is also the pulse's interval, corresponds to a frequency exactly equal to the mode spacing of the laser, $T = 1/\Delta f$. An example is shown in Fig. 2.7. With the same spectral intensity profile of longitudinal modes, after Fourier transformation, the power in a roundtrip is distributed as cw if the phases are randomly distributed, but is focused into a single pulse if the phase relationship is locked for all modes.

There are two major types of mode locking: active and passive.

2.3.1 Active and passive mode locking

Active mode locking modulates the resonator losses actively. One of the most common realizations is an acousto-optic modulator. With an electrical signal, a sinusoidal amplitude modulation on laser can be generated inside the cavity. The amplitude modulator acts as a weak shutter to the optical wave bouncing, putting a

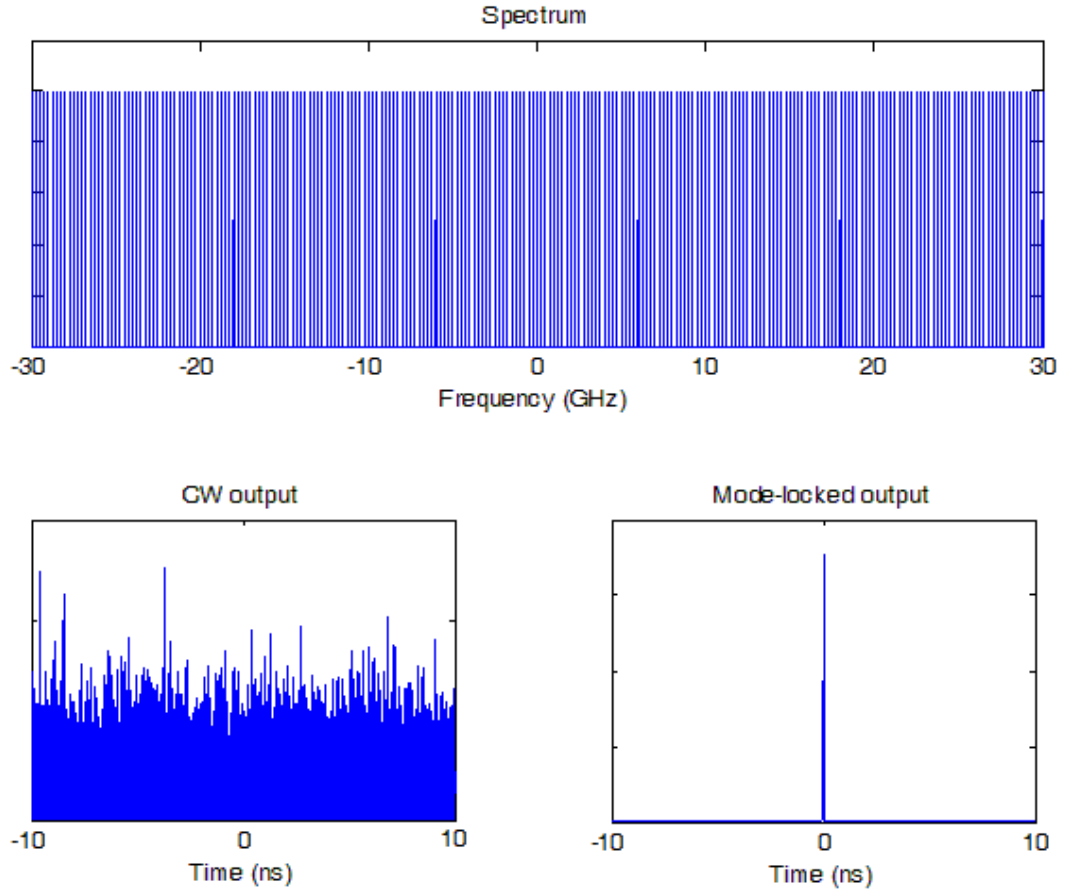


Figure 2.7: The comparison of cw output and pulsed output. Top: spectral intensity profile. Lower left: temporal profile with random mode phases. Lower right: temporal profile with modes with a fixed phase relationship.

high attenuation on the output when it is “off”, and a much smaller attenuation when it is “on”. If the modulation rate δf is fully synchronized to the cavity round-trip time T , then only a single pulse with the “correct” timing can pass the modulator per round trip at the moment when losses are minimized. This is known as AM active mode locking. In the frequency domain, for a mode with an optical frequency f , the modulated signal has two sidebands at frequencies $f \pm \delta f$. If we drive the modulator at the same frequency as the cavity-mode spacing δf , then the two sidebands exactly correspond to the two longitudinal modes adjacent to the original mode. Since the sidebands are driven in-phase from the active modulator, these 3 adjacent modes

are locked in-phase. Similarly, all other adjacent longitudinal modes can be locked together in-phase, until most modes in the gain bandwidth are locked.

Similar to AM active mode locking, there is also FM mode locking by electro-optic modulators. With an applied electrical signal, it can induce a small and sinusoidally varying frequency shift in the optical wave passing through it inside the cavity. If the modulation frequency matches the cavity traversing round-trip time, then a part of the light is repeatedly blue-shifted, and some other gets repeated red-shifts. After many repetitions, they finally move beyond the gain bandwidth as the accumulation of the frequency shifts. The part of the optical wave which passes through the modulator with zero induced frequency shift will be left unchanged, forming a narrow pulse of light.

Another approach of active mode locking is synchronous pumping. Here the pump source is already modulated higher and lower than threshold, effectively turning the laser on and off to produce pulses. Typically, the pump source is itself another mode-locked laser. This technique may introduce short pulses with severe spectral broadening in nonlinear cavities, described as supercontinuum. Generally, synchronous pumping requires very accurately matching the cavity lengths of the pump laser and the driven laser.

Unlike active methods, passive mode locking techniques require no external signals to produce pulses. A saturable absorber is commonly used to achieve this. As an optical device that exhibits an intensity-dependent transmission, a saturable absorber behaves differently depending on the time-domain optical intensity passing through it. When placed in a laser cavity, a saturable absorber will attenuate low-intensity constant wave light, and transmit light which is of sufficiently high intensity [88]. For simplicity, it is assumed that there is a single circulating pulse in its steady state and a fast absorber. Each time the pulse hits the saturable absorber, it saturates the absorption with its high intensity and the losses are temporarily reduced. At other

times, any light of lower intensity experiences much higher losses at the saturable absorber when circulating the cavity. Since the laser system always reaches the steady state with minimal losses, the absorber can thus suppress any continuous background signal as well as some weak pulses. Also, the absorber thus tends to decrease the pulse duration by putting a high loss on the low intensity parts of a pulse, and therefore suppress the sub-pulse noises and clean up the pulse shape.

Usually, the saturable absorber can self-start the mode locking process automatically. In this case, the laser oscillation first starts with random mode phases with fluctuations of cw power. In each round trip, the saturable absorber favors the light with higher intensities, which saturates the absorption more than light with lower intensities. That is to say, high-intensity spikes have a higher net gain every round trip and hence get selectively amplified. After the accumulation of many round trips, the part with the highest temporal intensity dominates as a short pulse, and other parts with higher losses gradually go below the threshold and vanish.

There are also passive mode locking schemes that directly display an intensity dependent absorption without a saturable absorber additional to the cavity. That is to say, some nonlinear optical effects in intracavity components provide an effective saturable absorption, selectively amplifying high-intensity light and attenuating low-intensity light. One example is Kerr-lens mode locking or “self mode locking”. With the nonlinearity of optical materials, Kerr effect makes high-intensity light focused differently from low-intensity light. Another example uses nonlinearity in the directional couplers, where high-intensity light goes to the port with feedback for cavity oscillation, and low-intensity light goes through another port and get lost [89, 90].

Because of the response time of saturable absorbers, the pulse duration from passive mode locking is usually much shorter than active ones. Another advantage of passive mode locking is that the cavity design becomes much simpler without complicated and expensive active components.

2.3.2 Saturable absorber modeling

Saturable absorbers are commonly made of liquid organic dyes, doped crystals, quantum dots, semiconductors, nonlinear polarization rotation device, carbon nanotubes or atomic layer graphene. Different absorber devices are used since different applications require very different parameters. Semiconductor saturable absorber mirrors (SESAM) tend to exhibit response times as fast as the order of 100fs. In a passively mode-locked laser, such fast response time determines the final short duration of the pulses and hence SESAM are very frequently used for passive mode locking.

It is a fast saturable absorber if its recovery time is well below the pulse duration. In that case, the loss modulation basically follows the variation of the temporal optical power. For a slow absorber with a recovery time above the pulse duration, mode locking can also be achieved. Because its response is slow, the saturable absorber may be in the unsaturated state at the time the leading edge of the pulse hits it and still in the saturated state shortly after the pulse. Both experimental observations and numerical simulations indicate stability for the slow saturable absorbers. The stronger absorption for the leading edge of the pulse shifts the position of the maximum and therefore delays the pulse in this situation.

As an optical component with low losses at high optical intensities and high losses at low intensities, saturable absorbers are widely applied for passive mode locking. However, besides the main pulse, any random and intense spike will be transmitted without high losses by the saturable absorber. After many round trips, this may still lead to more than one pulse per roundtrip in mode locking. Self-starting is not always achieved. Generally speaking, slow absorbers are more suitable for self-starting mode locking than fast absorbers.

Paschotta and Keller [9, 91] have built an analytical model for saturable absorbers with a time-dependent power-loss coefficient $q(t)$ which depends on the parameters

of the absorber and on the pulse exciting the absorber. With the recovery time τ , the unsaturated loss q_0 , and the saturation fluence F_{sat} , the dynamic model for $q(t)$ is given by:

$$\frac{dq}{dt} = -\frac{q - q_0}{\tau} - \frac{I}{F_{sat}}q. \quad (2.5)$$

In the slow limit with large recovery time τ , we can ignore the first term and simply solve for q as:

$$q_{slow} = q_0 \exp(F_p/F_{sat}), \quad (2.6)$$

where F_p is the pulse fluence if it hits an initially unsaturated absorber. The amplitude-loss coefficient $\alpha_{slow} = q_{slow}/2$ for the quadratic relationship between power and amplitude.

On the other hand, for a fast saturable absorber with a very short recovery time (e.g. 100fs), it responds almost immediately for a picosecond level mode-locked pulse. In this case, we may consider the saturation process as quasi-static with setting the dynamic term of dq/dt to zero. It means that the power-loss coefficient q reaches its steady state very fast and remains almost constant during the short time in our calculation. By taking $dq/dt = 0$, we have

$$q_{fast} = \frac{q_0}{1 + \frac{I}{F_{sat}/\tau}}. \quad (2.7)$$

Therefore, the amplitude-loss coefficient

$$\alpha_{fast} = q/2 = \frac{q_0/2}{1 + \frac{I}{F_{sat}/\tau}} = \frac{\alpha_0}{1 + \frac{I}{P_{SA}}}, \quad (2.8)$$

where $\alpha_0 = q_0/2$ is the unsaturated amplitude-loss coefficient, and $P_{SA} = F_{sat}/\tau$ is the effective saturation power for the absorber, defined by the saturation fluence over the recovery time. With the formula for q or α , the saturable absorption process can

be modeled quantitatively with other equations on laser propagation in the cavity.

In this thesis we use a semiconductor saturable absorber mirror (SESAM) with a response time of a few picoseconds, and the fast saturable absorber model is appropriate here. Taking $\alpha_0 = 0.33\text{mm}^{-1}$ with a thickness of 3.0mm, we have plotted the power transmittance by Eq. (2.8) for passing through such SESAM in Fig. 2.8 It is observed that there is an obvious loss until the instantaneous power grows above around 50mW. By suppressing low power components, it sharpens the pulse from background noises and stabilizes the pulse against perturbations.

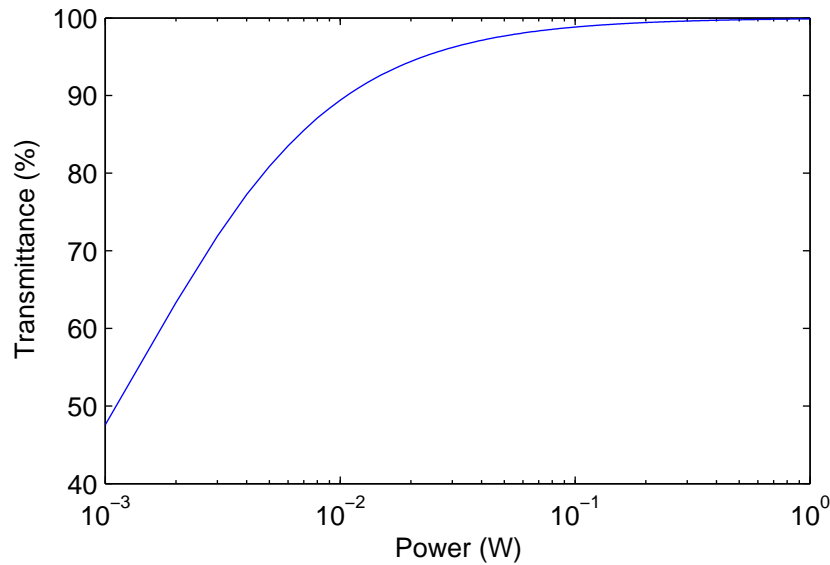


Figure 2.8: The power transmittance curve for instantaneous power passing through the SESAM.

2.3.3 Simulation results for a single fiber laser

Table 2.3.3 lists the parameter values used in our simulations which are based on the split-step Fourier method for solving the NLSE in this chapter. The fields evolve from an initial noise distribution and we examine the output after at least 2000 round trips in fiber cavities with lengths of about 8 meters. In this thesis, each round trip contains 24 discrete spatial steps for linear simulations and 48 discrete spatial steps

for nonlinear ones.

Table 2.1: Parameter values used in simulations.

Wavelength λ	1.545 μm
Saturation power P_{sat}	0.6 mW
Fiber propagation loss α	$1.8 \times 10^{-3} \text{m}^{-1}$
Group velocity dispersion β_2	-0.003 ps ² /m
Loss dispersion b	0.013 ps ² /m
Refractive index n	1.50
Unsaturated gain g_0	2.67m^{-1}
Saturation power for saturable absorber P_{SA}	300 mW
Unsaturated absorption for saturable absorber α_0	0.33mm^{-1}
Saturable absorber thickness L_{SA}	3.0 mm

Figure 2.9 shows the spectral and temporal results of a single 8.083m bidirectional laser cavity mode locked by a fast saturable absorber. The nonlinearity γ is as small as $0.0005 \text{m}^{-1}\text{W}^{-1}$ here, in order to avoid the instability which will be discussed in Chapter III. Unlike the cw operation, it is seen that there is a fixed spectral phase relationship among most longitudinal modes with a relatively high intensity. As a result, there is a temporal “burst” at the point when all these modes constructively interfere, and hence a mode-locked pulse with 2ps duration is generated inside the cavity. The pulse repeats itself every roundtrip.

2.4 Simultaneous beam combining and mode locking

2.4.1 Linear model

To study simultaneous beam combining and mode locking we follow the standard approach that uses discrete 50:50 directional couplers to create an interferometric system of coupled amplifier pairs in a composite cavity. A bidirectional Michelson

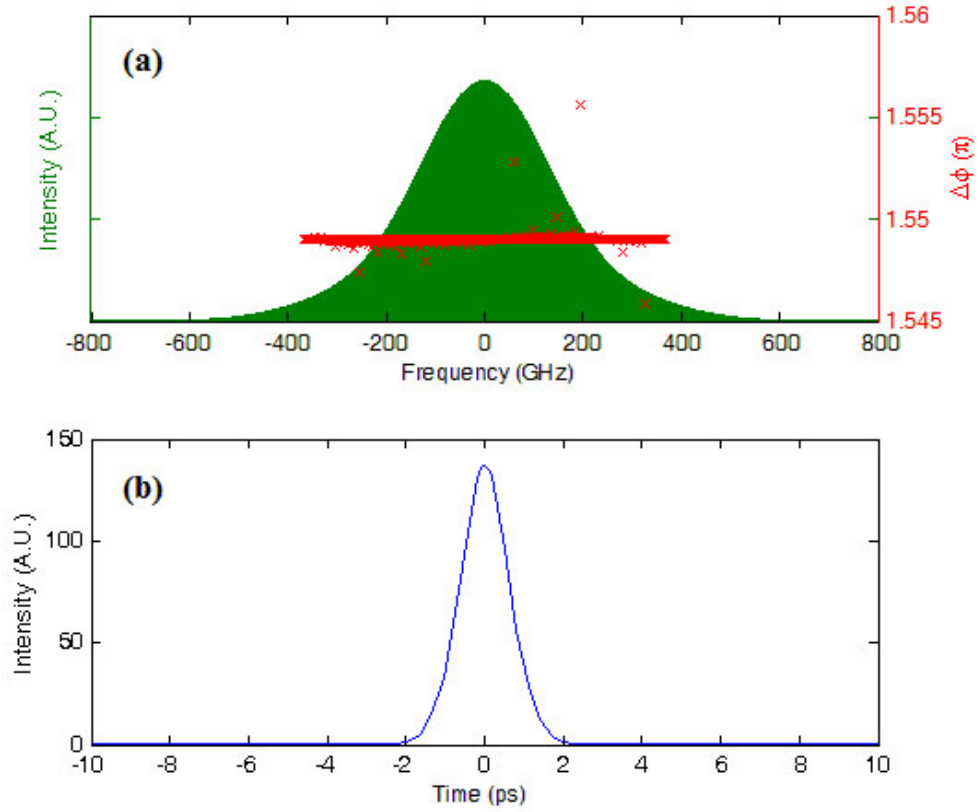


Figure 2.9: The simulation results for one mode-locked single fiber laser with a fast saturable absorber. (a) The spectral profile (green plots). The phase differences $\Delta\phi$ between two adjacent modes (red crosses) are almost constant. (b) The temporal pulse.

cavity is used here. In Fig. 2.10 the angle-cleaved port is a source of loss (no feedback) while the saturable absorbing (SA) mirror in Port 2 provides the mode locking mechanism and serves as the output coupler. Here the fiber amplifiers are of different lengths, arbitrarily chosen as 8.053m and 8.071m. The nonlinear coefficient is set to zero initially in order to focus on the essential mechanisms responsible for coherent combining and mode locking.

In the presence of a saturable absorber, the absorption in the system is low at high power and high if the power is below the saturation power. The system will thus discriminate against the low power cw state with random phases in favor of the solution in which the phases of adjacent modes are locked in a fixed relationship to

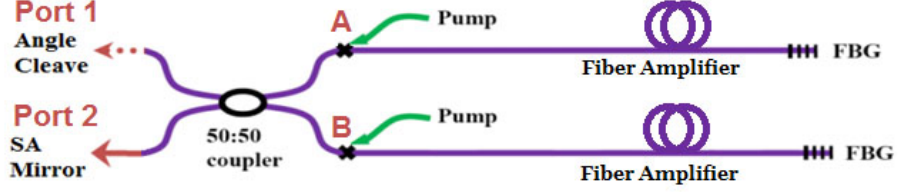


Figure 2.10: The Michelson interferometer structure for mode locking of two coupled fiber lasers. There is an angle cleave at Port 1 while a saturable absorber (SA) mirror is connected to the output port 2 to provide feedback and a mode locking mechanism.

generate high peak power pulses. Figure 2.11 shows the spectrum of the output of Port 2 in the presence of the saturable absorber. It can be seen that the spectrum in this case is much wider, with a bandwidth (FWHM) of about 100 GHz compared to the 20 GHz bandwidth under cw operation. The spectrum contains a large number of “lines”, each of which, upon magnification reveals a width of about 0.6 GHz. These lines are spaced by the cw beat frequency $\Delta f = c/(2n\Delta L)$, which in this example is 5.56 GHz as determined by the length difference.

For mode locking, the adjacent array modes need to be locked with a fixed phase relationship in order to generate a mode-locked pulse instead of cw output. Figure 2.11 also shows the phase difference between two adjacent array modes. For those frequencies around the array modes where there is a spike, the phase difference is fixed. Hence those phase-locked modes will constructively interfere with each other, leading to the mode-locked pulse output.

In time domain (Fig. 2.12), the output consists of packets of pulses at the round trip period $T = 2n\bar{L}/c$, with each packet containing a train of mode-locked pulses spaced by $\delta T = 1/\Delta f = 2n\Delta L/c$. For our chosen parameters each packet has a temporal width of 1 ns, which corresponds to the inverse of the 0.6 GHz spectral width of each spike in Fig. 2.11. Each of the mode-locked pulses in a packet has a width of 5 ps determined by the inverse of the 100 GHz bandwidth. Clearly the separation of pulses in each packet can be tuned by changing the fiber length difference ΔL .

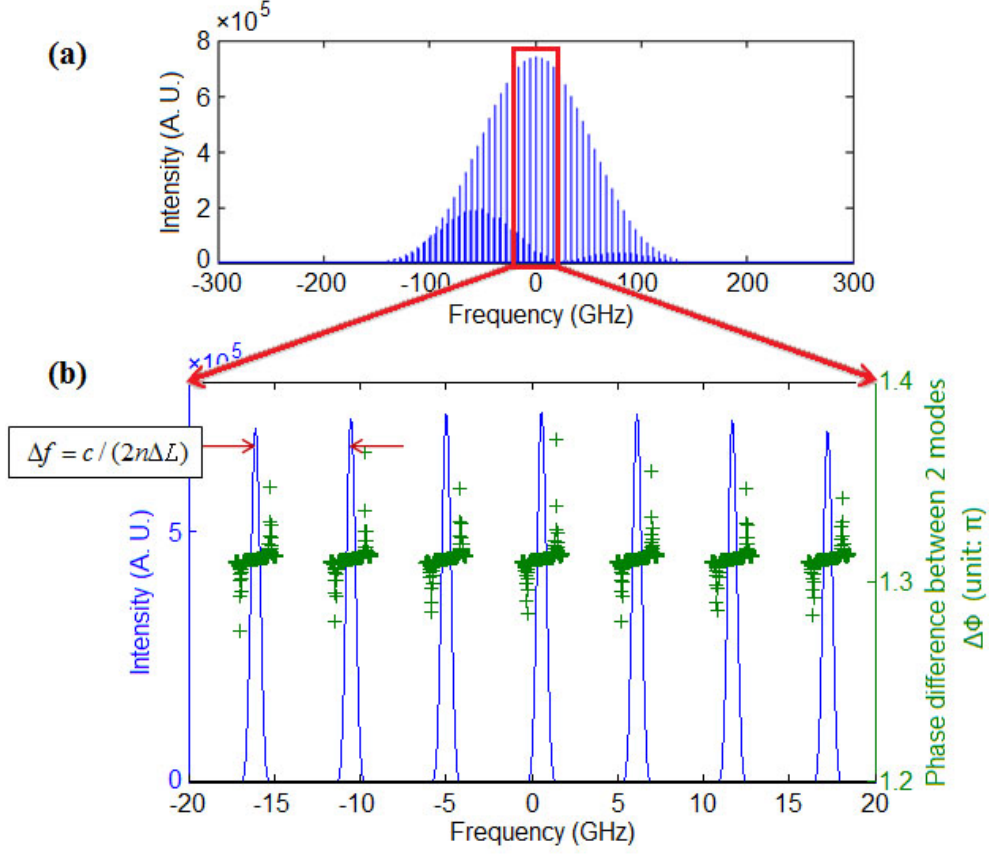


Figure 2.11: The spectral profile (a) of two-channel beam combining and mode locking with fiber lengths 8.053m and 8.071m at Port 2 without nonlinearity. A saturable absorber partial mirror is used at Port 2. In the zoomed figure (b), the phase difference between two adjacent longitudinal modes is also plotted (green crosses). The phase difference $\Delta\phi$ remains at around 1.31π for the frequencies around the array mode.

The average power out of Port 2 is 49.70 mW, representing 98.02% of the total power. Thus the combining efficiency remains high under mode locking conditions.

2.4.2 Comparison with experimental results

To compare with experiment, we apply our model to the work of Lhermite et. al. [62], in which packets of gigahertz pulse trains were generated through the coherent combining of mode-locked fiber lasers. Their experiment employed the Mach-Zehnder ring cavity configuration.

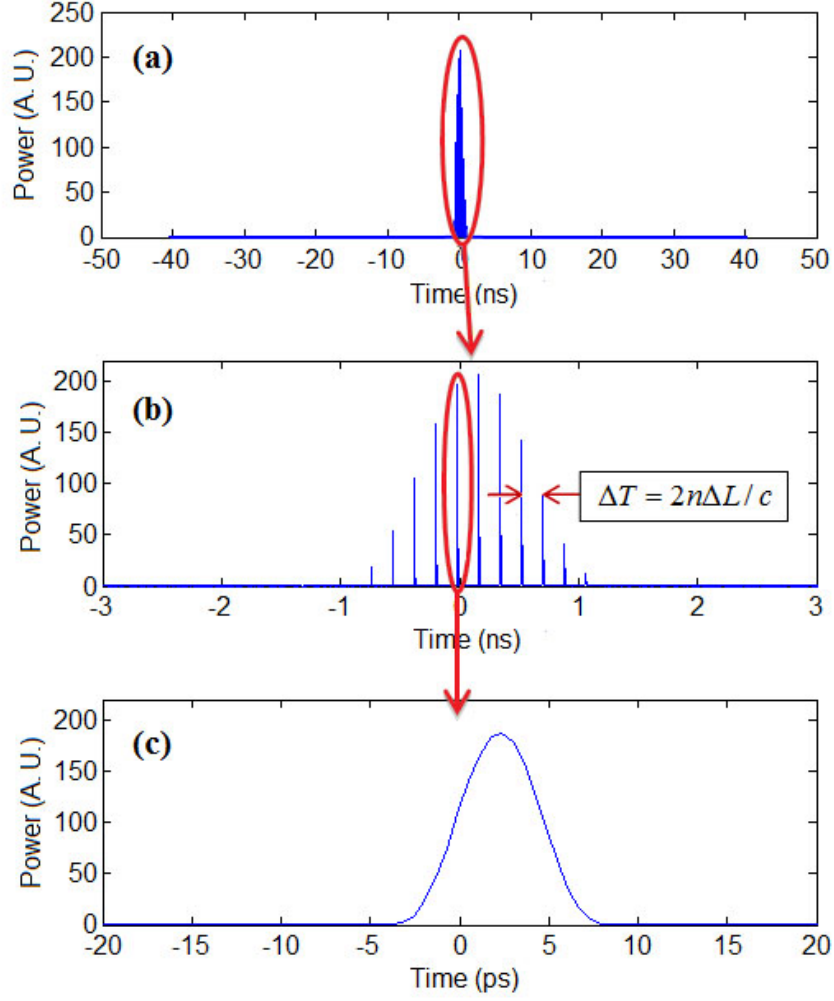


Figure 2.12: The temporal profile at Port 2 of two fiber beam combining and mode locking with lengths 8.053m and 8.071m without nonlinearity. The figures are zoomed in from (a) one roundtrip time to (c) one single pulse.

The interferometer modulates the individual laser spectrum with a beat frequency $\Delta f = c/\Delta L'$ thus creating pulse trains with interval $\delta T = \Delta L'/c$, where $\Delta L' = n\Delta L$ is the roundtrip optical path length difference. Each of the active fibers is 10m long and a delay line is inserted in one arm to permit a variable optical path-length difference $\Delta L'$ which we set at 5.1 mm, 3.5 mm, and 2.1 mm in accordance with the experimental values. (Note: According to the authors the smallest $\Delta L'$ used in the experiment was 2.1 mm, not 2.3 mm.) These length differences predict pulse repetition periods of 17 ps, 11.67 ps, and 7 ps, respectively. Figure 2.13 shows the

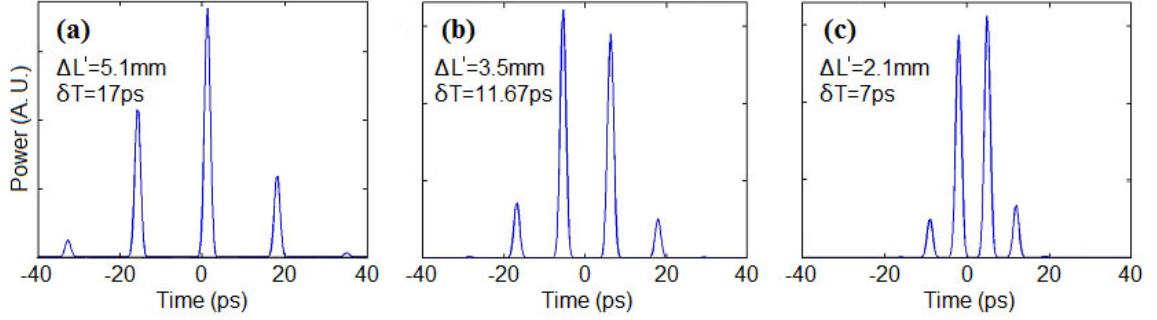


Figure 2.13: The pulse packet output for the Mach-Zehnder ring cavity structure shown in Fig. 5, in the absence of nonlinearity. The length differences between two channels are (a) 5.1 mm, (b) 3.5 mm and (c) 2.1 mm respectively.

simulated pulse packets. There is one of these packets within a round trip time of 120 ns. It is seen that the period of the pulse train within the packet decreases from 17 ps to 7 ps as the length difference is decreased, in agreement with the theoretical expression $\delta T = \Delta L'/c$. For these parameters the pulse heights within the train are not uniform.

In Fig. 2.14 we compare our simulated intensity autocorrelation results with the experimental measurements. Initially we found a systematic discrepancy with the published pulse periods. This discrepancy was resolved with new data supplied by the authors, which replaces the published periods with the values 17.19 ps, 11.88 ps, and 6.98 ps.

From the simulations about 90% of the total power of 100 mW emerges from the output port, indicating high combining efficiency. For very small length differences the pulse interval δT becomes comparable to the pulse duration and the mode locking breaks down. From the spectral viewpoint, such a small $\Delta L'$ leads to a Δf that is comparable to the effective bandwidth. As a result, only one array mode is left in the spectrum and thus there are not enough modes to be locked. We note that there is a relatively high background in the experimental autocorrelation compared to the

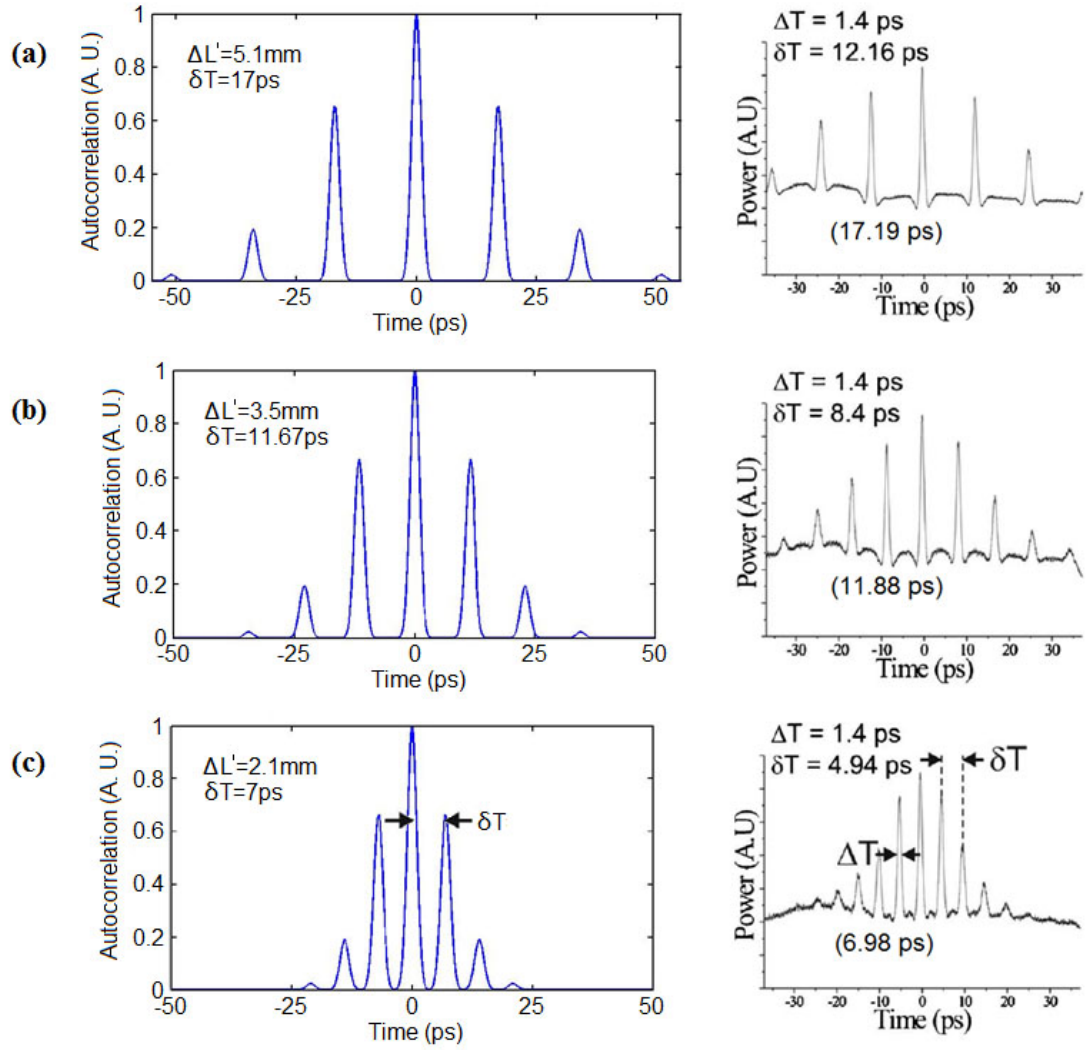


Figure 2.14: Comparison between simulation results (left) and the experimental results of Lhermite et. al. [8] (right) for (a) $\Delta L' = 5.1$ mm, (b) $\Delta L' = 3.5$ mm, and (c) $\Delta L' = 2.1$ mm. The corrected pulse separations are included in parentheses on the experimental plots. Experimental figure used by permission.

background-free results of the simulation. We will consider a possible cause in the next section.

2.5 Influence of nonlinearity

In order to elucidate the basic features of mode locking in coherently combined fiber lasers we neglected the nonlinear refractive index in the above simulations. We found very good agreement with the experimental results, except that our simulated autocorrelation plots do not show the high background levels seen in the experimental results. It is well known however, that at high pump levels the nonlinear index can lead to phenomena such as multiple pulsing in mode-locked fiber lasers. Here we include the Kerr nonlinearity and examine its effect on the spectral and temporal characteristics of mode locking. Fig. 2.15 shows the time series as well as the autocorrelation traces for $\gamma = 0.004 \text{ m}^{-1}\text{W}^{-1}$ and three values of length difference. The time series shows pulse splitting as well as the presence of irregular subpulses in between the main pulses. The autocorrelation trace displays a significant rise in background which can be attributed to the presence of these sub-pulses of essentially random heights. The exact nature of the pulse substructure is strongly dependent on the values chosen for nonlinearity, dispersion, and fiber length difference. The sub-pulse instability due to nonlinearity is worse for short fiber length differences.

Figure 2.16 shows the spectra and the spectral phase distribution for three length differences in the presence of nonlinearity. The uniform phase indicates that adjacent modes are successfully locked with a fixed phase difference even though the time series is highly irregular.

The rise in background with increasing nonlinearity is consistent with the increased SPM and frequency spread which makes it difficult for the fields in the two channels to maintain the phase relationship needed to minimize loss at the 50:50 directional coupler [12].

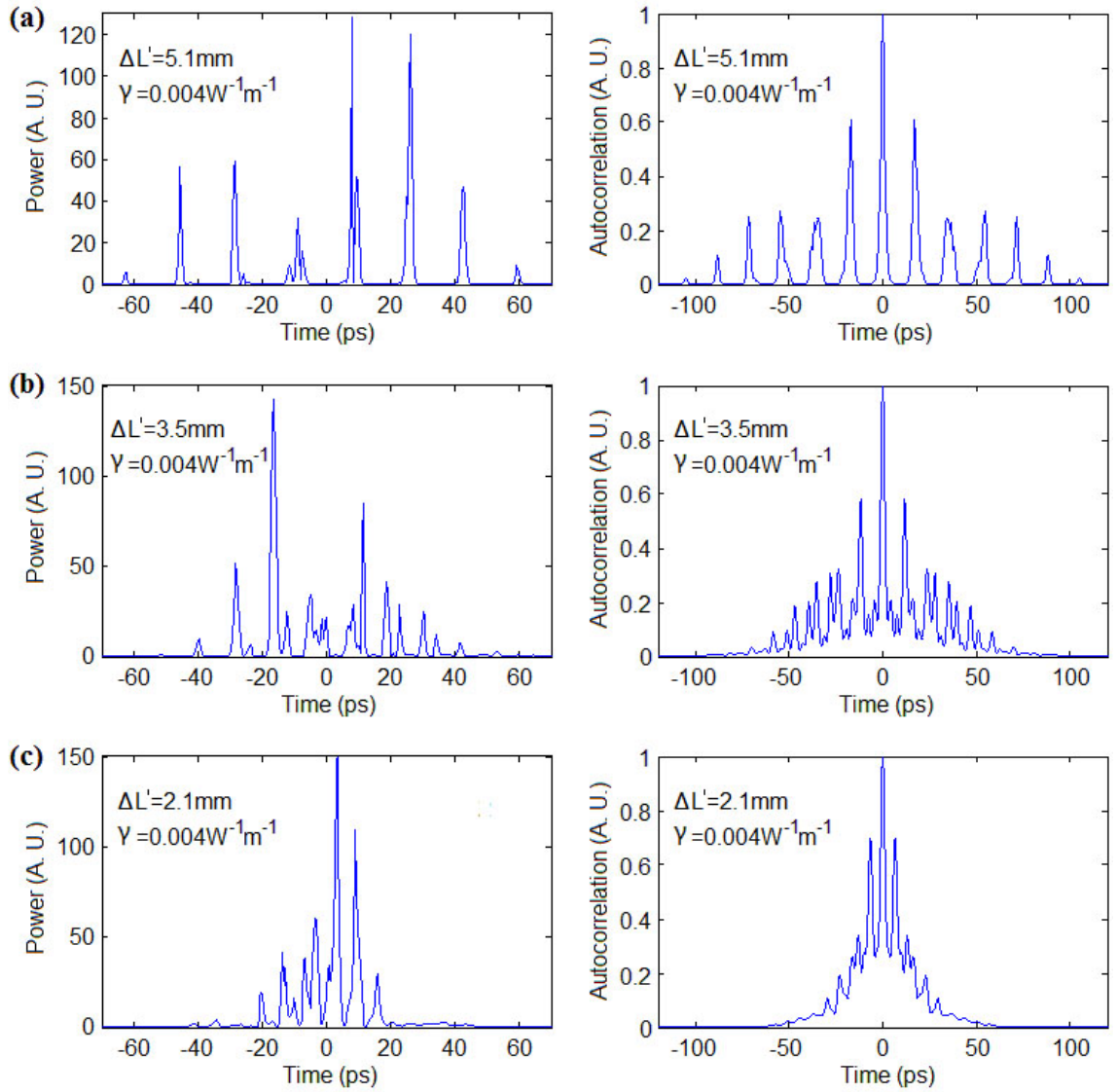


Figure 2.15: The time series (left) as well as intensity autocorrelation traces (right) for increased nonlinearity γ , with (a) $\Delta L' = 5.1$ mm, (b) $\Delta L' = 3.5$ mm, and (c) $\Delta L' = 2.1$ mm

2.6 Four-channel beam combining

To explore the possibility of mode locking larger arrays we extend our simulations to the 4-element fiber array shown in Fig. 2.17 with bidirectional Michelson structure. With four elements, there are 3 independent length differences and the array mode spacing is determined by the greatest common divisor (GCD) of these length

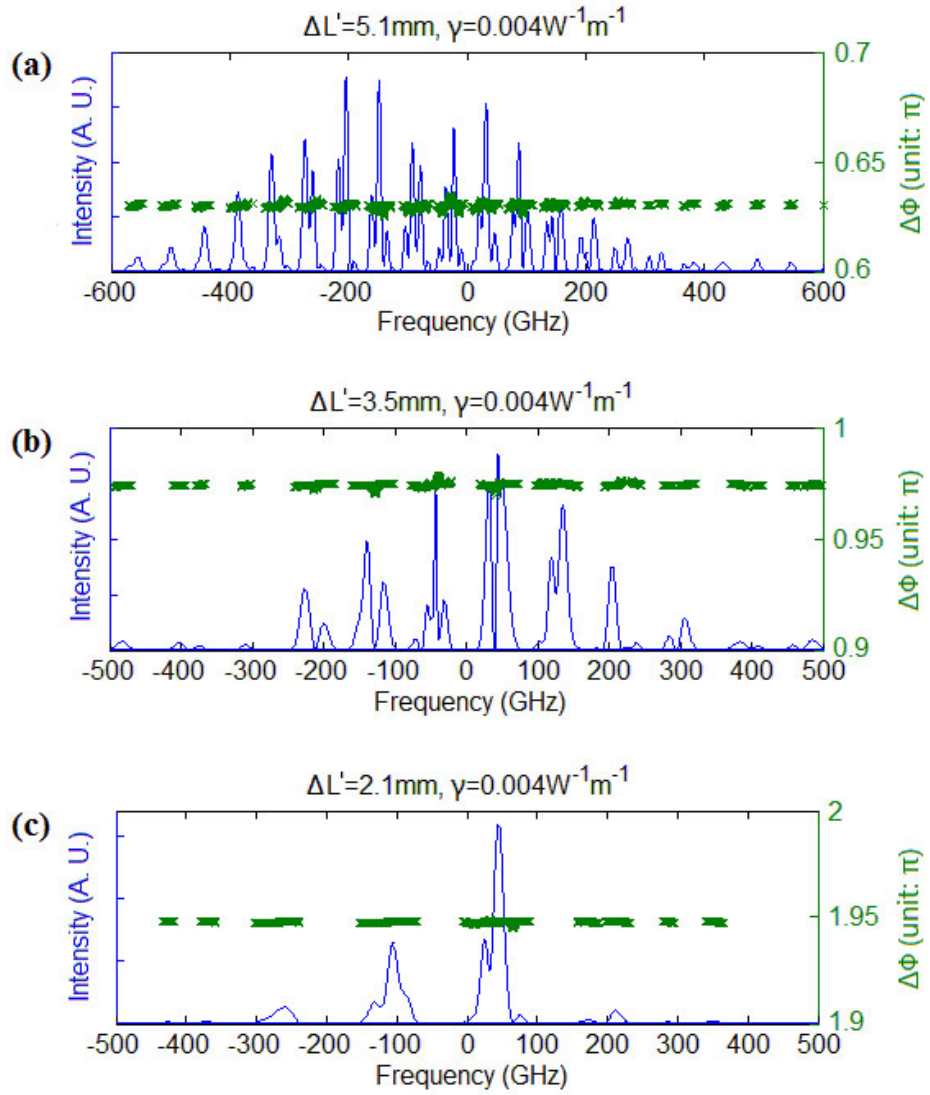


Figure 2.16: Frequency spectra (blue, solid curves) and spectral phase (green crosses) in two-fiber-laser beam combining and mode locking for $\gamma=0.004\text{m}^{-1}\text{W}^{-1}$, with (a) $\Delta L' = 5.1$ mm, (b) $\Delta L' = 3.5$ mm, and (c) $\Delta L' = 2.1$ mm.

differences [44, 46]. Strictly speaking the concept of a greatest common divisor is defined only for integers. Since the length differences are real numbers, we express them as integer multiples of the resolution of the length measurement, here taken to be 1 mm. The length differences are said to be commensurate when they have a non-trivial GCD. When the length differences are incommensurate, the allowed modes do not have any discernible periodicity.

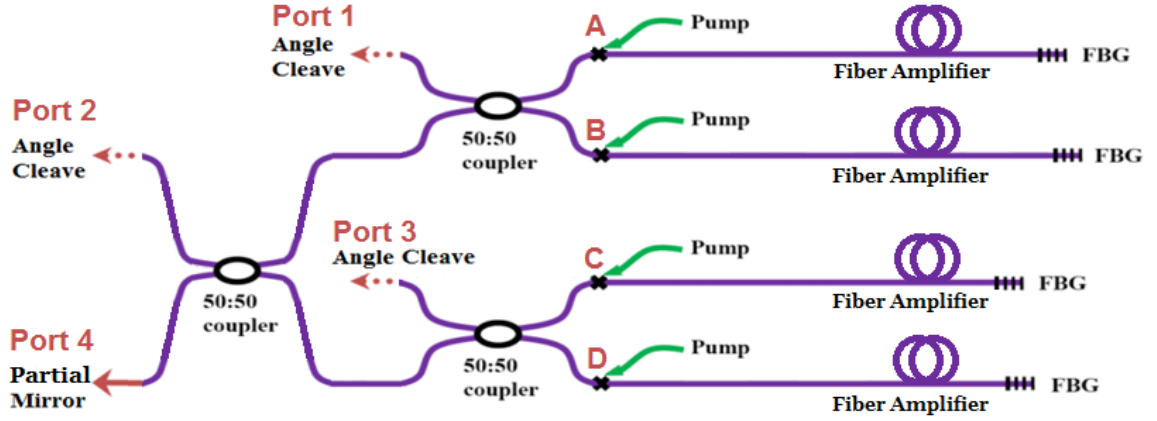


Figure 2.17: The structure of four-element fiber laser array with tree structure.

2.6.1 CW operation

We first consider cw operation without saturable absorber for a 4-element array with fiber lengths randomly chosen as 8.000 m, 8.011 m, 8.024 m and 8.041 m. The length differences are $L_{AB} = 11$ mm, $L_{CD} = 17$ mm, $L_{BC} = 13$ mm, for which there is no GCD except the trivial one, which in this case is 1 mm, the resolution of the length measurement. The implied mode periodicity is given by $\Delta f = c/(2n\Delta L_{gcd}) = 100$ GHz. This frequency separation is comparable to the bandwidth of the two-channel fiber laser array in Section 3.2. This means that for the chosen parameters only one array mode will exist within the net gain bandwidth under cw operation. Figure 2.18 shows the simulation result and it is clear from the spectrum that there is only one principal array mode, the other modes being at least 10 orders of magnitude lower. In the time domain the output is close to a sinusoid with a slow modulation.

It should be noted that since the actual fiber length differences are generally not rational numbers, the GCD is only approximate and thus the array modes will only be approximate modes with some coupling loss [12]. The closer the actual difference is to a multiple of the approximate GCD, the less coupling loss there will be, and vice versa. Since the laser system will be stabilized at the state with minimal loss, an optimal approximate GCD will be reached.

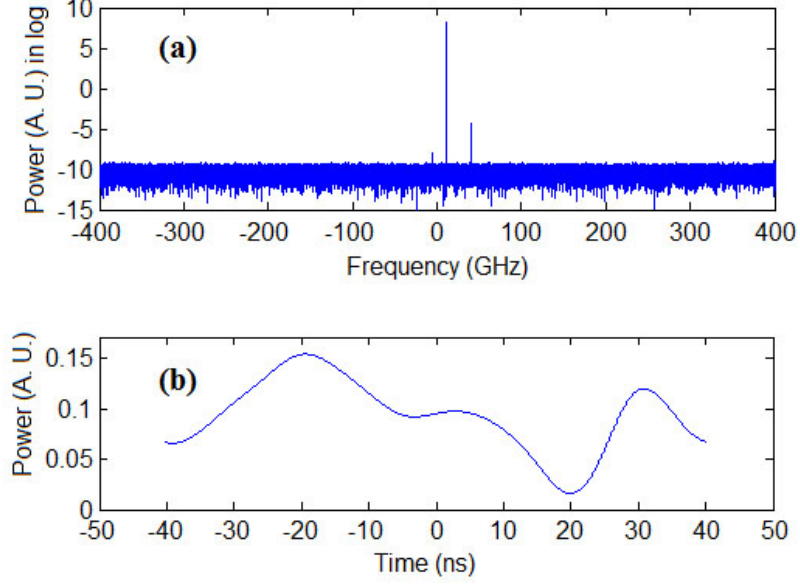


Figure 2.18: The spectrum in log scale (a) and temporal profile for one roundtrip time (b) for four-channel combining without saturable absorber. The four fiber lengths are independently randomly selected: 8.000 m, 8.011 m, 8.024 m and 8.041 m. Here the Kerr nonlinearity is $0.003 \text{ m}^{-1}\text{W}^{-1}$.

2.6.2 Four-channel beam combining and mode locking in fibers with incommensurate or commensurate lengths

In the simulation below, we use the same randomly selected fibers lengths as in the cw case: 8.000 m, 8.011 m, 8.024 m and 8.041 m. All parameters remain the same as in the simulation for Fig. 2.18, except that the partial mirror at Port 4 is replaced by a saturable absorber partial mirror. The nonlinearity is $0.003 \text{ m}^{-1}\text{W}^{-1}$. Figure 2.19 plots the spectral and temporal outputs. In the presence of the saturable absorber the spectrum exhibits a large number of modes as required for the formation of short pulses with the intensity needed to saturate the absorption. In the time domain, it is seen that a train of pulses with non-uniform separation is generated. The shortest separation between sub-pulses is about 10ps, corresponding to the 100 GHz array mode spacing in the cw case. The duration of each pulse is around 2.5 ps. The combining efficiency was computed to be 78%.

It is the requirement for beam combining that favors those array modes with the

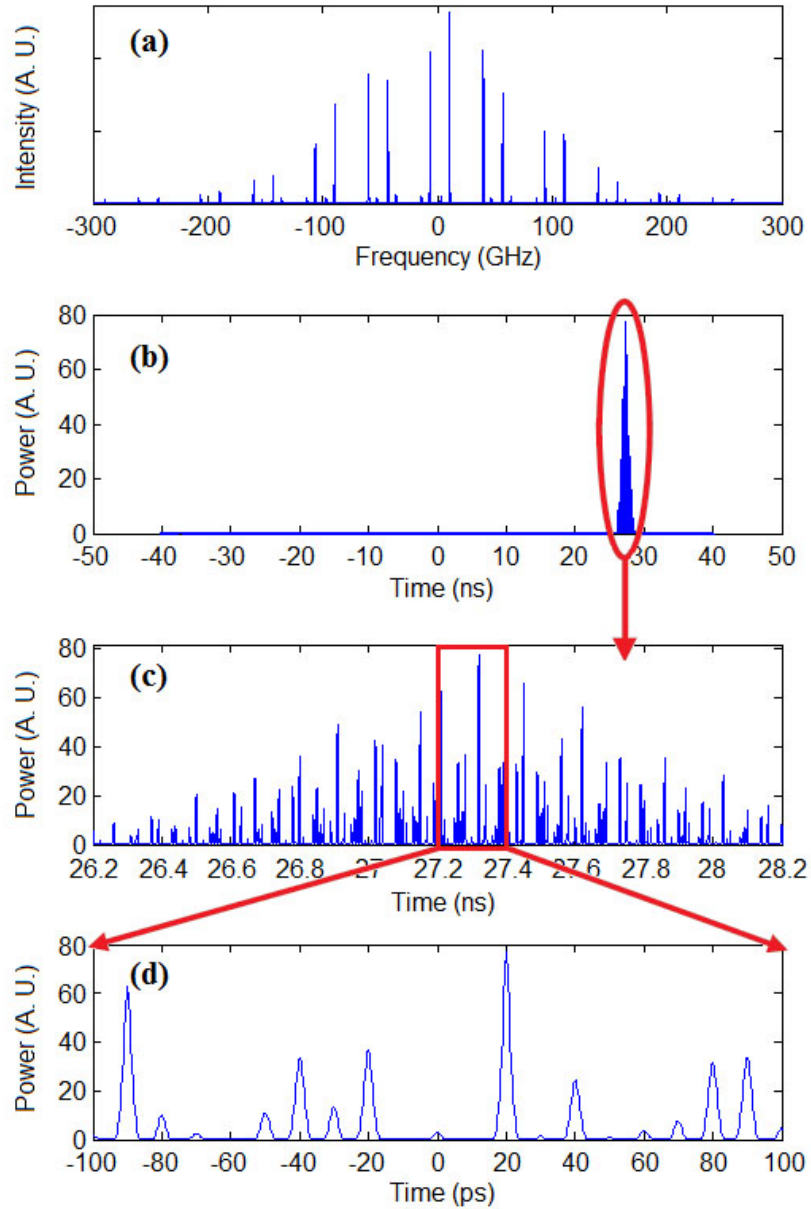


Figure 2.19: The spectral (a) and temporal profiles (b) for four-channel coupling with saturable absorber and with $0.003 \text{ m}^{-1}\text{W}^{-1}$ Kerr nonlinearity. The fiber lengths are 8.000 m, 8.011 m, 8.024 m and 8.041 m. (b) denotes one roundtrip time and it is further zoomed to (c) and (d).

least cavity loss. Nevertheless, with the growth of the number of channels, there will not be enough modes left no matter how broad the gain bandwidth is. A large number of modes are necessary to generate mode-locked pulses in order to pass through the saturable absorber and complete the roundtrip. Therefore, some non-array-modes

have to be selected as the optimized result with least total loss, from the interplay of saturable absorption and beam combining. Although they are not exact array modes, they are the closest to satisfying the minimum loss requirement. The passive combing system automatically stabilizes at this least loss working state. In this case, the shape of the pulse packet together with the pulse separation becomes non-uniform.

With randomly chosen lengths we obtained quasi-random mode-locked pulse trains from the 4-element fiber laser array. We now consider an array in which the elements are chosen such that their length differences are commensurate, i.e. they have a non-trivial greatest common divisor. Also, the length differences are chosen to be in the centimeter range so that the array mode spacing of roughly $c/(2n\Delta L)$ will be in the gigahertz range. This way there will be many more array modes within the gain bandwidth which should lead to improved mode locking.

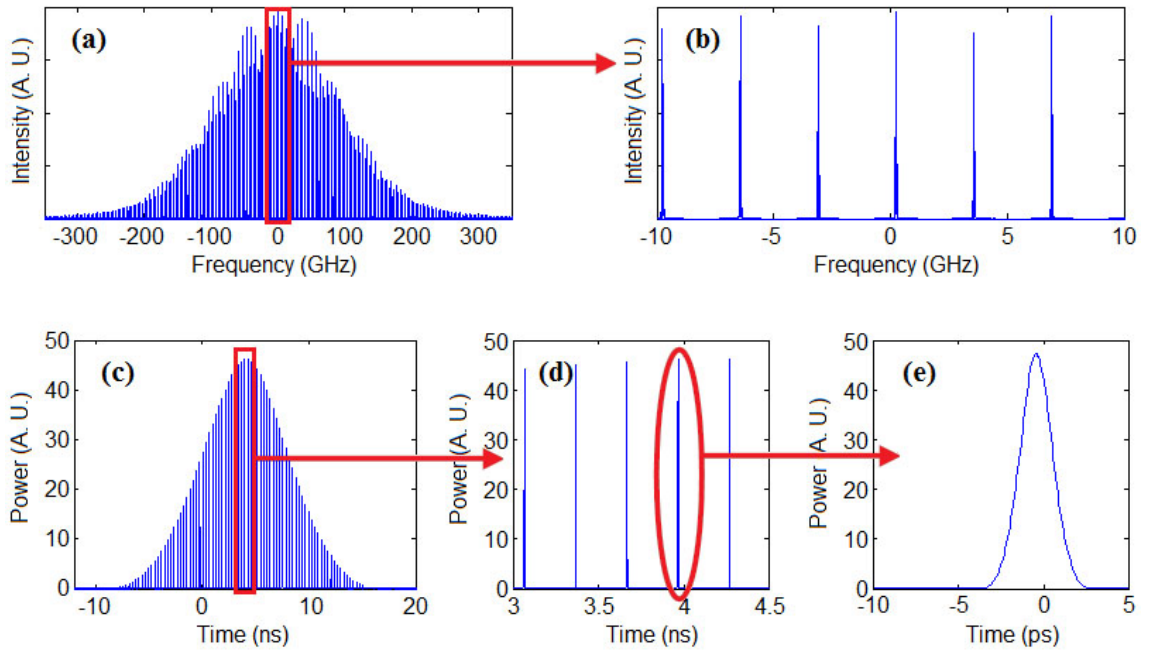


Figure 2.20: The spectral (a, b) and temporal (c, d, e) profiles for four-channel combining with saturable absorber and with $0.003 \text{ m}^{-1}\text{W}^{-1}$ Kerr nonlinearity. Here the four fiber lengths 8.050 m, 8.260 m, 8.200 m and 8.530 m are carefully designed for a 30 mm GCD for their differences.

For example, if we select 8.050 m, 8.260 m, 8.200 m and 8.530 m, the differences 210 mm, 60 mm, and 330 mm will have a greatest common divisor of 30 mm, which leads to an array mode separation of 3.33 GHz. As a result there will be many more array modes within the bandwidth range to be locked to produce short mode-locked pulses. The simulation result for this case is plotted in Fig. 2.20. It is seen that the pulses within a packet are uniformly spaced with a repetition rate of 3.3 GHz. The calculated combining efficiency of 91% is higher than in the incommensurate case.

Next we consider an intermediate situation where the GCD is relatively small but still non-trivial, e.g. 5 mm. Here the fiber lengths are selected as 8.000 m, 8.015 m, 8.040 m, and 8.060m. Their length differences are 15 mm, 25 mm, and 20 mm respectively. The array mode separation is calculated to be 20 GHz. Consider a spectrum from -150 to 150 GHz, there will be approximately 15 array modes, which is not as sparse as the non-commensurate case. However, this number is not enough yet for mode locking to produce high peak short pulses. In the simulation result shown in Figure 2.21, the spectral spikes are distributed mainly in two periods: 20 GHz corresponding to the array mode separation by $L_{gcd} = 5$ mm, and 6.7 GHz corresponding to the 15 mm fiber length difference. In the temporal profile, there are 3 packets per roundtrip. In each packet, there are uniform pulse separation but irregular pulse amplitudes in the center, and non-uniform separation in the tails.

2.6.3 Combining efficiency in four channel beam combining

The data of four-channel beam combining efficiency are listed in Table 2.6.3 based on our simulations. For the bidirectional tree-structure, the mode-locked operation for incommensurate lengths has a much lower combining efficiency than others, especially with the growth of nonlinearity. Since a high combining efficiency is the key for scaling up the fiber array, it is interesting and important to analyze the reason for the efficiency drop.

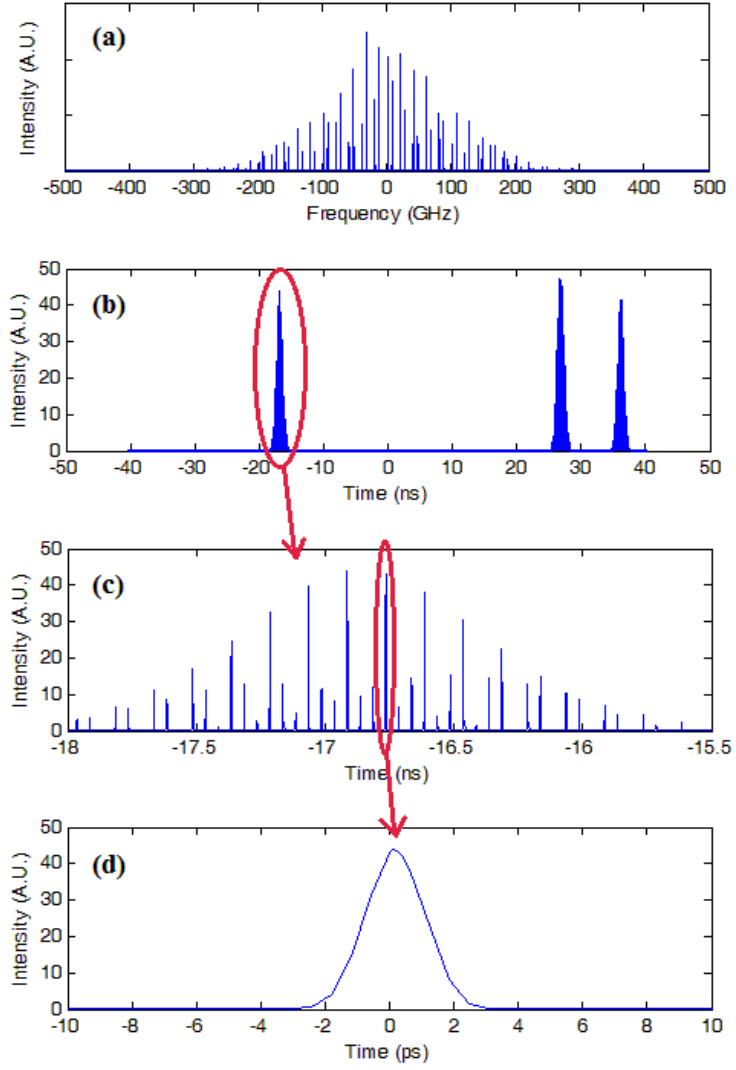


Figure 2.21: The spectral (a) and temporal (b, c, d) profiles for four-channel combining with saturable absorber and with $0.003 \text{ m}^{-1}\text{W}^{-1}$ Kerr nonlinearity. The fiber lengths 8.000 m, 8.015 m, 8.040 m and 8.060 m are designed for a 5 mm GCD for their differences, which is in between the trivial 1 mm and non-commensurate 30 mm.

There are 3 directional couplers in our bidirectional tree structure for 4 fibers. With the theoretical transfer matrix model for 50:50 directional couplers in Eq. (2.4), it is easy to show that the E-field at loss ports Port 1-3 and output Port 4 can be

Table 2.2: Comparison on combining efficiencies for different setup.

	$\gamma = 0.0007\text{W}^{-1}\text{m}^{-1}$	$\gamma = 0.003\text{W}^{-1}\text{m}^{-1}$
CW operation (8.000m, 8.011m, 8.024m and 8.041m)	92.29%	92.28%
Mode locking (8.000m, 8.011m, 8.024m and 8.041m)	84.87%	77.96%
Mode locking (8.05m, 8.26m, 8.20m and 8.53m)	95.63%	90.93%

represented as:

$$E_1 = \frac{1}{\sqrt{2}}(E_A - iE_B), \quad (2.9)$$

$$E_2 = \frac{1}{2}(-iE_A + E_B - E_C - iE_D), \quad (2.10)$$

$$E_3 = \frac{1}{\sqrt{2}}(E_C - iE_D), \quad (2.11)$$

$$E_4 = \frac{1}{2}(-E_A - iE_B - iE_C + E_D), \quad (2.12)$$

where E_A , E_B , E_C and E_D are the E-fields at position A, B, C and D respectively (see Fig. 2.17). Therefore, if we have a good phase relationship with $\phi_A - \phi_B = \pi/2$, $\phi_A - \phi_C = \pi/2$ and $\phi_A - \phi_D = \pi$, then the output magnitude $|E_4|$ will reach its maximum of $\frac{1}{2}(|E_A| + |E_B| + |E_C| + |E_D|)$. From Fig. 2.22, the phase locking looks good at the time of each pulse peak for 4 fibers with random lengths and saturable absorber.

On the other hand, for a good combining efficiency, we need also minimize the output at the loss port $|E_1|$, $|E_2|$ and $|E_3|$. Since there is still good phase relationship maintained among four channels for coherent beam combining, approximately $\phi_A - \phi_B = \pi/2$, $\phi_A - \phi_C = \pi/2$ and $\phi_A - \phi_D = \pi$, we have $|E_1| \approx ||E_A| - |E_B||$, $|E_2| \approx ||E_A| + |E_B| - |E_C| - |E_D||$, and $|E_3| \approx ||E_C| - |E_D||$. We need keep the magnitudes

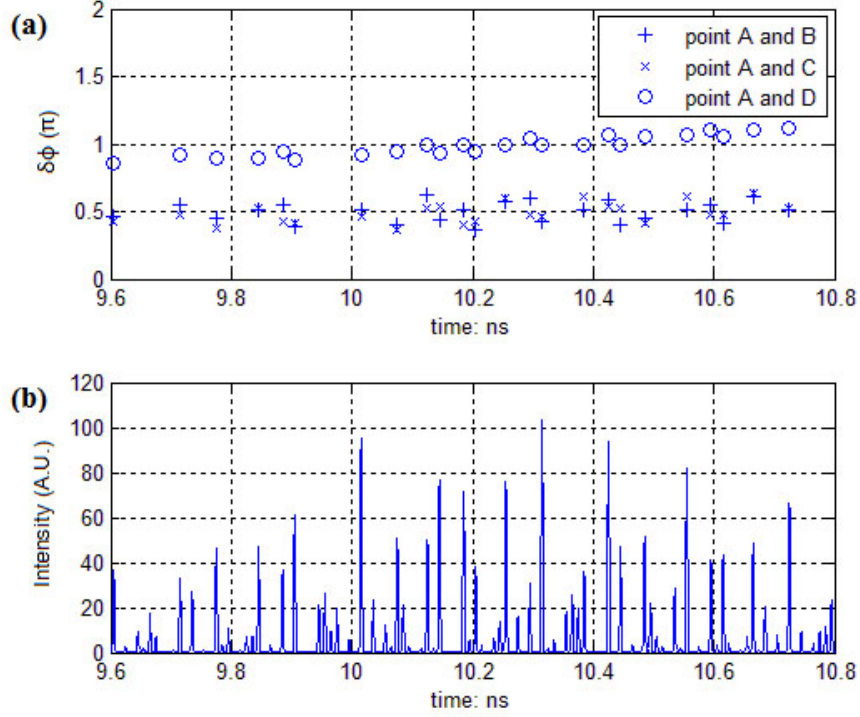


Figure 2.22: (a) The measured inter-cavity phase differences between points A and B, points A and C and points A and D, at the time points when there is a mode-locked pulse. (b) A temporal pulse packet from incommensurate lengths. At the time when a pulse is generated, the four channels maintain a good relative phase relationship for high efficiency.

$|E_A|$, $|E_B|$, $|E_C|$ and $|E_D|$, as close to each other as possible to minimize the power leaking through angle cleaves.

From Fig. 2.23, the temporal pulse packet profiles look almost identical for all fiber channels in shape, but with different time shifts. At every time point, the E-field intensity in each fiber varies irregularly. When there is a strong pulse peak at point A, the pulse peak at point B, C, D may be weak, etc. The peaks of the pulse packet in each fiber channel are not synchronized. The E-field intensity mismatch is distributed across the whole pulse train, from the beginning to the end. After integration over one round-trip time, such mismatch accumulates and hence $|E_1|$, $|E_2|$ and $|E_3|$ are not negligible thus reducing the total combining efficiency. If we measure the time shifts between these channels, the difference between fiber A and B is 0.11 ns, the

one between B and C is 0.13 ns, and the one between C and D is 0.17 ns. The length difference between fiber A and B is 1 mm, and between B and C is 13 mm, and between C and D is 17 mm. That is, the time shift between any two channels is exactly their roundtrip time difference as beating, i.e. $\delta T_{ij} = 2n\Delta L_{ij}/c$. Because the fibers are non-uniform in their lengths, the round trip time in each fiber is different. Hence the time shift cannot be avoided.

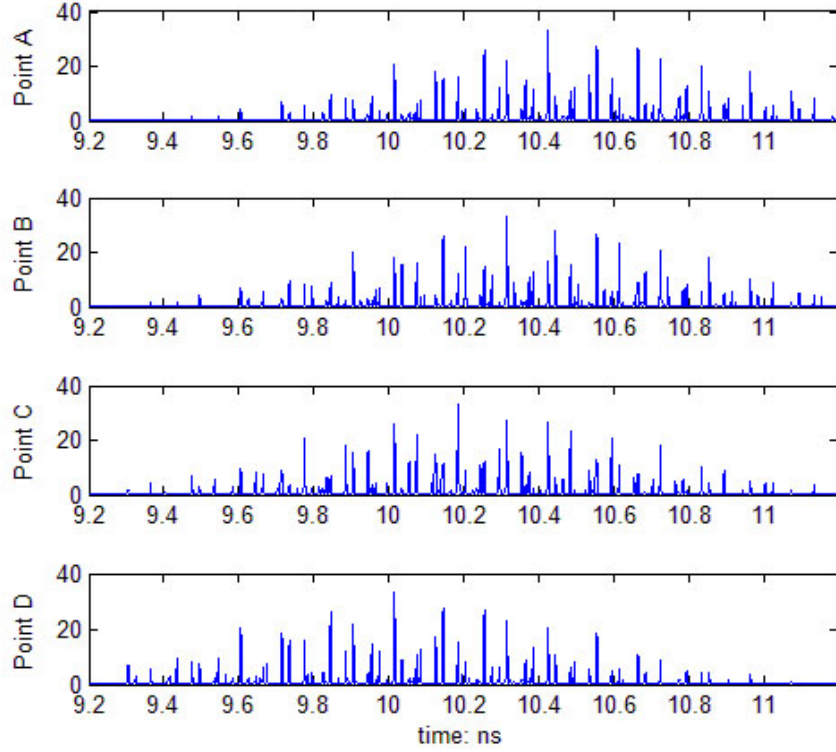


Figure 2.23: The temporal plots for the observation on points A, B, C, and D respectively, i.e. the entrances of the directional couplers. The y-axis represents the temporal optical intensities in each fiber.

For cw operation, the different time delay effect is not obvious because of the continuous nature of cw wave. As a result, the beam combining efficiency for cw operation is much higher. Also, for mode locking with commensurate fiber lengths, the shape of the pulse packet is very regular. Unlike the incommensurate cases, the pulse intensities for adjacent pulses do not vary too much. Therefore commensurate fiber lengths have a higher efficiency for coherent beam combining.

2.7 Conclusion

In this chapter, we have presented a dynamic model of simultaneous passive coherent beam combining and passive mode locking for coupled fiber lasers, in the presence of a saturable absorber. The presence of a saturable absorber in the composite cavity results in the generation of packets of mode-locked pulse trains. The results show, in agreement with experiment, that a pair of coherently combined fiber lasers will produce packets of mode-locked pulses whose repetition rate can be tuned by varying the length difference between the fibers.

For larger arrays, beam combining decreases the density of modes while mode locking requires a number of modes to be locked for a high peak to pass through saturable absorption. Such interplay of saturable absorption and beam combining determines that some non-array-modes left in the spectrum in the steady state, with the least total roundtrip loss. Since these surviving non-array-modes are neither regular in shape nor have a unique separation, the temporal packet becomes random unless the fiber lengths are chosen carefully such that their differences are commensurate (where there are still enough array modes to lock). The combining efficiency of the array drops as a consequence of the unsynchronized irregular pulse packet in each channel.

CHAPTER III

Dissipative Solitons in Fiber Laser Array With Normal Dispersion

3.1 Introduction

Optical solitons generated by the balance between anomalous dispersion and Kerr nonlinearity are widely applied in ultrafast optics and optical communications. However, the energy carried by each soliton is limited in fiber lasers to avoid wave-breaking [28]. Recently, there is much research interest focusing on dissipative solitons [18, 19, 92–96], a new class of stably mode-locked pulses with both amplitude and phase balances, which can be generated under normal dispersion conditions. Unlike transform-limited pulses, these chirped dissipative solitons are more stable in shape and do not suffer from wave breaking at high energies [18, 94–100]. With dissipative solitons in normal dispersion, fiber lasers can output pulse energies an order of magnitude higher than prior soliton fiber lasers, and therefore provide a path towards higher pulse energies. After pulse compression of these chirped pulses, high peak power can be achieved [94, 98]. The all-normal-dispersion fiber laser [97–101] simplifies the cavity design a lot, without using any dispersion map with anomalous dispersion sections [22, 93]. It has become a practical method to design fiber cavity for dissipative solitons. To date, most dissipative solitons are generated and

operated within one isolated fiber amplifier [18, 19, 92–100]. With directional couplers, fiber amplifiers can be combined pair-wise in a tree structure to form a passive interferometric fiber array [44, 45, 62, 64]. Such passive coherent beam combining enables the scaling of output power from two or more channels in an array without too complicated configuration.

In order to obtain robust pulses with clean pulse shape and high energy, the possibility of scaling up multiple dissipative solitons through passive combining is worthy of investigation. To the best of our knowledge, our work is the first to combine dissipative solitons from two active fibers through passive coherent beam combining in normal dispersion regime. The simulation results show that the output energies from two independent channels are combined together with a high efficiency. Comparisons are made among different nonlinearity parameters, in order to show the stability of the dissipative soliton solution and its robustness with regard to nonlinearity.

One useful application for mode-locked pulses is clocking. However, it is not easy to produce multiple and uniformly distributed mode-locked pulses per roundtrip to increase its repetition rate in single-channel cavity. In the fiber array, a mode-locked pulse packet with multiple pulses with a fixed interval is generated every round trip. Thus the repetition rate becomes high, tunable and stable [62, 64]. In this paper we also present a possible approach to generate robust pulse trains with two different repetition rates simultaneously. One is the repetition rate for pulses which is much faster than the roundtrip traversal, and the other one is a relatively slow amplitude modulation which is comparable with the roundtrip rhythm. For commensurate fiber lengths, the modulation envelope degenerates and a regular and uniform pulse train with high repetition rate is produced.

3.2 Theory of dissipative solitons

Dissipative solitons are stable and localized solutions in the dissipative system. In its dynamics, balances are achieved not only between the phase modulations caused by nonlinearity and dispersion, but also between the amplitude modulations from nonlinear gain and loss. Unlike conventional solitons, dissipative solitons may arise even for normal dispersion in combination with a positive Kerr nonlinearity, as long as there is a spectral bandpass filtering effect together with optical amplification to compensate for the filter loss.

3.2.1 Solitons and dissipative solitons

The discovery of optical solitons dates back to 1973, when Akira Hasegawa and Fred Tappert first suggested that solitons could exist in optical fibers [102, 103], as a balance between SPM and anomalous dispersion, and that these solitons are governed by the NLSE [2, 16]. Both bright and dark solitons are predicted based on the mathematical models. In 1980, the first experimental observation of the propagation of a bright soliton was made in an optical fiber. Since then, the theoretical and experimental developments on solitons have aroused interest from many scientific and engineering areas.

Because of the Kerr nonlinearity and chromatic dispersion, a short optical pulse usually cannot maintain its temporal and spectral shape unchanged during its propagation. However, under certain circumstances, the effects of positive Kerr nonlinearity (as for most media) and anomalous dispersion can exactly cancel each other, so that the temporal and spectral shape of the pulses can be preserved after very long propagation distances [13, 15]. In a bright fundamental soliton in lossless medium, assuming there is no higher-order dispersion, the temporal shape of the pulse has to be an unchirped sech profile with constant width and intensity.

The soliton solutions of the NLSE are remarkably stable. With any initial pulse

shape, a fundamental soliton solution can be automatically achieved as the initial pulse sheds the rest energy into a weak background. The intensity in the background wave is too low for significant nonlinear effects or chromatic dispersive temporal broadening [2]. At the same time, solitons are very stable against changes of the medium and fiber parameters. Therefore, solitons can adapt their shape to some slowly varying fiber parameters. Soliton mode locking is frequently used for the generation of femtosecond pulses. The soliton shaping effects play a dominant role there, shortening the pulse duration to be even significantly shorter than the response time of the absorber. Soliton mode locking allows for significantly stronger nonlinear phase shifts by SPM, which could otherwise make the pulses unstable. When used in the appropriate regime of nonlinear phase shifts, soliton mode locking normally allows for very high pulse quality with low chirp.

Although it has many advantages, solitons are conservative solutions in lossless medium, where the pulse exchanges no energy with the fiber. In a dissipative system with gain and/or loss, it becomes different and a much wider range of phenomena becomes possible. Strictly speaking, no conservative solitons can exist in fiber amplifiers, because there is at least always a positive laser gain. However, if the dominant pulse shaping effects are the conservative ones (anomalous dispersion canceling the positive Kerr nonlinearity), we may still consider them as conventional solitons instead of dissipative solitons.

This extension of the conventional soliton concept implies that the exact balance between gain and loss plays a dominant role in the dissipative dynamics, for producing stationary localized solutions. It is useful to highlight one significant difference between conventional conservative solitons and dissipative solitons. In order to be stationary while keeping continuous energy exchange with environment, dissipative solitons have internal regions that extract energy from outside, as well as other internal regions to release energy. A stationary dissipative soliton therefore holds the

live redistribution of energy between various parts inside. Such internal energy flow leads to a non-uniform phase distribution in its temporal profile, in contrast to the constant nonlinear phase profile of a stationary conservative soliton.

An important feature for a dissipative soliton is that besides the saturable laser gain, the amplitude modulation balance is reached mainly by some dissipative effects such as saturable absorption, spectral filtering, etc. A passively mode-locked fiber laser cavity contains not only the pumped fiber, but also other optical components including a saturable absorber and a spectral bandpass filter. A stable dissipative soliton solution comes from stable cavity parameters with the required dissipative elements. Therefore, if these effects are not too strong and can be considered a uniformly distributed model within the fiber, then the circulating pulses will be usually analyzed as dissipative solitons.

3.2.2 Wave breaking

In the case of fiber lasers, soliton mode locking in the picosecond regime works well by the balance of nonlinear SPM and negative GVD phase shifts, but usually limits the pulse energy achievable up to nJ order in standard fiber by the soliton area theorem, whereas Kelly sidebands occur in the femtosecond regime. With SPM, the nonlinear phases are proportional to the temporal intensities. With the increase of pulse peak intensity and in the presence of chromatic dispersion, the excessive nonlinear phase shift can make an optical soliton distorted, altering the pulse shape and generating irregular sub-pulse noises around its main peak.

When a short pulse is temporally confined in ultrashort duration, high intensities always make the resulting nonlinear phase shift a major concern in power scaling-up for mode-locked fiber sources. A high-energy pulse may accumulate a too high nonlinear phase shift to get balanced by dispersion. It will put a distortion on the pulse profile, which eventually break the pulse. Such effect is well known as wave-

breaking [29, 30, 65, 104]. Attempts to produce high energies in single-mode-fiber lasers always lead to multiple-pulsing or other instabilities.

Wave-breaking is the fundamental limit to pulse energy for nonlinear fiber lasers, and it is the very motivation why we have to use coherent beam combining instead of a single fiber channel to get the high energy pulses in this thesis. To avoid wave-breaking by excessive nonlinear phase shift, we have to put a limit on the pulse intensity in each fiber. Nonlinear effects can be reduced by increasing the average pulse duration [27, 95, 105]. An effective approach is to chirp the pulse in the fiber so its duration gets stretched, and therefore its peak intensity is lowered for a fixed pulse energy. Then the chirped pulse with high energy can be compressed again for high intensities by removing the chirp, outside the fibers after outputting. The word “breathing” is used to describe the process that pulse first gets chirped and stretched, and then dechirped and compressed.

With positive GVD and SPM, the phase shifts are added together and there will be a considerably large chirp. Therefore with the same pulse energy condition, the highly chirped pulses in normal dispersion are more resistant to wave-breaking than the ones in anomalous dispersion. In other words, although anomalous dispersion leads to ultrashort mode-locked pulses with little chirp, the system operated under normal dispersion is more robust and hence can support about an order higher pulse energies without wave-breaking. Thus it becomes important to explore the mode-locked dissipative solitons in positive GVD regime.

3.2.3 Comparison with similaritons

Similaritons are self-similar asymptotic solutions propagating in nonlinear fiber amplifiers with normal chromatic dispersion [20–22, 93, 106–108]. The self-similar optical pulses usually have both temporal and spectral intensity profiles with a parabolic shape as well as an up-chirp. It is parabolic not only near the pulse peak, but also

well towards the wings up to the point where the intensity goes to zero. Along the active fiber amplifier, the parabolic pulse grows self-similarly in both width and magnitude, no matter its temporal or spectral profile. Unlike solitons where both pulse durations and pulse shapes are preserved, the similariton pulses maintain their shapes asymptotically and their duration keeps increasing. As its name implies, a similariton is self-similar until it reaches gain saturation or gain bandwidth, or arrives at the boundary of the fiber amplifier.

The chirped parabolic pulse is the asymptotic solution for long propagation distances in active fibers. After growing in a sufficiently long propagation length, the resulting pulse parameters get decoupled with the shape or duration of the seeding pulses, because of the self-similar nature. Theoretically, the peak power and duration of the pulse after a long propagation length depend only on the energy of the seeding pulse. Parabolic similaritons have a number of remarkable properties, and particularly important in the context of fiber amplifiers for generating high-energy ultrafast pulses. Although similaritons come from fiber amplifiers without cavity boundary conditions at the beginning, people have broadened its concept to normal dispersion nonlinear laser cavities by either adding another section of anomalous dispersion to compensate the chirped phases [22, 93, 97], or using a narrow bandwidth filter to cut off the chirped frequencies [97, 106].

The latter approach is easy to get confused with dissipative solitons. A self-similar asymptotic solution can be produced in active fibers with nonlinearity, normal dispersion, spectral filter and saturable absorber, almost the same condition as dissipative solitons. However, unlike dissipative solitons, a similariton decouples from fiber parameters and grows self-similarly in both spectral and temporal domains, relying on a local attracting mechanism. Because of its own nature, similaritons have large temporal and spectral breathing ratios when produced inside the laser cavity, and a very narrow bandwidth spectral filter need be inserted in the cavity for the roundtrip pe-

riodical boundary conditions. The effect of spectral filtering is so strong and lumped at one point of the roundtrip, and cannot be modeled as a distributed element which is necessary for dissipative solitons. In our paper, we focus on dissipative solitons because we limited the calculation bandwidth for computational efficiencies, and there is not enough room for a large spectral breathing to support similariton simulations.

3.3 Quantitative model of dissipative solitons

In passive mode locking, the most important physical processes in shaping a pulse include accumulated linear phases from GVD, nonlinear phases from SPM, amplitude modulation through saturable absorption, and bandpass spectral filtering. They are all critical for the formation of dissipative solitons. A satisfying quantitative model needs to take these physical effects into account.

Compared with conventional solitons which are conservative, the dissipative effects make it possible to derive a solution in a normal dispersion regime where the output pulses are highly chirped. An all-normal-dispersion fiber laser [97–100] is considered one of the simplest structures to produce dissipative solitons, where the breathing of the pulses is reduced as a result of the absence of a dispersion map. Another feature of an all-normal-dispersion fiber is that the stable solutions exist with a wide variety of parameters, leading to several different temporal and spectral shapes [94, 98].

3.3.1 Cubic-quintic complex Ginzburg-Landau equation

The Haus master equation, also known as the cubic Ginzburg-Landau equation (CGLE), has been used widely to model mode-locked laser behaviors for the past two decades with significant success [16, 81, 82, 109–112]. As an extension of NLSE, a cubic real term for saturable absorption is included as self-amplitude modulation. However, some typical stable dissipative soliton solutions with steep edges in an all-normal-dispersion fiber could not be directly derived from the master equation, but

from one of its generalizations: the complex cubic-quintic Ginzburg-Landau equation (CQGLE) [82, 94, 113]. In the CQGLE, the SPM term is still cubic, while the saturable absorption term is real quintic. A typical CQGLE can be written as:

$$\frac{\partial E}{\partial z} = gE + \left(\frac{1}{\Omega} - i\frac{D}{2}\right)\frac{\partial^2 E}{\partial t^2} + (\alpha + i\gamma)|E|^2E + \delta|E|^4E. \quad (3.1)$$

From left to right, g is net gain, $1/\Omega$ is related to filter bandwidth, D is GVD parameter, α and δ are the cubic and quintic parameters respectively for amplitude modulation by a saturable absorber, and γ denotes the SPM.

It has been shown that the CQGLE has some analytic solutions for dissipative solitons with variable spectral and temporal shapes in an all-normal-dispersion fiber. Fig. 3.1 from Ref. [94] indicates some possible types of dissipative soliton solutions.

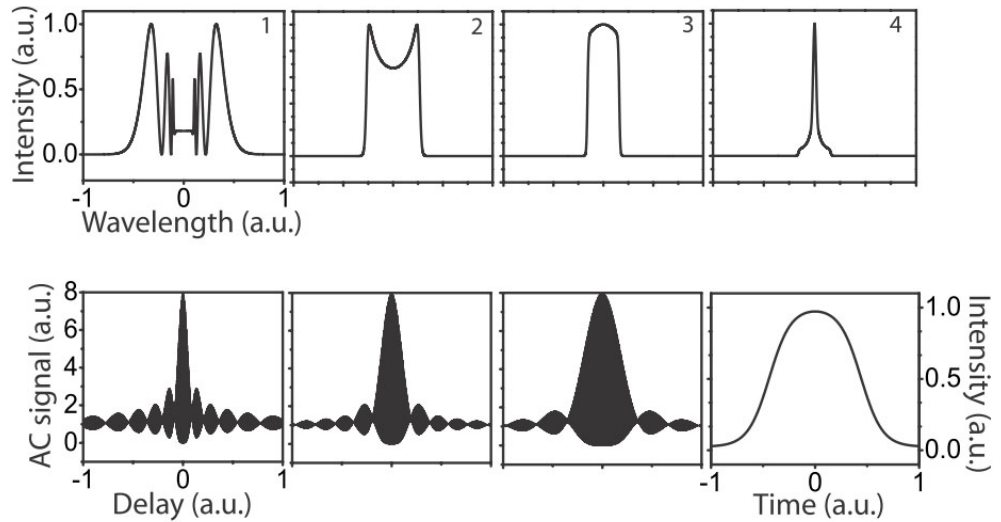


Figure 3.1: The theoretical solution of CQGLE with several possible different pulse shapes.

3.3.2 Nonlinear Schrödinger equation

The CQGLE can be considered an extended NLSE, where nonlinear amplitude modulations such as spectral filtering and saturable absorption are all incorporated. With an appropriate model shown in Chapter 2 describing these effects, we may

also use the NLSE method to simulate the dissipative soliton system with normal dispersion.

Starting from NLSE, we can use Eq. (2.1), (2.3) and (2.8) again to describe the fiber laser behavior:

$$\begin{aligned}\frac{\partial E}{\partial z} &= \frac{1}{2}(g - \alpha)E - \beta_1 \frac{\partial E}{\partial t} + \frac{1}{2}(\beta_2 - ib) \frac{\partial^2 E}{\partial t^2} + i\gamma|E|^2 E, \\ g &= \frac{g_0}{1 + \frac{\int_0^T |E|^2 dt}{E_{sat}}}, \\ \alpha_{SA} &= \frac{\alpha_0}{1 + \frac{|E|^2}{P_{SA}}},\end{aligned}$$

with a positive GVD value β_2 here.

These equations build a dynamic model suitable for split-step calculations in programming, for a mode-locked single fiber in the dissipative environment with normal dispersion. Every parameter in our dynamic NLSE model has an evident physical meaning, without the requirement of artificially taking a quintic amplitude term into account as in CQGLE. Also, our NLSE model provides more flexibility, so that we can easily attach a lumped 50:50 directional coupler to it (as in Chapter 2), connecting two channels into one array. In our model, only one lumped SESAM will be used in the array as the partial reflection to mode lock all channels, while CQGLE models the saturable absorption as distributed everywhere in each fiber. Similar to CQGLE, our dynamic NLSE model also includes the linear and nonlinear gain and losses, as well as linear and nonlinear phase modulations, which are necessary for generating dissipative solitons. Thus it is reasonable to build the model in this way to describe the behavior of dissipative solitons.

To verify our model and simulation coding, we first apply it on the single fiber structure in Fig. 2.10. Several typical shapes of dissipative solitons are produced in Fig. 3.2, using different fiber parameters within an active all-normal-dispersion

fiber. It qualitatively matches these typical solutions of CQGLE analytically and experimentally [94] and therefore confirms on the validity of our numerical simulation model.

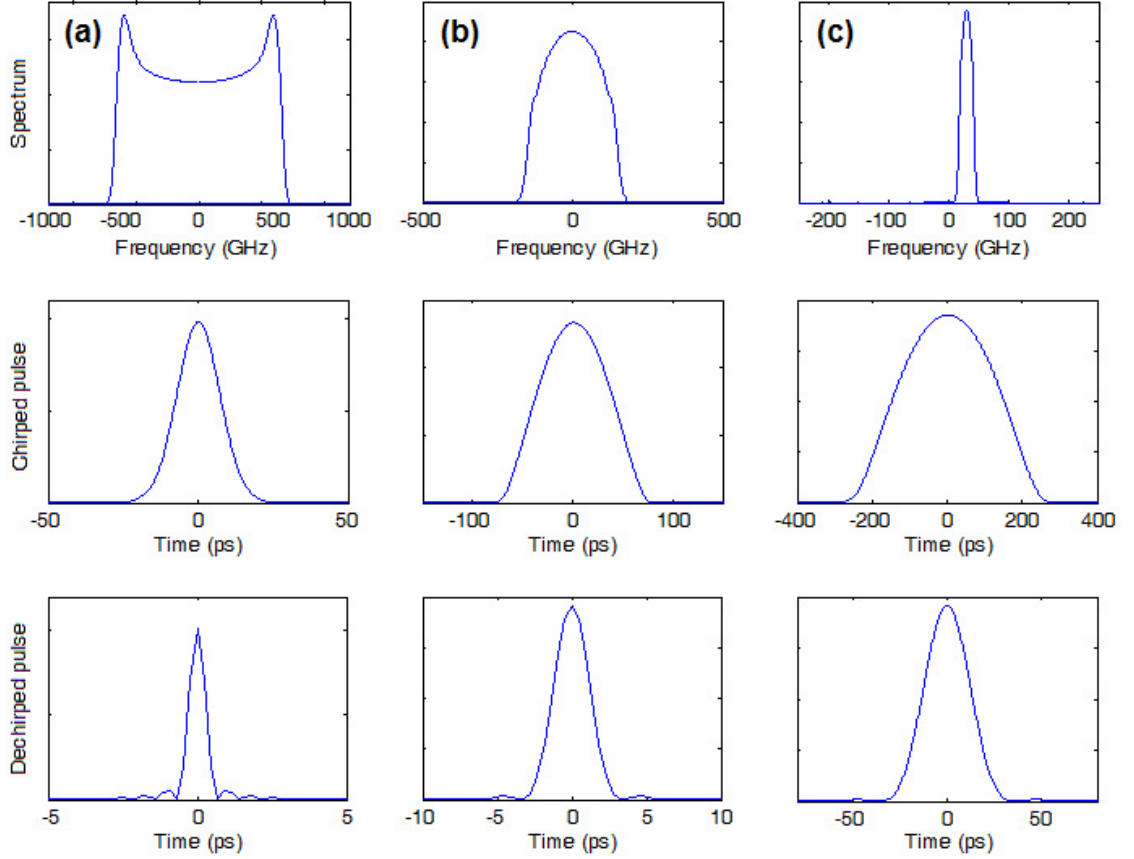


Figure 3.2: Some simulation results of our dynamic NLSE model. $\gamma = 0.005\text{m}^{-1}\text{W}^{-1}$ for (a) and $0.003\text{m}^{-1}\text{W}^{-1}$ for (b) and (c). $\beta_2 = 0.023\text{ps}^2/\text{m}$ for (a), $0.075\text{ps}^2/\text{m}$ for (b), $0.24\text{ps}^2/\text{m}$ for (c). $P_{SA} = 9.3\text{W}$ for (a) and (b), 0.93W for (c).

3.3.3 Simulation result for a single Yb-doped fiber laser

Here we present the simulation result for a single Yb-doped fiber laser cavity, operating at $1.060\mu\text{m}$ wavelength for normal dispersion. Fig. 3.3 shows the unidirectional cavity model with an active single mode all-normal-dispersion fiber (with a uniform and positive GVD parameter). A lumped fast saturable absorber is connected to the end of fiber, to provide the nonlinear loss for mode locking. 12% of the total output

power is fed back to finish the roundtrip in the ring cavity. The output pulse can be dechirped later to achieve high peak intensity.

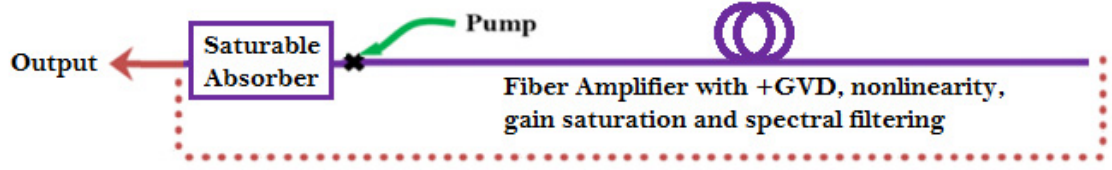


Figure 3.3: The structure of a ring cavity. A fiber amplifier is modeled with positive GVD, Kerr nonlinearity, gain saturation and spectral filtering. One end of the fiber connects to a lumped saturable absorber.

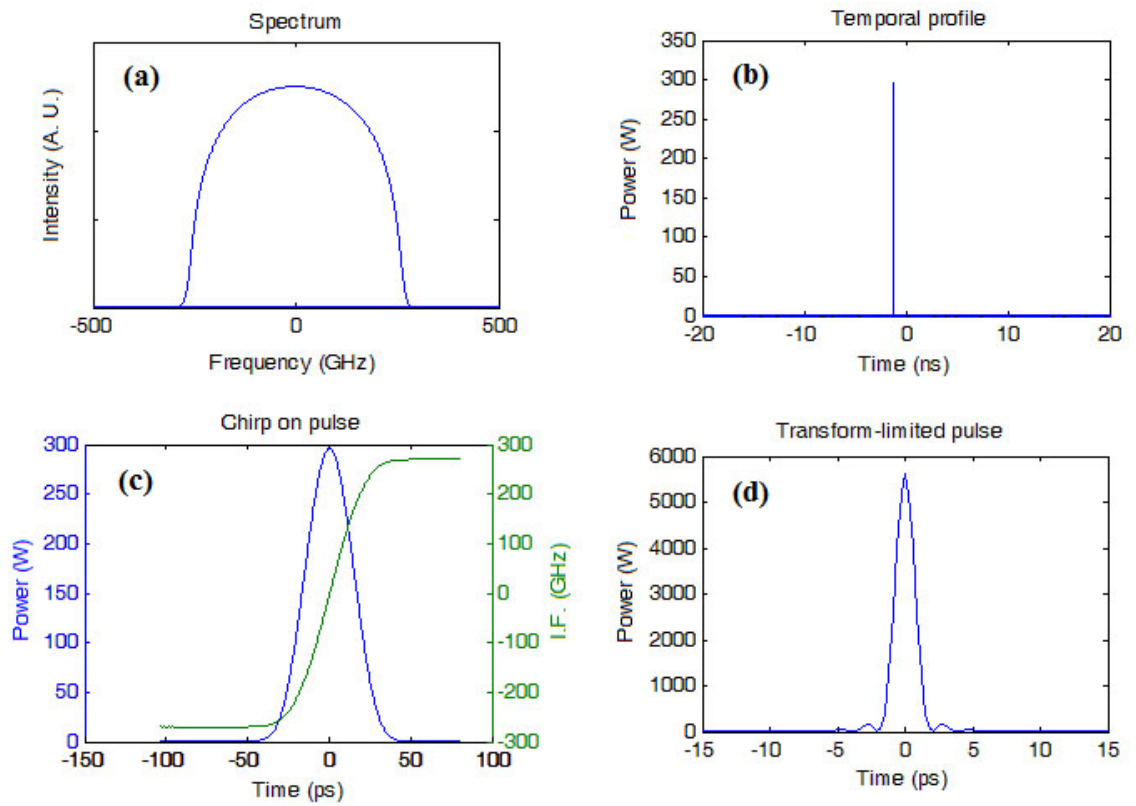


Figure 3.4: Simulation results for a single channel Yb-doped fiber. (a) The spectrum. (b) The pulse packet in the roundtrip time window. (c) The pulse profile with instantaneous frequency. (d) The transform-limited pulse.

Here the unsaturated gain g_0 is 1.76m^{-1} , the gain saturation energy E_{sat} is 7.2nJ , the nonlinearity γ is $0.003\text{W}^{-1}\text{m}^{-1}$, and the dispersion loss b is $0.13\text{ps}^2/\text{m}$ for spectral filtering. With a fiber length of 8.083m , we have simulation result shown in Fig. 3.4.

The pulse energy is 10.17 nJ and the average output power is 258.6 mW. The pulse is chirped with a FWHM about 30 ps.

3.4 Dissipative solitons in fiber laser arrays

In mode locking operation where short pulses are generated, we are able to scale up the energy carried by the pulse packet with coherent beam combining. Instead of a single pulse per roundtrip, a pulse packet with a tunable high repetition rate is produced, as a result of the spectral beating between different cavity lengths in the array [62, 64]. The pulse interval is theoretically determined by $\Delta T = n\Delta L/c$ as a unidirectional ring cavity, where n is the refractive index and ΔL is the fiber length difference between two channels. Accordingly, the spectrum is no longer continuous, but only exists near the common longitudinal modes for both channels. Therefore the separation between two adjacent array modes is given by $\Delta f = 1/\Delta T = c/(n\Delta L)$, which is also the temporal pulse repetition rate. It is tunable because we can easily control ΔL to adjust it.

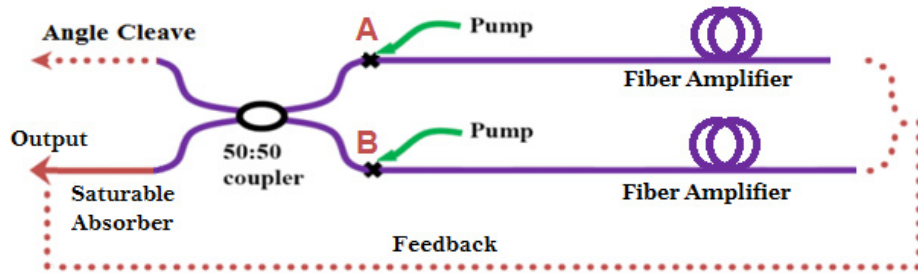


Figure 3.5: The Mach-Zehnder interferometer structure for mode locking of two coupled fiber lasers. There is an angle cleave at one port while a saturable absorber is connected to the other output port to provide feedback and a mode locking mechanism.

A unidirectional Mach-Zehnder interferometer structure as shown in Fig. 3.5 is used. A 50:50 directional coupler connects two Yb-doped fibers, with one arm connected with an angle cleave and the other arm feedback to the fibers after a saturable absorber. Both channels are identical in their pumped power, GVD, nonlinearity, gain

saturation power and loss dispersion parameter, but with slightly different lengths: 8.083m and 8.003m. We keep other cavity parameters the same as in our simulation result for one single channel in the Section 3.3.

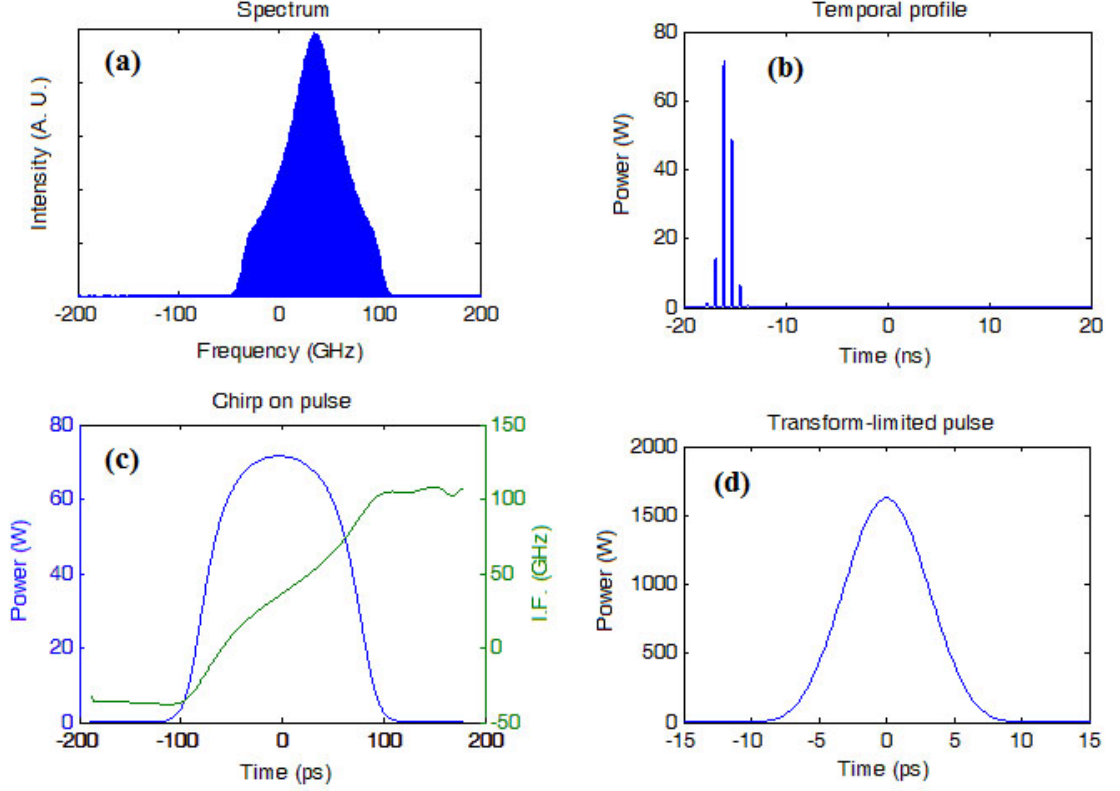


Figure 3.6: Simulation results for a two-channel fiber laser array with $\gamma = 0.003\text{m}^{-1}\text{W}^{-1}$ and $\beta_2 = 0.023\text{ps}^2/\text{m}$. (a) The spectrum. (b) The pulse packet in the roundtrip time window. (c) The pulse profile with instantaneous frequency. (d) The transform-limited pulse.

From the simulation results in Fig. 3.6, the average output power is 536.5 mW. Since there is a pulse packet with more than one pulse as a consequence of spectral beating, we select the pulse with highest energy, which is 12.71 nJ. The combining efficiency is 79.72%, defined as the ratio of the output power through the SESAM port to the total power from both the SESAM and the angle cleave port. The remaining power leaks from the laser cavity through the port with angle cleave. The pulse is chirped and elongated to 140ps FWHM, as a result of the interplay of normal dispersion and nonlinearity.

3.4.1 Comparisons between positive and negative GVD

To demonstrate the difference between positive and negative GVDs, a control group is provided in Table 3.4.1 and Fig. 3.7 with $-0.003\text{ps}^2/\text{m}$ GVD for Er-doped fibers at the wavelength of $1.545\mu\text{m}$. The result found in anomalous dispersion has a much broader bandwidth, much shorter pulse duration, and also closer to the transform-limit. It is well known that the pulses in anomalous dispersion are vulnerable to wave-breaking at high peak intensity as a result of nonlinear effects. By contrast, the chirped pulses in normal dispersion are more robust with a lower peak intensity and a higher pulse energy. By removing the chirp, the pulses can be compressed for higher peak power. Therefore, to contain more power per pulse without wave-breaking, normal dispersion is preferred to the anomalous dispersion.

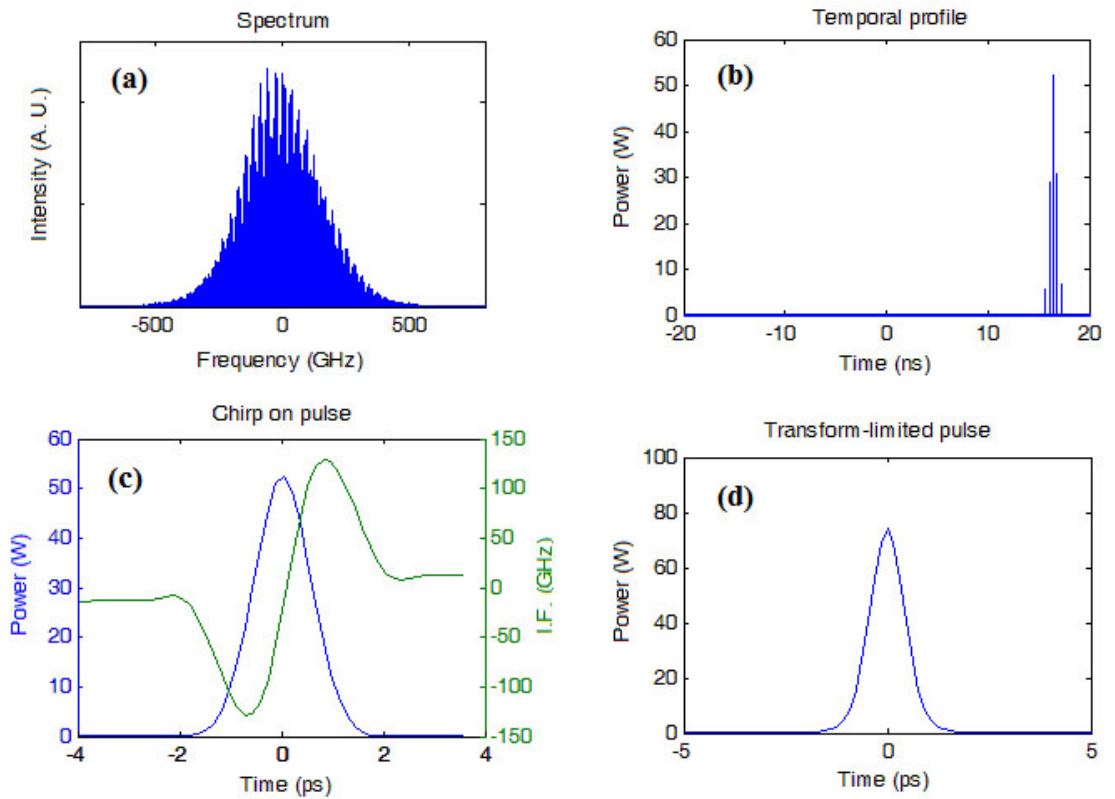


Figure 3.7: Simulation results from a two-channel Er-doped fiber laser cavity in anomalous dispersion. (a) The spectrum. (b) The pulse packet in the roundtrip time window. (c) The pulse profile with instantaneous frequency. (d) The transform-limited pulse.

Table 3.1: Comparison between Yb-doped and Er-doped fiber laser arrays, with positive and negative GVD parameters respectively.

β_2 (ps ² /m)	0.023	-0.003
Output power (mW)	536.5	17.27
Max pulse energy (nJ)	12.71	0.086
Combining efficiency (%)	79.72	85.66
Chirped pulse FWHM (ps)	140	1.5

Comparing the results for positive and negative GVD (Fig. 3.6 and Fig. 3.7), we find that with coherent beam combining, the dissipative solitons in normal dispersion two-channel Yb-doped array can carry about two orders higher energy than the Er-doped array.

3.4.2 Effects of nonlinearity

To investigate the impact of nonlinearity, Fig. 3.8, Fig. 3.9 and Table 3.4.2 give a comparison with two other γ values: 0.0015 and 0.0045m⁻¹W⁻¹, in addition to $\gamma = 0.003\text{m}^{-1}\text{W}^{-1}$ in Fig. 3.6. A typical γ value for fibers is at the order of 0.001m⁻¹W⁻¹, which can be increased by reducing the fiber's effective cross section area A_{eff} . The combining efficiency drops slightly with the increase of nonlinearity, but still remains above 78%. Accordingly, the time-average output power drops together with the combining efficiency. The positive GVD and the SPM from nonlinearity both increase the chirp. As a result, higher nonlinearity brings a broad spectral bandwidth and elongates the temporal duration.

Therefore, we have built a mode-locked beam combining system in the normal dispersion regime. A good combining efficiency gives the system a higher power output than a single-channel fiber laser, and the stable dissipative solitons give it higher pulse energy than anomalous dispersion, and make it more robust. This approach provides the possibility of achieving a higher pulse energy and dechirped peak power,

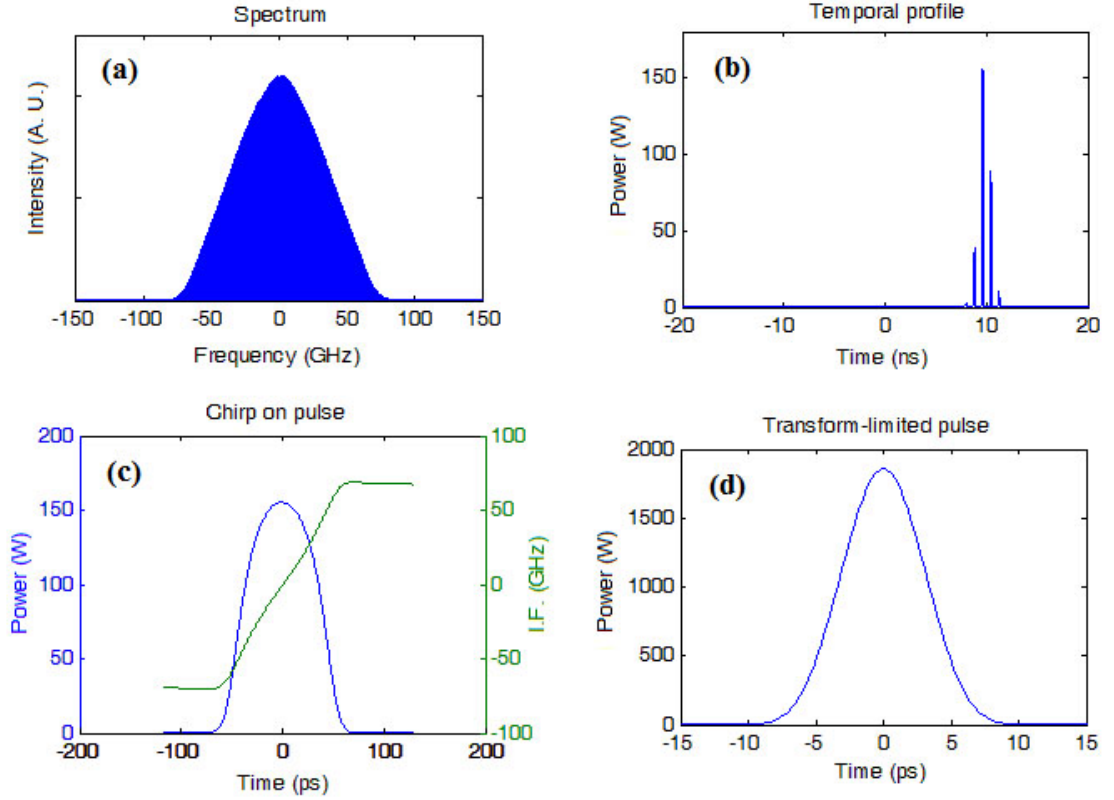


Figure 3.8: Simulation results for $\gamma = 0.0015\text{m}^{-1}\text{W}^{-1}$. (a) The spectrum. (b) The pulse packet in the roundtrip time window. (c) The pulse profile with instantaneous frequency. (d) The transform-limited pulse.

Table 3.2: Comparison among different nonlinearity parameters.

γ ($\text{m}^{-1}\text{W}^{-1}$)	0.0015	0.003	0.0045
Output power (mW)	608.4	536.5	516.4
Max pulse energy (nJ)	14.44	12.71	12.36
Combining efficiency (%)	84.18	79.72	78.49
Chirped pulse FWHM (ps)	80	140	200

due to two factors: scaling up the total output energy of the pulse packet by beam combining, and increasing the energy carried by every pulse by dissipative solitons in normal dispersion.

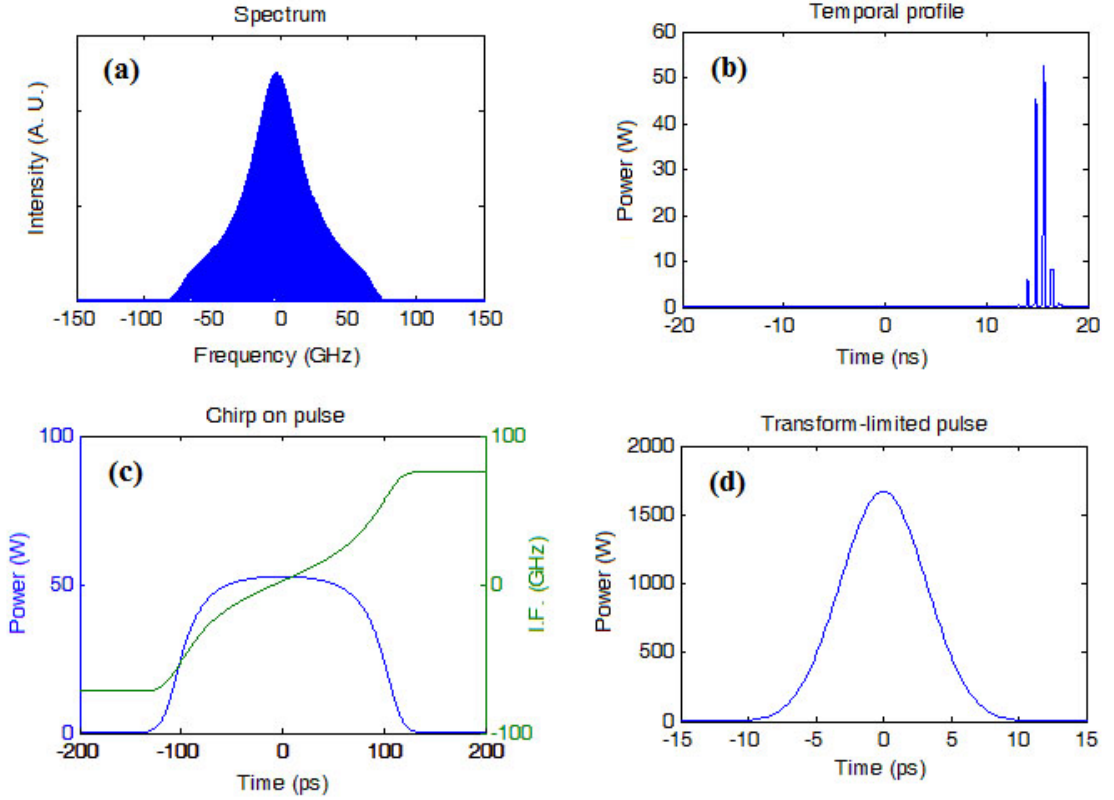


Figure 3.9: Simulation results for $\gamma = 0.0045\text{m}^{-1}\text{W}^{-1}$. (a) The spectrum. (b) The pulse packet in the roundtrip time window. (c) The pulse profile with instantaneous frequency. (d) The transform-limited pulse.

3.5 Pulse train operation

A mode-locked pulse train with high power and GHz level pulse repetition rate is attractive in a great number of applications such as optical clocking, high-speed optical sampling, telecommunication, ultrafast spectroscopy, and precision metrology. In fiber lasers, however, there is much difficulty in getting such a high pulse repetition rate because of the cavity length limit. Therefore, some techniques including harmonic mode locking are used for pulse train generation. We found that the high pulse repetition is an intrinsic property as a consequence of the spectral beating in a coherent beam combined fiber laser cavity. Hence it becomes meaningful to use coherent combining to produce a stable and robust pulse train with high power and a high repetition rate.

3.5.1 Pulse repetition rate

In conventional mode locking operation, one pulse is generated per roundtrip, and it repeats every roundtrip so that the pulse interval is exactly the roundtrip time, which is proportional to the cavity length. Hence the pulse repetition rate is inversely proportional to roundtrip time and cavity length. In order to get a high repetition rate, one may first consider making the length of laser cavity as short as possible. While this simple method may work for solid-state lasers in free space, it is not that easy for fiber lasers because the gain parameter is not high enough for doped silicon fibers. A too short cavity length may not provide enough gain for the lasing threshold. Besides the active fiber section, other devices such as WDM, polarization controllers, directional couplers, and optical isolators/circulators may extend the length of cavity even longer. A bidirectional cavity has doubled the roundtrip time from a ring cavity with the same fiber length, further lowering down the pulse repetition rate. Generally, it is not very easy to produce a fiber laser cavity shorter than 1m, which is almost a limit for this basic approach.

A useful solution to increase the repetition rate for originally passively mode-locked pulses is to multiply the number of pulses circulating in the cavity, and simultaneously make them uniformly distributed as shown in Fig. 3.10(a). It is named as harmonic mode-locking and was first observed in 1993 from an erbium-doped laser by Grudinin et al. [53] The principle of harmonically mode-locked fiber lasers is to split one single pulse circulating in the cavity into several pulses in the presence of high pumping power. However, for passively mode-locked lasers, it becomes a challenge to ensure constant pulse spacing, since pulses are usually randomly located in the cavity. So the key part of harmonic mode locking is to make these pulses self-arranged to a stable and well-organized pulse train, with a repetition rate as a multiple of the longitudinal mode separation. Furthermore, the pulses are not always mutually phase coherent [3]. Driving the modulator of an actively mode-locked laser with a harmonic

of the resonator's round-trip frequency can lead to equidistant multiple pulses. In this approach, we need an additional active control on amplitude and phase modulation of the intracavity field, involving more complex hardware. Such harmonically mode-locked system costs more since it is more complicated and larger in size.

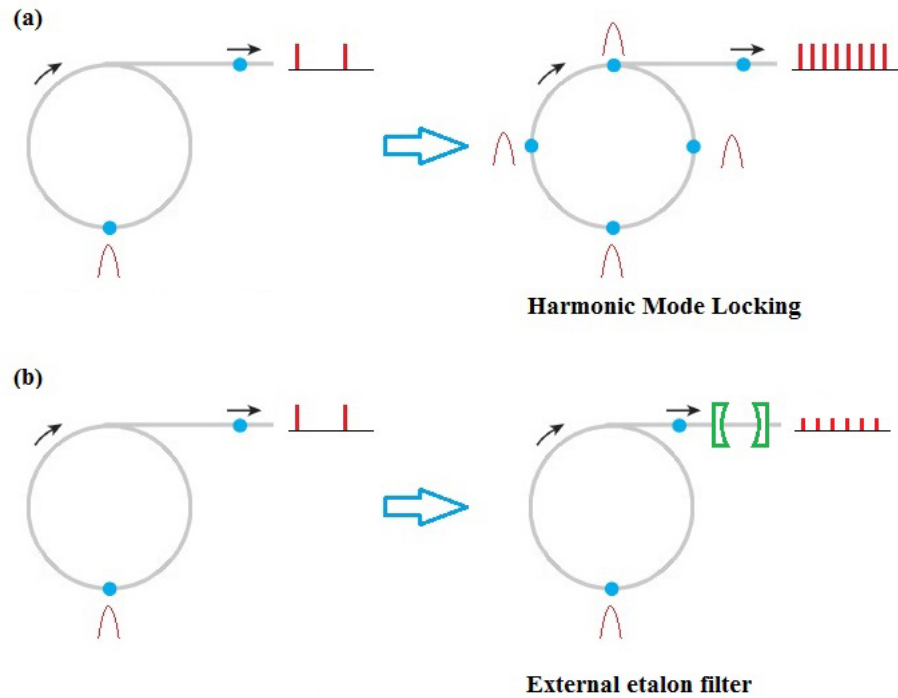


Figure 3.10: Increase the pulse repetition rate. (a) Harmonic mode locking multiplies the number of pulses circulating in the cavity. (b) An external etalon is used for spectral elimination.

Another strategy is to multiply the repetition rate externally with Fabry-Pérot filters by spectral elimination as in Fig. 3.10(b) [56, 57]. After exiting the laser, each pulse enters an external Fabry-Pérot cavity with a much shorter cavity length. It bounces back and forth in the external cavity and a series of pulses are hence generated. For one thing, high finesse etalon filters are relatively lossy elements; for another, this spectral elimination approach can maintain the phase coherence between the multiplied laser pulses. It works at a cost of loss of laser power. Moreover, such external cavity is more sensitive to the frequency drift. To better understand the term of “spectral elimination”, the concept of frequency comb need be introduced

first.

3.5.2 Frequency Comb

To explain the physics behind a pulse train, we need to transform the temporal train into frequency domain. If the pulses are mutually coherent in a regular pulse train, the optical spectrum of the pulse train is a frequency comb after Fourier's transform, where the spacing of the lines is just the pulse repetition rate. If the pulse train is infinitely long, its Fourier spectrum consists of infinitely narrow lines. As an optical spectrum with equidistant lines, a frequency comb has many applications such as an optical clock [114, 115].

Figure 3.11 shows the temporal and spectral profiles of a pulse train. The periodicity of an infinitely long pulse train is represented by a series of Dirac delta functions. After a convolution with the pulse shape envelope, we get the temporal profile for the train. At the same time, every term can be Fourier transformed to get their spectral correspondence. The Fourier transform of an infinitely long train of Dirac delta function is also an infinite train of Dirac delta function, which has a name of frequency comb. Also, the convolution operation corresponds to multiplication after Fourier transform. The product of a single pulse's spectral envelope and a frequency comb gives the spectral profile of the pulse train. The discrete spectrum in a frequency comb corresponds to the temporal periodicity. It is seen that the distance between two adjacent teeth in a frequency comb is exactly the pulse repetition rate [58, 116, 117].

For spectral elimination, the external etalon cavity forms a frequency comb determined by its own length. Its design motivation is to make the repetition rate, i.e. the teeth separation in the frequency comb, much higher than the longitudinal mode separation. Therefore, in the spectrum, a frequency comb with high line separation reduces the density of modes and eliminates most modes between adjacent teeth of

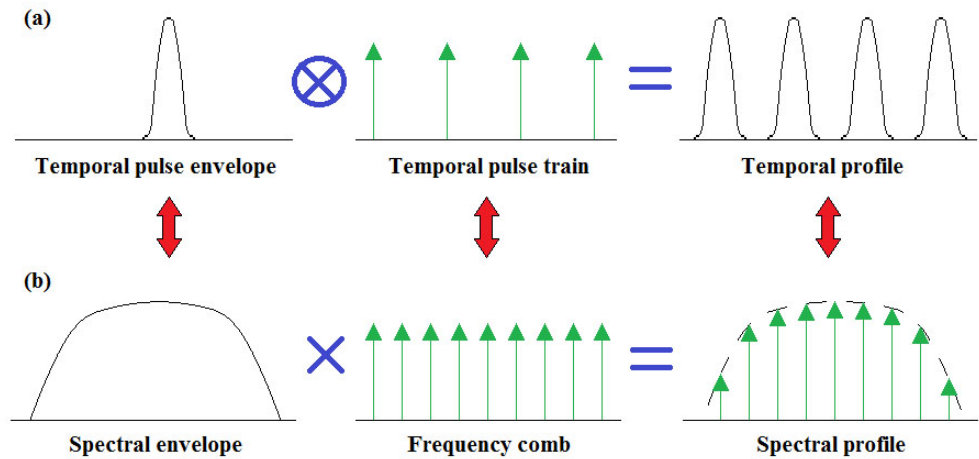


Figure 3.11: Illustration of an infinitely long pulse train profile in temporal and spectral domains. (a) In time domain, it is a convolution of a single pulse shape envelope and an infinitely long pulse train with Dirac delta functions. (b) In frequency domain, it is the product of the spectral envelope of a single pulse and an infinitely long frequency comb, as a Fourier transform from (a). Red arrows denote Fourier transform.

the comb.

Now let us return to the array modes with coherent beam combining in Chapter 2. Determined by the channel length difference ΔL , the separation of array modes, i.e. the repetition rate, can be much higher than the longitudinal modes separation. That is to say, similar to an external Fabry-Pérot filter, the array modes also perform as an effective frequency comb to the mode locking system. It explains why the pulse packet has a high repetition rate among its pulses, no matter what the sign of GVD is.

3.5.3 A new approach to a robust pulse train with high repetition rate

Besides the advantages as dissipative solitons, a pulse packet is very useful in clocking applications especially once it becomes a continuous pulse train, i.e. the pulse packet is of the same length as the roundtrip time so that the pulse packet in each roundtrip gets connected as a long train. Also, the pulses inside packet are required with a uniform interval. Such a high pulse repetition rate is highly valuable in

many applications. As shown in last section, more than one pulse per roundtrip is the key technique for increasing the repetition rate, as the roundtrip time cannot be too short for a fiber laser system. The array beating effect from coherent beam combining performs as a natural approach for this goal, together with all advantages of passive elements such as low cost and simplicity. However, the pulse packet durations in our previous results are not long enough. Since the pulse separation between any two adjacent pulses is determined by $\Delta T = n\Delta L/c$, we can increase ΔL a little to raise the pulse separation, and hence elongate the pulse packet.

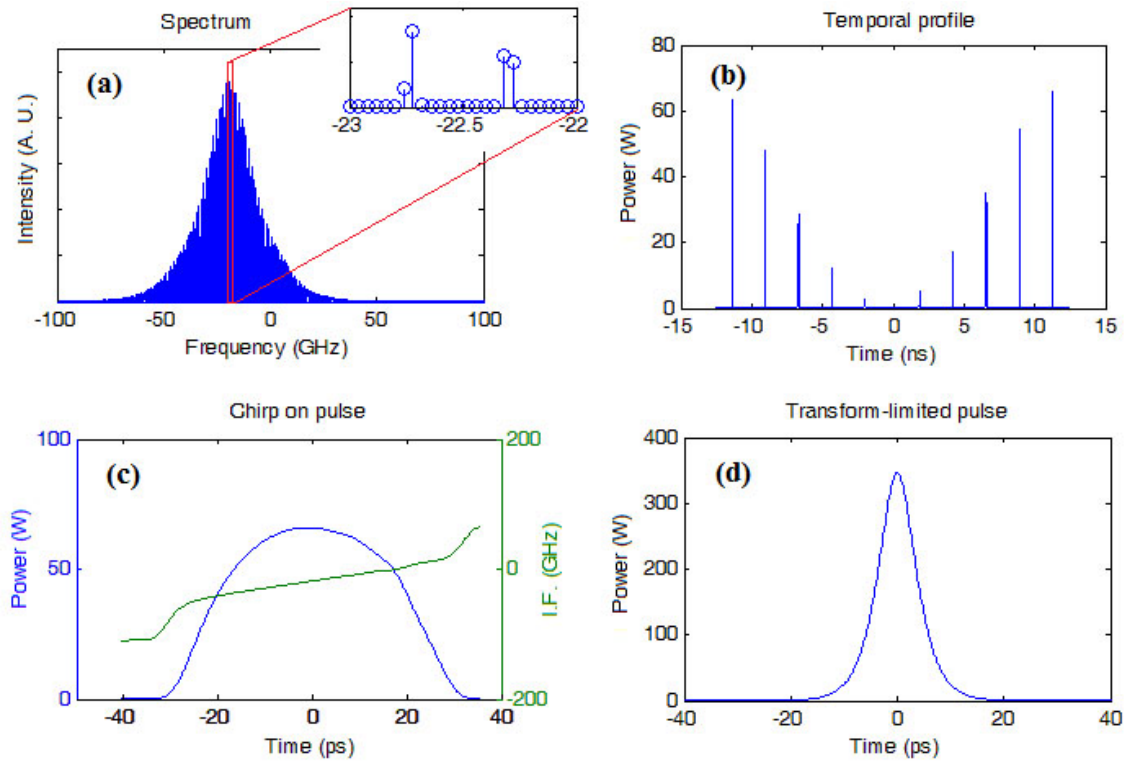


Figure 3.12: Pulse train results from two-channel beam combining for fiber lengths 4.53m and 5.00m. (a) The spectrum and its zoom. Each circle denotes a longitudinal mode. (b) The temporal profile in a full roundtrip time. (c) The chirped output pulse. (d) The compressed pulse.

Here we chose the lengths of two channels as 4.53m and 5.00m respectively. The GVD and nonlinearity are $0.023\text{ps}^2/\text{m}$ and $0.003\text{m}^{-1}\text{W}^{-1}$ as usual. The simulation result is shown in Fig. 3.12. There is a long pulse packet covering almost the whole roundtrip time in its temporal profile. Furthermore, it is repeated every round trip,

making it similar to a pulse train modulated by a relatively slow envelope. So there are simultaneously two repetition rates here: one is the intrinsic high repetition rate of pulses, and the other is the relatively low repetition rate of pulse packets. The separation between pulses is $\Delta T = n\Delta L/c$, and the modulation envelope period approximately equals round trip time.

We now consider a special commensurate case where the fiber lengths are exactly integer times of their length difference ΔL , such as 4.50m and 5.00m, while keeping everything else unchanged. An interesting result of an ideal pulse train with a high repetition rate is achieved in Fig. 3.13, with uniform pulse intensities and uniform pulse separations in the whole roundtrip time window. Here we have 10 identical pulses per roundtrip time, so the repetition rate has risen 10 times from a single-channel fiber laser with fundamental mode locking. Since the total energy is almost equally distributed among these pulses, the energy and peak power of each pulse are decreased from the incommensurate case.

In the view of Fourier transform, the packet temporal width is controlled by the width of the spectral spike, and an infinitely narrow spectral spike corresponds to an infinitely long pulse train in the temporal profile. For commensurate fiber lengths, the array modes are separated by $\Delta f = c/(n\Delta L)$, which is exactly a multiple of the longitudinal mode separation $c/(nL)$ for each channel. That is, all array modes can fall on longitudinal modes and become its proper subset. So each spectral spike contains only one mode frequency and is almost infinitely narrow. If it is incommensurate, however, not all array modes belong to the set of longitudinal modes. At the frequency where an array mode should exist accurately from beating effects, there are no longitudinal modes at that specific point. If so, the array mode will be substituted by its nearby longitudinal modes. Therefore the spike gets some width as shown in Fig. 3.12. That explains the difference between commensurate and incommensurate cases. There is no longer amplitude modulation for commensurate

fiber lengths.

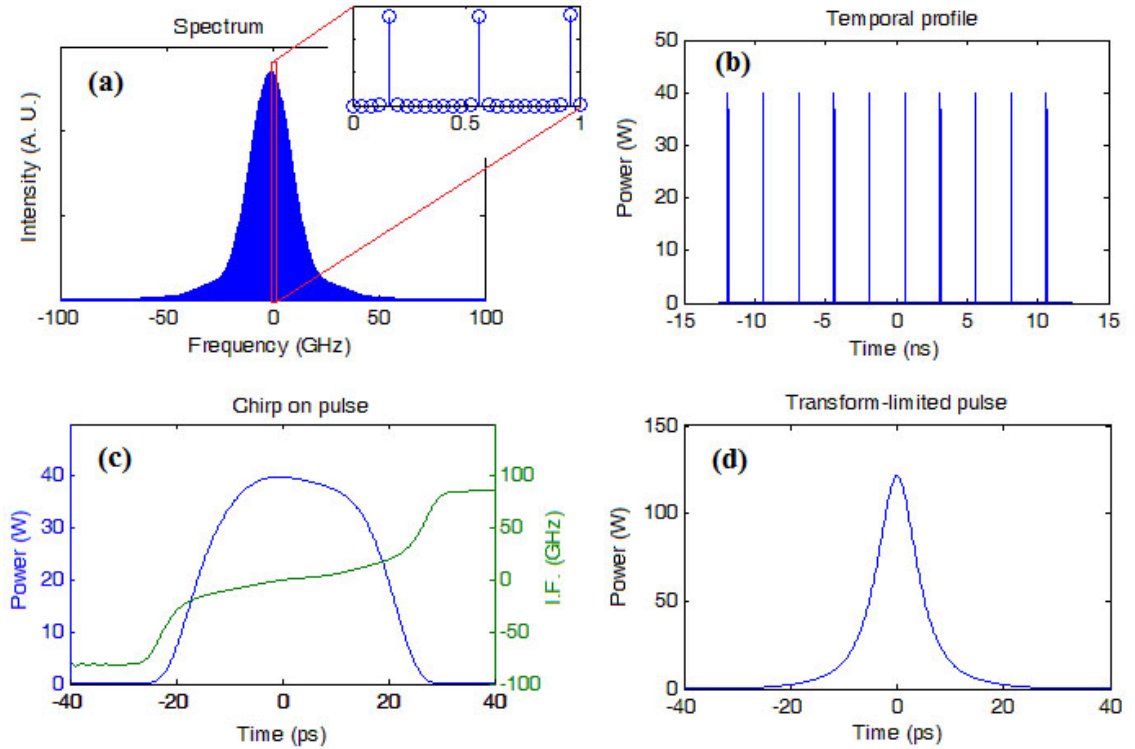


Figure 3.13: A comparison of Fig. 3.12 with commensurate lengths 4.50m and 5.00m (They are integer times of the difference 0.50m).

3.5.4 Discussion on the results

Comparing with the lossy external Fabry-Pérot filter, the directional coupler is basically lossless. The laser power does not get reduced, but combined from an array with two or more channels. Therefore we may develop a new approach to a robust pulse train with high repetition rate from coherent beam combining, with advantage compared to conventional methods.

In the real world with laser noises, however, the pulse train may not be completely stable and infinitely long. We now consider a pulse train with finite time duration. Figure 3.14 shows a finite and amplitude modulated pulse train, in contrast of Fig. 3.11. After a Fourier transform, the frequency comb no longer consists of Dirac delta functions, but with some spectral spikes of finite width. This can be understood

physically: generally speaking, the array modes of the array are not necessarily the longitudinal modes of each channel. Hence the longitudinal modes which are the closest to that frequency points (from right and left sides) are used to substitute the array mode.

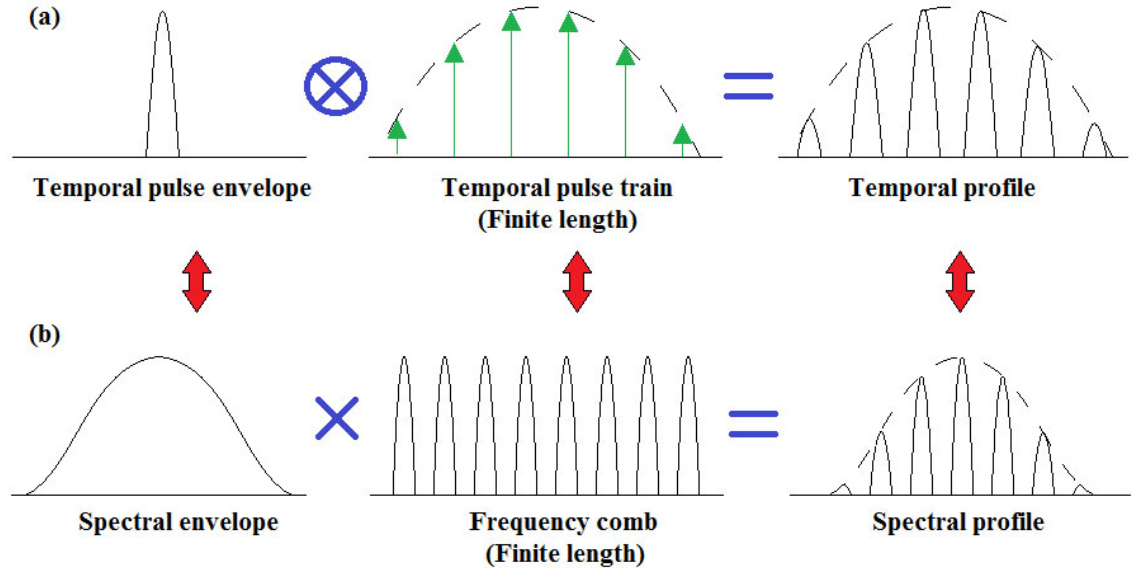


Figure 3.14: Illustration of a finite pulse train profile in temporal and spectral domains. (a) In time domain, it is a convolution of a single pulse shape envelope and a finite (also amplitude modulated) pulse train with Dirac delta functions. (b) In frequency domain, it is the product of the spectral envelope of a single pulse and a finite long frequency comb, as a Fourier transform from (a). Red arrows denote Fourier transform.

In this case, each comb tooth is no longer infinitely narrow on one frequency point, but has a finite width of a few array mode separations. Such a finite spectral width corresponds to a temporal pulse train with finite length. Consequently, we got the temporal and spectral profiles as shown in Fig. 3.14. Both of them are of finite lengths and finite spike widths.

We may understand Fig. 3.11 as a particular commensurate case, where all array modes belong to the set of longitudinal modes of each fiber channel. Fig. 3.14 is a more general case. One analogy to them is the external Fabry-Pérot cavity. Unless the length of the Fabry-Pérot cavity is accurately controlled so that the laser

cavity's optical length is an integer multiple of it, there would be pulse amplitude fluctuations just as our incommensurate results above. So we may consider coherent beam combining as lossless spectral elimination, which forms a frequency comb with array modes and reduces the mode density on the spectrum. The longitudinal modes between two adjacent comb teeth are eliminated in the laser cavity. For the same reason, it becomes challenging to scale up the number of channels in mode-locked operations unless each channel length is accurately controlled to be commensurate as in Section 2.6.

3.6 Conclusion

In this Chapter, we have carried out simulations of the dissipative solitons in simultaneous passive coherent beam combining and mode locking where the cavity is of all normal dispersion, with a dynamic model based on the NLSE. With balances on both amplitude and phase modulations, dissipative solitons in an all-normal-dispersion fiber are more stable and robust to wave-breaking than in an anomalous dispersion cavity. With coherent beam combining, a stable pulse packet of dissipative solitons with a high repetition rate is produced every roundtrip. We are able to scale up pulse energy and pulse packet energy carried by chirped dissipative solitons, while avoiding wave-breaking.

We have shown that a stable pulse train can be generated in a passively coherently beam combined fiber laser array. The pulse packets have a modulation repetition rate comparable with the roundtrip time, while the pulses have a much faster repetition rate inside the pulse packet. Commensurate fiber lengths degenerate the pulse packet modulation, and a regular pulse train with uniform pulse intensities and a high repetition rate is achieved. The physical explanations for such phenomenon have also been presented related to the frequency comb. Simulation results have validated our theoretical analysis.

CHAPTER IV

Tunneling in Directional Couplers [138]

4.1 Introduction

Our beam combining model relies on directional couplers. As a typical four-port device as shown in Fig. 2.1, a directional coupler is connected to two discrete fiber channels at one side, and to a partial reflector and an angle cleave at the other side. It plays a key role in our passive coherent beam combining model, as the intra-cavity connector between the fiber amplifiers and output/feedback signals, and also the inter-cavity connector between two discrete channels. The 50:50 ratio guarantees that each channel contributes equally to the whole cavity. In addition, it minimizes the possible cavity losses leaked through the angle cleave port as analyzed in Section 2.6.3, to optimize the system in its best efficiency. Inside a directional coupler, two parallel fiber cores are placed together very close to each other, so that the power from each channel can exchange and redistribute. Therefore, it is interesting to explore the dynamic process how a directional coupler works, how the powers and phases are redistributed, and more importantly, how the mode-locked pulses tunnel inside it.

In this chapter, we will first take a brief review on the optical field transfer matrix from the view of mode power distribution and phase change, using the coupled-mode theory [118]. Next we will focus on the mechanism of the coupling process, the evanescent wave, which transfers energy between two fiber cores by means of frus-

trated total internal reflection (FTIR). The fiber cladding acts as a barrier to prevent the optical wave propagating inside. A small evanescent field penetrates the less dense cladding but carries no time-average power in the direction normal to the interface. When another fiber core is brought within a few wavelengths of the first interface, the evanescent wave can penetrate this second fiber core and excite a propagating wave that transports energy away from the interface. This phenomenon of FTIR is the electromagnetic analog of quantum tunneling, with the cladding gap between the cores serving as the potential barrier within which the propagation constant is imaginary [119]. In fact, the directionally-coupled waveguides are referred to as tunnel-coupled waveguides in the Russian literature [120–124]. Because of the near-exact analogy between FTIR and quantum tunneling, there has been much interest in defining, calculating, measuring, and interpreting the time delay in FTIR as it would shed light on the dynamics of the quantum tunneling process, which latter process is difficult to probe directly [125]. Recently tunneling an optical potential well has been imaged directly by Tomes et al. [126].

Similar to 1-D electromagnetic/optical tunneling with undersized waveguides or periodic dielectric band gap structures, FTIR tunneling transports the wave longitudinally across the barrier. The difference is that FTIR tunneling is a 2-D problem where the incident beam suffers a lateral Goos-Hänchen shift at the same time [127]. (To clarify, in this chapter we use “longitudinal” or “normal” to denote the direction across the barrier and “lateral” or “transverse” for the direction in parallel with the fibers, in order to focus on the FTIR tunneling from one fiber to another.) Here we analytically calculate and interpret Goos-Hänchen shift with clear physical meaning.

Interestingly, an optical pulse may appear “superluminal” in optical tunneling, including FTIR tunneling inside a directional coupler [128–138]. That is, the group delay time between a pulse’s peak entering and exiting the barrier appears shorter than the propagation time required at a speed of c . Furthermore, it saturates with

the increase of the barrier width (Hartman effect) [139–141]. In this chapter we will make a thorough study on 2-D FTIR tunneling.

In the laser cavity, a directional coupler has much shorter length (a few centimeters) than the active fibers, so we neglect the influence of nonlinearity and dispersion in the tunneling analysis of this chapter. For single-mode fibers, we assume the incident angles are almost uniform for the FTIR incident beam. The distance between two fiber cores, i.e. the barrier width, is within a few wavelengths for a high coupling parameter. Consider a mode-locked pulse of 1ps. In a medium with refractive index $n=1.5$, its spatial length in the fiber is about $200\mu\text{m}$, which is hundreds of wavelengths. Since the pulse here is relatively long compared to the barrier width, the tunneling delay time is much shorter than the temporal pulse duration. So it is very reasonable to approximate the tunneling process as “quasi-static” [142–144]. A relatively long pulse corresponds to a relatively narrow spectral bandwidth. To further simplify, we consider a 2-D dielectric waveguide model rather than the actual cylindrical fibers, while the main physics and conclusions are not affected. Using a 2-D linear and non-dispersive model, we show that the group delay for FTIR is equal to the “dwell time” plus a “self-interference delay”, that is, the lifetime of stored energy in the gap between the fiber cores and in the partial standing wave in front of the gap. As in other manifestations of tunneling the saturation of group delay with barrier length (Hartman effect) is explained by the saturation of stored energy in the region defined. No superluminal propagation is implied.

4.2 Power distribution in directional couplers

It is total internal reflection (TIR) that confines the light propagating inside a fiber core. From the view of ray optics, the oblique incident beam reaches the cladding from fiber core, and then gets total-internally reflected if the incident angle exceeds the critical angle. As the light enters cladding, it becomes evanescent surface wave

and decays exponentially with the penetration distance into the cladding. Inside an optical directional coupler, two fiber cores are put together in parallel as shown in Fig. 4.1. The distance is so close that the surface wave has not vanished in the cladding between two fiber cores. In other words, the barrier is not thick enough to isolate optical waves. As a consequence, the TIR is frustrated and the light tunnels through the cladding barrier to the other fiber.

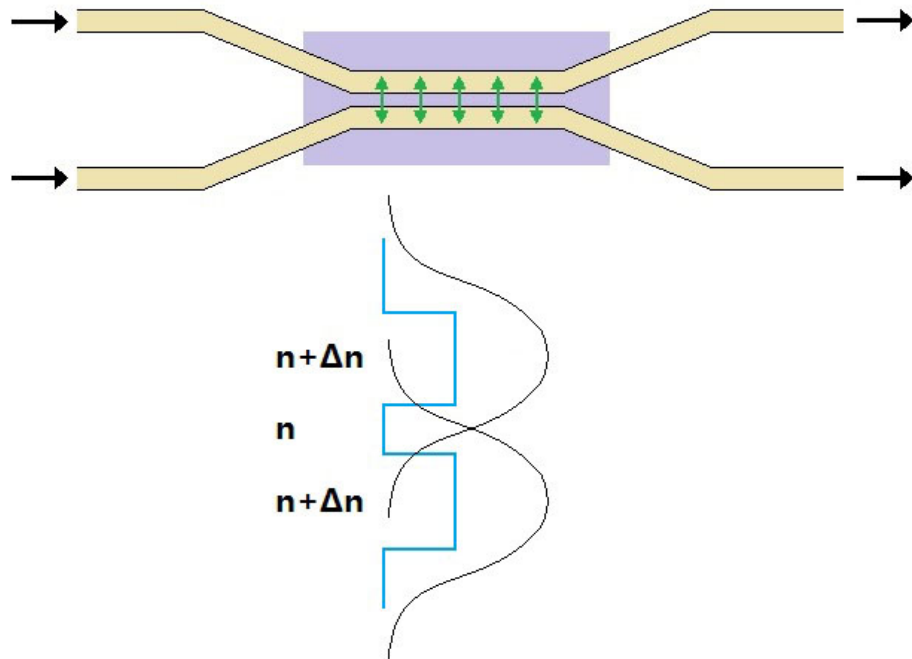


Figure 4.1: Upper: the structure of a directional coupler where two fiber cores with higher refractive indices are very close and parallel to each other. Lower: the single transverse mode in each fiber core tunnels to and gets coupled into the other core.

First we consider the coupling process in its steady state as power flow's redistribution by the perturbation on two co-directional propagating modes in two fiber cores respectively. Coupled-mode theory [118] is a powerful analytical model to analyze the power distribution in directional fiber couplers. It considers the change of refractive indices between core and cladding as shown in Fig. 4.1 as a weak perturbation $n(x) = n + \Delta n(x)$. The optical field from each single-mode fiber core extends to the

other one, and therefore the modes from two cores can get coupled as they propagate along the waveguide [145, 146]. Figure 4.1 gives an example for the coupling between two modes from two close fiber cores, which is common for a directional fiber coupler.

With a weak perturbation on indices, we use slow-varying envelope assumption to neglect higher order terms. The coupling among multiple fibers can be described by coupled-mode equations [118]:

$$\pm \frac{dA_\nu}{dz} = \sum_{\mu} iC_{\nu\mu} A_\mu \exp[i(\beta_\mu - \beta_\nu)z], \quad (4.1)$$

where A_ν is the wave amplitude for the ν th fiber, with a propagation constant of β_ν . This mode is coupled from the mode in another fiber with A_μ and β_μ by a complex coupling coefficient $C_{\nu\mu}$. The plus sign is taken if mode ν is forward propagating along \hat{z} , otherwise the minus sign is used. The coupling effects with all fibers are summed over index μ in Eq. (4.1).

In a directional coupler, two single-mode fibers get coupled with co-directional propagation \hat{z} , the coupled-mode equations reduce to a simpler form with analytical solutions:

$$\begin{aligned} \frac{dA_1}{dz} &= iC_{11}A_1 + iC_{12}A_2 \exp[i(\beta_2 - \beta_1)z], \\ \frac{dA_2}{dz} &= iC_{21}A_1 \exp[-i(\beta_2 - \beta_1)z] + iC_{22}A_2, \end{aligned} \quad (4.2)$$

where A_1 and A_2 are the mode amplitudes in each fiber with propagation constants β_1 and β_2 . With $j = 1, 2$ and $k = 1, 2$, C_{jk} is defined as $\frac{\omega\epsilon_0}{4} \int \Phi_j^* \Delta n_j^2 \Phi_k dx dy$, where Φ_j and Φ_k are normalized intensities for modes j and k . For $j \neq k$, C_{jk} provides the amplitude exchanging between two fibers. On the other hand, C_{jj} 's physical meaning is the tiny change on the propagation constant of each mode itself.

To separate C_{jj} and C_{jk} terms, we expand Eq. (4.2):

$$\begin{aligned}
A_1 &= \tilde{A}_1 \exp(iC_{11}z), \\
A_2 &= \tilde{A}_2 \exp(iC_{22}z), \\
\frac{d\tilde{A}_1}{dz} &= iC_{12}\tilde{A}_2 \exp[i2\Delta\beta z], \\
\frac{d\tilde{A}_2}{dz} &= iC_{21}\tilde{A}_1 \exp[-i2\Delta\beta z],
\end{aligned} \tag{4.3}$$

where $2\Delta\beta = \beta_2 + C_{22} - \beta_1 - C_{11}$ stands for the possible phase mismatch.

By solving the coupled-mode equations Eq. (4.3) with boundary conditions $A_1(0) = A_{10}$ and $B_1(0) = B_{10}$ at position $z = 0$, we can decouple A_1 and A_2 terms and derive a general analytical solution:

$$\begin{aligned}
A_1(z) &= A_{10}e^{-i\Delta\beta z} \left[\cos \left(z\sqrt{\Delta\beta^2 + C_{12}C_{21}} + i\Delta\beta \frac{\sin \left(z\sqrt{\Delta\beta^2 + C_{12}C_{21}} \right)}{\sqrt{\Delta\beta^2 + C_{12}C_{21}}} \right) \right] \\
&\quad + iA_{20}e^{-i\Delta\beta z} C_{12} \frac{\sin \left(z\sqrt{\Delta\beta^2 + C_{12}C_{21}} \right)}{\sqrt{\Delta\beta^2 + C_{12}C_{21}}}, \\
A_2(z) &= A_{20}e^{i\Delta\beta z} \left[\cos \left(z\sqrt{\Delta\beta^2 + C_{12}C_{21}} - i\Delta\beta \frac{\sin \left(z\sqrt{\Delta\beta^2 + C_{12}C_{21}} \right)}{\sqrt{\Delta\beta^2 + C_{12}C_{21}}} \right) \right] \\
&\quad + iA_{10}e^{i\Delta\beta z} C_{21} \frac{\sin \left(z\sqrt{\Delta\beta^2 + C_{12}C_{21}} \right)}{\sqrt{\Delta\beta^2 + C_{12}C_{21}}}.
\end{aligned} \tag{4.4}$$

Assume a good phase matching $2\Delta\beta = 0$, and if the two fibers are identical that $C_{12} = C_{21} = C$ based on symmetry, we can further simplify the results to be:

$$\begin{aligned}
A_1(z) &= A_{10} \cos(Cz) - iA_{20} \sin(Cz), \\
A_2(z) &= -iA_{10} \sin(Cz) + A_{20} \cos(Cz).
\end{aligned} \tag{4.5}$$

It is clear that the power $|A_1(z)|^2 = |A_{10}|^2 \cos^2(Cz) + |A_{20}|^2 \sin^2(Cz)$ and $|A_2(z)|^2 =$

$|A_{20}|^2 \cos^2(Cz) + |A_{10}|^2 \sin^2(Cz)$. Thus the power conservation for lossless couplers is confirmed with $|A_1(z)|^2 + |A_2(z)|^2 = |A_{10}|^2 + |A_{20}|^2$. For an ideal 3dB directional coupler that distributes the energy equally (50:50) to each channel at the output end ($z = d$), it is required that $\cos^2(Cd) = \sin^2(Cd) = 1/2$, therefore the coupling length should be

$$d = \frac{\frac{m\pi}{2} + \frac{\pi}{4}}{C}, \quad (4.6)$$

where m is an arbitrary integer. Take $m = 0$ for an example, the wave amplitude transform matrix between the entrance $z = 0$ and exit $z = d$ of the directional coupler becomes

$$\begin{pmatrix} A_1(d) \\ A_2(d) \end{pmatrix} = \begin{pmatrix} 1/\sqrt{2} & -i/\sqrt{2} \\ -i/\sqrt{2} & 1/\sqrt{2} \end{pmatrix} \begin{pmatrix} A_{10} \\ A_{20} \end{pmatrix}, \quad (4.7)$$

which is exactly the same transform matrix we have used in Chapter 2 and 3.

Besides the power distribution between two fiber cores of a directional coupler and the steady state transfer matrix, we also need explore the physics of how the power gets transported across the FTIR barrier, which is a region where light is evanescent. In the following sections, we will build a rigorous electromagnetic model to analyze the wave behavior in both transverse and longitudinal directions when tunneling through an FTIR barrier. Both the spatial lateral displacement and the temporal group delay will be analytically solved and interpreted in physics.

4.3 Evanescent waves

There are two groups of electromagnetic/optical waves: propagating ones and evanescent ones. The first one is sinusoidal and in space and time, while the latter one is exponential decaying with distance. With the separation of transverse and longitudinal modes, a plane wave with $\exp(-i\omega t)$ time-harmonic term traveling in

x-direction can be written as:

$$E = \exp[i(\mathbf{k} \cdot \mathbf{r} - \omega t)] = \exp[i(\mathbf{k}_t \cdot \mathbf{r}_t + k_x x)], \quad (4.8)$$

where \mathbf{k}_t and k_x are the transverse wavevector and longitudinal wavenumber respectively, and the E-field magnitude is normalized to $|E| = 1$ without loss of generality. From Helmholtz's equation, we have

$$\frac{d^2 E}{dx^2} + k_x^2 E = 0, \quad (4.9)$$

along \hat{x} direction. The wave is propagating if $k_x = \sqrt{k^2 - k_t^2}$ is real, i.e. k_t is smaller than the wavenumber $k = \omega\sqrt{\mu\epsilon}$ where ω , μ , and ϵ are the angular frequency, permeability and permittivity respectively in the medium. Otherwise it is evanescent, indicating for imaginary k_x and $k_t > k$. Unlike the sinusoidal propagating waves, evanescent waves are localized in the near-field and vanish exponentially as plotted in Fig. 4.2. The penetration distance of an evanescent wave depends on $|k_x|$, usually only a few wavelengths.

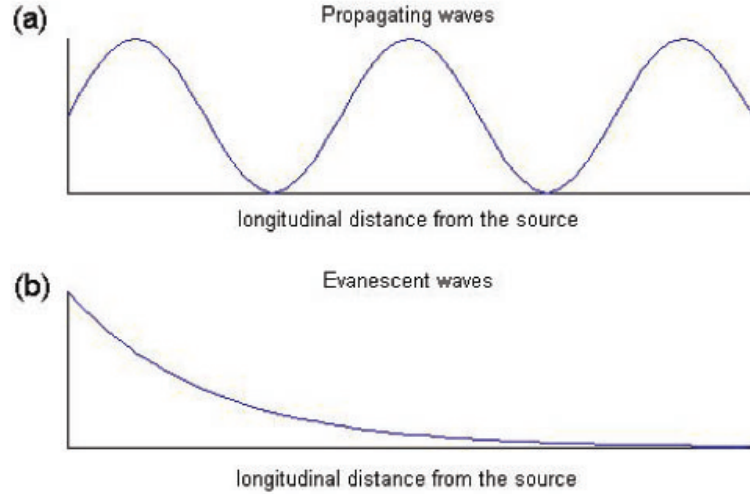


Figure 4.2: Two solution forms of electromagnetic equations: (a) Propagating wave. (b) Evanescent wave.

Compared with propagating fields, the polarization of evanescent fields are a little more complicated. Consider a homogenous dispersionless medium, the rotation of time-harmonic fields “ $\nabla \times$ ” equals “ $i\mathbf{k} \times$ ” from Helmholtz’s equation. To simplify, we assume $k_y = 0$ so that $k_t = k_z$, i.e. the wave propagates in the xoz plane. For a TE plane wave where the E-field is purely in \hat{y} direction, we solve the fields from Maxwell’s equations as follows:

$$\begin{aligned}\mathbf{E} &= -\hat{y} \exp(ik_z z + ik_x x), \\ \mathbf{H} &= \frac{1}{\eta} \left(\hat{x} \frac{k_z}{k} - \hat{z} \frac{k_x}{k} \right) \exp(ik_z z + ik_x x),\end{aligned}\quad (4.10)$$

in which $\eta = \sqrt{\mu/\epsilon}$ is the wave impedance. For propagating wave whose k_x is real, the field vectors are shown in Fig. 4.3(a); for evanescent wave with imaginary k_x , the case becomes a little different. H-field remains the same form, while E-field is no longer linearly polarized, but elliptical [147].

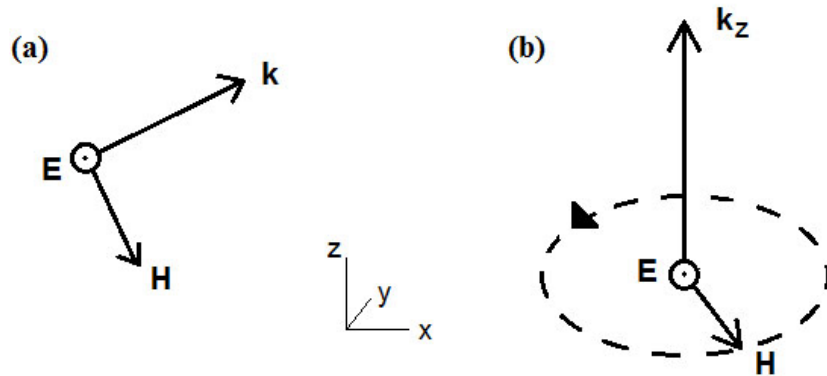


Figure 4.3: An example of TE wave patterns. (a) Propagating wave. E , H , k meets right-hand rule. (b) Evanescent wave. E is linearly polarized but H is elliptically polarized.

In the propagating wave, the fields are linearly polarized and the magnitude $|E| = \eta|H|$. However, $k_t > k$ in the evanescent wave and there is

$$|H| = \frac{|E|}{\eta} \sqrt{|k_x/k|^2 + |k_t/k|^2} = \frac{|E|}{\eta} \frac{\sqrt{(k_t^2 - k^2) + k_t^2}}{k} > \frac{|E|}{\eta}, \quad (4.11)$$

The time-averaged H-field magnitude becomes larger and the H-field polarization becomes elliptical. If $k_t \gg k$, i.e. the transverse wavenumber is extremely high, the polarization of H-field is approximately circular, whose magnitude is much larger than $|E|/\eta$. Simultaneously, with its large $|k_x|$ value, such evanescent wave decays very fast with longitudinal distance. The time-average Poynting vector which indicates the energy flow of the wave is $\mathbf{S} = \text{Re}(\mathbf{E} \times \mathbf{H}^*)/2 = \hat{x}k_z/(2k\eta)$. As a consequence, there is no time-averaged energy flux in the longitudinal direction \hat{x} for an evanescent wave.

Similarly, for a TM wave, $H = \hat{y} \exp(ik_z z + ik_x x)$, $E = \eta/k(\hat{x}k_z - \hat{z}k_x) \exp(ik_z z + ik_x x)$. Therefore the H-field is linearly polarized while the E-field is elliptical. The magnitude of the E-field is larger than ηH_0 . The representation of Poynting vector has the same format $\mathbf{S} = \text{Re}(\mathbf{E} \times \mathbf{H}^*)/2 = \hat{x}k_z/(2k\eta)$, completely lying in the transverse direction, too.

4.4 Power transportation in Frustrated Total Internal Reflection (FTIR)

In the half-space problem of TIR, no energy flux propagates into the second medium in the normal direction. The situation becomes different in the slab problem for FTIR, where a transmitted wave does tunnel through the barrier. Unlike tunneling through a periodic dielectric media where the tunneling wave is still propagating with a decaying modulation, the wave inside a FTIR barrier is purely evanescent. As in the previous section, an evanescent wave does not carry time-averaged flux in its decaying direction. So we need first figure out how the power transfer is accomplished. To answer this question, we will solve analytically the complex EM field in every point of the space and the reflection and transmission coefficients, in order to calculate the energy stored inside each region together with the energy flux along and

across the boundaries.

4.4.1 Analytical wave field derivation

To simplify, we first use a 2-D geometry and plane wave to analyze the FTIR structure as shown in Fig. 4.4. The ideal lossless medium in each region is assumed non-magnetic with permeability μ_0 . Region 1 and 3 represent two identical fiber cores while Region 2 is the cladding with a lower index. The permittivity is ϵ_1 in Regions 1 and 3, and ϵ_2 in Region 2 for the FTIR barrier. Of course there is $\epsilon_2 < \epsilon_1$. The incident angle $\theta > \tan^{-1} \sqrt{\epsilon_2/\epsilon_1}$ to ensure the TIR condition and the wave has to tunnel instead of propagate from Region 1 to Region 3. s in Fig. 4.4 is a lateral displacement for reflected and transmitted waves from the incidence position, which we will discuss in the following section.

Assuming TE polarization the incident field in the first region is

$$\begin{aligned}\mathbf{E}_i &= -\hat{\mathbf{y}} \exp[i(k_x x + k_z z)], \\ \mathbf{H}_i &= \frac{1}{\omega \mu_0} (\hat{\mathbf{x}} k_z - \hat{\mathbf{z}} k_x) \exp[i(k_x x + k_z z)].\end{aligned}\quad (4.12)$$

$k_x = k \cos \theta = \omega \sqrt{\mu_0 \epsilon_1} \cos \theta$ and $k_z = \omega \sqrt{\mu_0 \epsilon_1} \sin \theta$ denote the x and z components of the wave vector k in Region 1.

The reflected field is given by

$$\begin{aligned}\mathbf{E}_r &= -\hat{\mathbf{y}} R \exp[i(-k_x x + k_z z)], \\ \mathbf{H}_r &= \frac{R}{\omega \mu_0} (\hat{\mathbf{x}} k_z + \hat{\mathbf{z}} k_x) \exp[i(-k_x x + k_z z)],\end{aligned}\quad (4.13)$$

where $R = |R| \exp(-i\phi_r)$ is the reflection coefficient.

In Region 2, the continuity of boundary conditions determine that the transverse wavenumber k_z is the same. For such a bounded slab problem, both the exponential decaying and growing waves should exist. These two evanescent waves are the

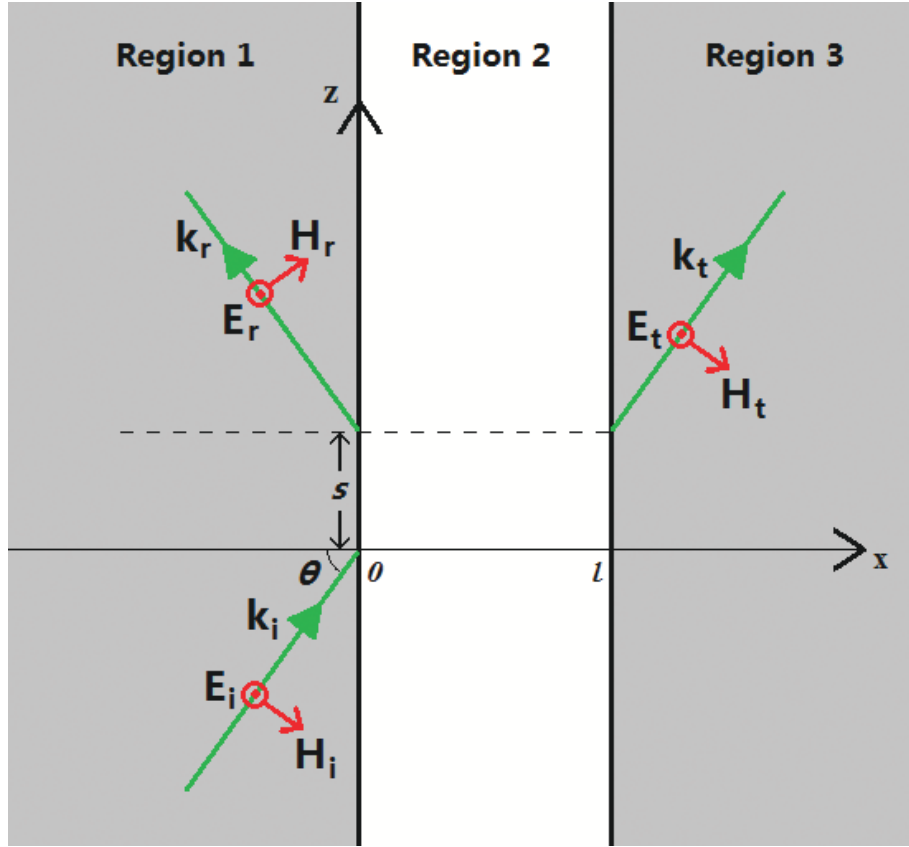


Figure 4.4: Geometry of the frustrated total internal reflection. The two cladding regions are separated by a fiber core with lower refractive index.

eigenwave solution from Maxwell's equations in this region, and can be written as:

$$\begin{aligned}
 \mathbf{E}_a &= -\hat{y}A \exp(ik_z z - \kappa x), \\
 \mathbf{H}_a &= \frac{A}{\omega\mu_0} (\hat{x}k_z - \hat{z}i\kappa) \exp(ik_z z - \kappa x), \\
 \mathbf{E}_b &= -\hat{y}B \exp(ik_z z + \kappa x), \\
 \mathbf{H}_b &= \frac{B}{\omega\mu_0} (\hat{x}k_z + \hat{z}i\kappa) \exp(ik_z z + \kappa x),
 \end{aligned} \tag{4.14}$$

where $k_2 = \omega\sqrt{\mu_0\epsilon_2}$ is the wavenumber supported in fiber core material and $k_2 < k_z$ makes it evanescent on x direction. $\kappa = \sqrt{k_z^2 - k_2^2}$ is used to describe the wave's developing or decaying along x direction, and A and B are unknown complex coefficients to be determined.

With transmission coefficient $T = |T| \exp(-i\phi_t)$, the transmitted wave is:

$$\begin{aligned}\mathbf{E}_t &= -\hat{\mathbf{y}}T \exp[i(k_x x + k_z z)], \\ \mathbf{H}_t &= \frac{T}{\omega\mu_0} (\hat{\mathbf{x}}k_z - \hat{\mathbf{z}}k_x) \exp[i(k_x x + k_z z)],\end{aligned}\quad (4.15)$$

There are four unknown complex coefficients R , T , A and B above in total. With boundary conditions at $x = 0$, we have

$$\begin{aligned}E_{iy} + E_{ry} &= E_{ay} + E_{by}, \\ H_{iz} + H_{rz} &= H_{az} + H_{bz}.\end{aligned}\quad (4.16)$$

At the second boundary $x = l$, we also have

$$\begin{aligned}E_{ty} &= E_{ay} + E_{by}, \\ H_{tz} &= H_{az} + H_{bz}.\end{aligned}\quad (4.17)$$

By substituting Eq. (4.13) – (4.15) into the boundary conditions, we have four linear equations with four unknown coefficients:

$$\begin{aligned}1 + R &= A + B, \\ -k_x(1 - R) &= i\kappa(B - A), \\ T \exp(ik_x l) &= A \exp(-\kappa l) + B \exp(\kappa l), \\ -k_x T \exp(ik_x l) &= i\kappa[-A \exp(-\kappa l) + B \exp(\kappa l)].\end{aligned}\quad (4.18)$$

The solution to Eq. (4.18) is:

$$\begin{aligned}
A &= \frac{-2k_x (i\kappa - k_x) \exp(2\kappa l)}{(k_x + i\kappa)^2 + (ik_x + \kappa)^2 \exp(2\kappa l)} \\
B &= \frac{-2k_x (i\kappa + k_x)}{(k_x + i\kappa)^2 + (ik_x + \kappa)^2 \exp(2\kappa l)} \\
R &= \frac{(k_x^2 + k_z^2 - k_2^2) [1 - \exp(2\kappa l)]}{(k_x + i\kappa)^2 + (ik_x + \kappa)^2 \exp(2\kappa l)} \\
T &= \frac{4ik_x \kappa \exp [(-ik_x + \kappa) l]}{(k_x + i\kappa)^2 + (ik_x + \kappa)^2 \exp(2\kappa l)}. \tag{4.19}
\end{aligned}$$

By solving the optical fields in all three regions, so far we have determined the fields in every point. From the field solutions, we have the reflectance $|R|^2$ and transmittance $|T|^2$ as

$$|R|^2 = \frac{2(k_x^2 + \kappa^2)^2 \sinh^2(\kappa l)}{-k_x^4 + 6k_x^2 \kappa^2 + (k_x^2 + \kappa^2)^2 \cosh(2\kappa l)}, \tag{4.20}$$

$$|T|^2 = \frac{8k_x^2 \kappa^2}{-k_x^4 + 6k_x^2 \kappa^2 + (k_x^2 + \kappa^2)^2 \cosh(2\kappa l)}. \tag{4.21}$$

The lossless relationship $|R|^2 + |T|^2 = 1$ is maintained here. There is an amount of $|T|^2$ power tunneling into Region 3 through FTIR. Note that only evanescent waves are allowed inside the barrier gap. Next, we will illustrate how the power transfers across the gap with these two evanescent eigenwaves.

4.4.2 Power tunneling through the barrier

In Region 2, there are only two evanescent eigenwaves as in Eq. (4.14). As known from section 4.3, none of these eigenwaves have a nonzero time-averaged longitudinal flux. Nevertheless, the total field in this region is given by their superposition

$$\begin{aligned}
\mathbf{E} &= \mathbf{E}_a + \mathbf{E}_b, \\
\mathbf{H} &= \mathbf{H}_a + \mathbf{H}_b. \tag{4.22}
\end{aligned}$$

Then we can get the time-averaged Poynting vector in Region 2 along \hat{x} direction

$$S_{2x} = \frac{1}{2} \text{Re} [(\mathbf{E}_a + \mathbf{E}_b) \times (\mathbf{H}_a^* + \mathbf{H}_b^*)]_x. \quad (4.23)$$

By evaluating it with Eq. (4.14), we have

$$S_{2x} = \frac{i\kappa}{2\omega\mu_0} \text{Re} (AB^* - BA^*) = \frac{\kappa \text{Im}[AB^*]}{\omega\mu_0}. \quad (4.24)$$

Only the interference terms are left after removing the zero time-averaged longitudinal Poynting vectors for each evanescent eigenwave. Because of such interference, a nonzero power intensity S_{2x} is generated to transfer power inside the barrier. It is the interference between growing and decaying evanescent waves that tunnels time-averaged power in the normal direction across FTIR barrier. By substituting the coefficients from Eq. (4.19), after some math we get

$$S_{2x} = |R|^2 \frac{2k_x^3 \kappa^2}{\omega\mu_0 \sinh^2(\kappa l) (k_x^2 + \kappa^2)^2} \quad (4.25)$$

In Regions 1 and 3, we can verify that

$$\begin{aligned} S_{1x} &= \frac{1}{2} \text{Re} [(\mathbf{E}_i + \mathbf{E}_r) \times (\mathbf{H}_i^* + \mathbf{H}_r^*)]_x \\ &= \frac{k_x}{2\omega\mu_0} (1 - |R|^2) + \frac{k_x}{4\omega\mu_0} \text{Im} [R \exp(-2ik_x x)], \\ S_{3x} &= \frac{1}{2} \text{Re} [\mathbf{E}_t \times \mathbf{H}_t^*]_x \\ &= \frac{1}{2} \frac{k_x}{\omega\mu_0} |T|^2 = S_{2x}. \end{aligned} \quad (4.26)$$

At the boundary of $x = 0$, we can reduce S_{1x} to be

$$S_{1x} = \frac{k_x}{2\omega\mu_0} (1 - |R|^2) = S_{2x} = S_{3x}. \quad (4.27)$$

Here the power flow on \hat{x} direction is conserved during FTIR tunneling process. Meanwhile, there is some interference between the incident and reflected wave in Region 1, putting a periodical oscillatory term in every wavelength until reaching its boundary with Region 2. Such oscillatory term does not affect the power transferred across the barrier. Once it enters the barrier, the flux in normal direction becomes a constant.

On the transverse direction, however, there is a lateral displacement which requires special care during the tunneling process, known as the Goos-Hänchen effect. A lateral power flow in \hat{z} direction is a straight-forward conclusion in FTIR corresponding to the nonzero transverse Poynting vectors S_{1z} , S_{2z} and S_{3z} . It is such lateral power flow that leads to the lateral displacement on the origin of reflected/transmitted wave from the incidence point.

4.5 Goos-Hänchen shift

In Fig. 4.4, s denotes a small lateral displacement on \hat{z} of the reflected/transmitted beam from the TE incident point ($x = 0, z = 0$) in FTIR condition. Besides the lateral spatial displacement, there is also a phase shift between the incident wave and reflected/transmitted wave. Both spatial and phase shifts are related to the FTIR incident angle. Since it is oblique incidence, there is always a transverse power flow during the tunneling time.

During quasi-static FTIR tunneling, the incident energy is first temporarily stored as the self-interference in the overlapping of the incident and reflected waves (in Region 1), and also in the evanescent fields inside the barrier (in Region 2). Then the energy gets released as either reflection or transmission after its lifetime. As a consequence, the lateral Goos-Hänchen shift is a result of the transverse power flow in front of and inside the gap in physics.

The calculation of the tunneling group delay in FTIR depends on the result of

Goos-Hänchen shift. So we need quantitatively derive the Goos-Hänchen shift before starting analyzing the group delay. There are two major approaches for Goos-Hänchen shift calculation.

4.5.1 Stationary-phase method

Conventionally, Goos-Hänchen effect is considered a coherence phenomenon of finite incident and reflected beams [119, 148]. The Goos-Hänchen shift as well as the group delay time are determined from the points of stationary-phase condition [149]. In this approach we consider a finite beam incidence with a small range of incident angles in space, and with a small range of wave frequencies in time. In FTIR, the locus of the incident beam is determined by a stationary point of the phase:

$$\frac{\partial \Phi_I}{\partial \theta} = 0, \quad (4.28)$$

in which $\Phi_I = (k \cos \theta)x + (k \sin \theta)z - \omega t$ is the total phase of the incident beam. A locus can accurately track the center line of the beam with a stationary phase point. The lateral Goos-Hänchen shift can be determined with this idea, by comparing the incidence locus position at the barrier entrance ($x = 0, z = 0$) and the reflected or transmitted locus positions at the barrier exits [150, 151].

For the incident wave, the locus is $z = x \tan \theta$. At the barrier entrance, the locus $z(0) = 0$. For the transmitted beam, $\Phi_T = -\phi_t + (k \cos \theta)x + (k \sin \theta)z - \omega t$ and the locus at the barrier exit ($x = l, z = s$) is determined by $\partial \Phi_T / \partial \theta = 0$. The result is

$$z(l) = l \tan \theta + \frac{\partial \phi_t / \partial \theta}{k \cos \theta}. \quad (4.29)$$

The lateral displacement between them is Goos-Hänchen shift s for the transmitted beam, i.e. $s = z(l) - z(0) = l \tan \theta + \frac{\partial \phi_t / \partial \theta}{k \cos \theta}$. With the solution of transmission coefficient T from Eq. (4.19), we may get the final result for Goos-Hänchen shift.

Similarly, solving the locus for the reflected beam, we are able to prove that the Goos-Hänchen shift s remains the same for reflected or transmitted beams. Such representation of s is related to the derivative of the Fresnel transmission/reflection phase shifts to the incidence angle, whose physical meaning is not obvious enough and it is not a direct result for judging the causality of the lateral shift.

With the same idea, the tunneling group delay can be solved by the stationary phase in time domain [148, 150–155]. As an analog that the locus of a finite spatial beam defined by $\partial\Phi/\partial\theta = 0$, the peak of a finite temporal pulse is defined by $\partial\Phi/\partial\omega = 0$. After similar algebra, the time delay between the pulse peaks entering and exiting the barrier is

$$\tau_g = -\frac{\partial\phi_t}{\partial\omega} + s\frac{\partial k_z}{\partial\omega} = \tau_F + \tau_{GH}, \quad (4.30)$$

where the first term τ_F relates to the Fresnel transmission phase shift, and the second term τ_{GH} is the Goos-Hänchen shift divided by group velocity on lateral direction $1/(\partial k_z/\partial\omega)$.

It is noted that if the exit of the barrier is defined as the reflection point rather than the transmission point, temporal delay remains the same after calculations, similar to the lateral Goos-Hänchen displacement. Hence the tunneling process differs from ordinary propagation. When the light energy gets released from the barrier, it does not differentiate whether going forward as transmission or backward as reflection.

One drawback with this approach is the tendency to ascribe the Fresnel term τ_F term to a longitudinal traversal time. Because this term vanishes in the limit of a thick barrier, there have been claims of instantaneous barrier traversal by some workers [133]. While the Goos-Hänchen term can be associated with a transverse propagation because of the real wave vector in that direction, the term τ_F cannot be associated with longitudinal propagation since the fields in that direction are evanescent. In addition, it is not clear whether the Fresnel term τ_F also contains contribution from lateral shift or not from this method.

As in the analogous phenomenon of quantum tunneling, the interpretation of this delay time has been controversial. For many years the group delay in tunneling has been taken to be the traversal time of a wave packet from the entrance to the exit of a barrier. Such an interpretation leads to endless difficulties, including a traversal time that becomes independent of barrier thickness, a phenomenon known as the Hartman effect [139].

Next we will introduce the other approach named energy flux method.

4.5.2 Energy flux method

Another definition of Goos-Hänchen shift is closely related to energy flux. There is a time delay between the reflection/transmission wave and the incidence wave, at the moment of light incidence on the barrier's entrance, the incident energy flux is not instantly reflected or transmitted away, but have to stay for a little while. Therefore it becomes possible to evaluate Goos-Hänchen shift in the viewpoint of energy conservation.

In Section 4.4 we have shown that there exists a transverse energy flux in Region 2 carried by the evanescent eigenwaves along \hat{z} . For the energy conservation in lossless medium, the lateral power flow inside barrier completely sources from the incidence, i.e. there must be an equal amount of incident energy flux penetrating across the boundary between Region 1 and 2 in Fig. 4.5 [156, 157]. Simultaneously, the lateral energy flux in Region 1 is not simply the sum of incident and reflected lateral energy fluxes. There is some interference between the incident and reflected wave which also contributes an additional lateral energy flux. Such interference occurs in the overlapping area in Region 1, and often referred as “self-interference”, which is an important part for Goos-Hänchen shift as well as the group delay.

The “self-interference” energy flux can be evaluated by introducing an appropriate averaging process into the integral of the energy-flux density over the region of overlap

of the two waves.

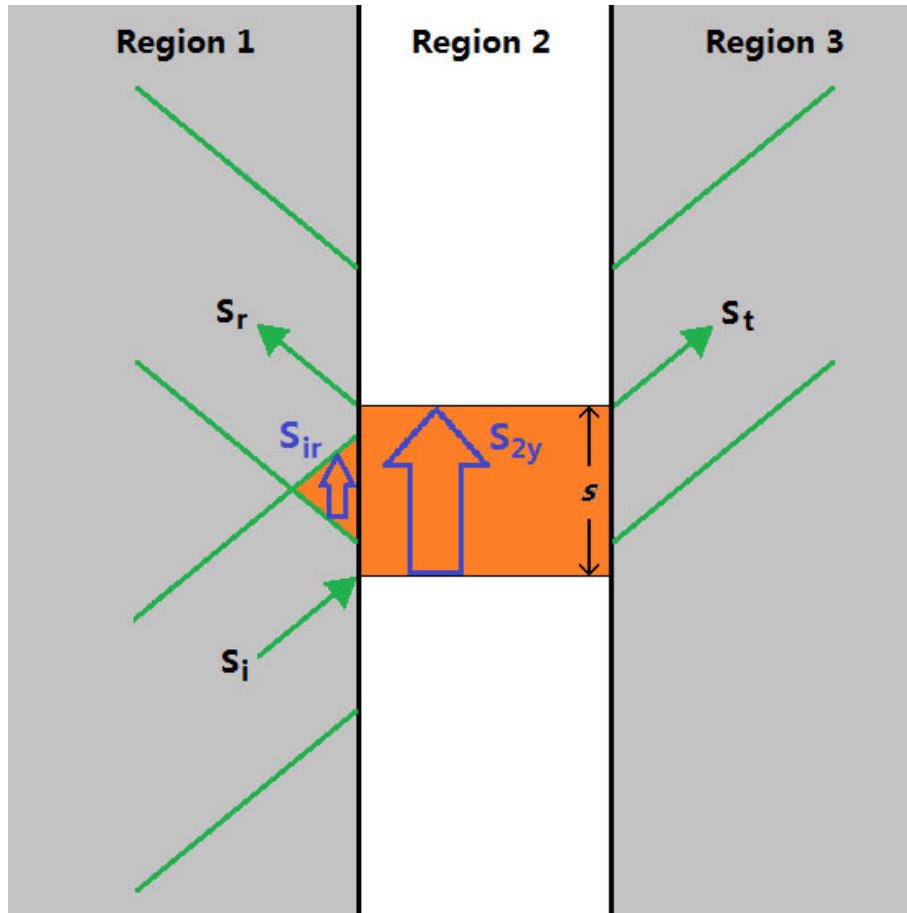


Figure 4.5: The power flux chart for FTIR. There is a Goos-Hänchen shift between the incident wave and the reflected/transmitted wave.

To sum up, from the view of the lateral energy flux during a TIR or FTIR process in a lossless structure, the incident energy is stored in two places: inside the barrier in the form of evanescent fields, and in the overlapping area in front of the barrier in the form of self-interference between incident and reflected waves. These two parts of energy correspond to the two orange shaded areas in Fig. 4.5. The prior one first enters Region 2, and then moves upward along \hat{z} direction unless its dwell time in the barrier expires. Finally it exits the barrier as the reflected or transmitted wave. So the total lateral energy flux of this part can be written as $\int_0^l S_{2z} dx$, as an integral from $x = 0$ to l . The latter one, nevertheless, gets internally reflected and remained

in Region 1. It is temporarily stored as the self-interference energy in the overlapping area between incident and reflected beams. It also flows upward along \hat{z} direction as shown in Fig. 4.5. In general, the overlapping area may extend to infinitely long away if the beam is as wide as plane wave. Therefore, such energy flux can be written as $\int_{-\infty}^0 S_{irz} dx$, where

$$S_{irz} = S_{1z} - S_{iz} - S_{rz} = \frac{1}{2} \text{Re} (\mathbf{E}_i \times \mathbf{H}_r^* + \mathbf{E}_r \times \mathbf{H}_i^*)_z. \quad (4.31)$$

In Section 4.4 we have shown that the \hat{x} component of the self-interference energy flux provides an the oscillating term in S_{1x} , which can be eliminated in the manner by averaging over a distance l and taking the limit as l goes to infinity or by simply integrating over a wavelength. So only the non-oscillatory z component of the self-interference energy flux, i.e. S_{irz} , is taken into account.

On the other hand, this transverse energy flux is induced by the light incidence on the boundary $x = 0$. If we consider the normal direction, all the normal components of incident flux reach the barrier's entrance and get temporarily stored (either inside the barrier or in front of the barrier). After the time of group delay, they are released to produce the normal components of reflected and transmitted waves away from the barrier.

Based on energy conservation, the total amount of energy flux temporarily stored and released need to equal, no matter we consider it in \hat{x} or \hat{z} direction. So we have

$$\int_0^l S_{2z} dx + \int_{-\infty}^0 S_{irz} dx = \int_0^s S_{ix} dz = S_{ix}s, \quad (4.32)$$

where s is the lateral Goos-Hänchen shift. Therefore

$$\begin{aligned}
s &= \frac{\int_0^l S_{2z} dx}{S_{ix}} + \frac{\int_{-\infty}^0 S_{irz} dx}{S_{ix}}, \\
&= \frac{\int_0^l S_{2z} dx}{\int_0^l w_2 dx} \frac{\int_0^l w_2 dx}{S_{ix}} + \frac{\int_{-\infty}^0 S_{irz} dx}{\int_{-\infty}^0 w_{ir} dx} \frac{\int_{-\infty}^0 w_{ir} dx}{S_{ix}}.
\end{aligned} \tag{4.33}$$

The result in Eq. (4.33) can be connected with explicit physical meanings. We start with the energy transport velocity which is defined as the Poynting vector over the energy density of the electromagnetic field, i.e. $v_e = S/w$ [158]. In time-harmonic field we take the time-averaged values for S and w . Thus energy velocity in the barrier along the propagation direction \hat{z} can be given as $v_{2z} = S_{2z}/w_2$ with energy density in the barrier $w_2 = \frac{1}{4}[\epsilon_2|\mathbf{E}_a + \mathbf{E}_b|^2 + \mu_0|\mathbf{H}_a + \mathbf{H}_b|^2]$ and transverse Poynting vector $S_{2z} = \frac{1}{2}\text{Re}[(\mathbf{E}_a + \mathbf{E}_b) \times (\mathbf{H}_a + \mathbf{H}_b)^*]_z$.

It is noted that the energy velocity v_{2z} in the barrier is a function of the position x . Each point in Region 2 may have its own velocity of lateral energy movement. From a total view of the energy transport rates in the whole region, we need a weighted average $\langle v_{2z} \rangle$ as the sum of energy fluxes over the sum of EM energy in Region 2:

$$\langle v_{2z} \rangle = \frac{\int_0^l S_{2z} dx}{\int_0^l w_2 dx}. \tag{4.34}$$

Similarly, we have the weighted averaged self-interference energy velocity $\langle v_{irz} \rangle$ as

$$\langle v_{irz} \rangle = \frac{\int_{-\infty}^0 S_{irz} dx}{\int_{-\infty}^0 w_{ir} dx}. \tag{4.35}$$

We divide it with w_{ir} instead of the total energy $w_1 = \frac{1}{4}[\epsilon_1|\mathbf{E}_i + \mathbf{E}_r|^2 + \mu_0|\mathbf{H}_i + \mathbf{H}_r|^2] = w_i + w_r + w_{ir}$, because the temporarily stored energy (during the time after the incident wave enters and before the reflected wave comes out) does not include w_i or w_r .

The energy dwell time in the barrier is defined as

$$\tau_d = \frac{\int_0^l w_2 dx}{S_{ix}}, \quad (4.36)$$

and the self-interference time indicating the energy dwelled in the overlapping region of incident and reflected beams is obtained by

$$\tau_i = \frac{\int_{-\infty}^0 w_{ir} dx}{S_{ix}}. \quad (4.37)$$

By substituting Eq. (4.34) – (4.37) into (4.33), we have the Goos-Hänchen shift as

$$s = \langle v_{2z} \rangle \tau_d + \langle v_{irz} \rangle \tau_i. \quad (4.38)$$

Obviously, s is the sum of two terms: the barrier dwell time multiplied by the average energy speed in the barrier, and the self-interference time multiplied by the average energy speed in the self-interference region.

Using Eq. (4.33), we may calculate the final result for s with the field solution we derived in the Section 4.4. We have

$$\begin{aligned} S_{2z} &= \frac{1}{2} \text{Re}[(\mathbf{E}_a + \mathbf{E}_b) \times (\mathbf{H}_a + \mathbf{H}_b)^*]_z \\ &= \frac{k_z}{2\omega\mu_0} [|A|^2 \exp(-2\kappa x) + |B|^2 \exp(2\kappa x) + 2\text{Re}(AB^*)], \end{aligned} \quad (4.39)$$

$$S_{irz} = \frac{1}{2} \text{Re}(\mathbf{E}_i \times \mathbf{H}_r^* + \mathbf{E}_r \times \mathbf{H}_i^*) = \frac{k_z}{\omega\mu_0} |R| \cos(\phi_r + 2k_x x), \quad (4.40)$$

$$S_{ix} = \frac{1}{2} \text{Re}(\mathbf{E}_i \times \mathbf{H}_i^*) = \frac{k_x}{2\omega\mu_0}. \quad (4.41)$$

The final representation of the Goos-Hänchen shift s is

$$\begin{aligned}
s &= \frac{k_z}{k_x} \left[(|A|^2 e^{-2\kappa l} + |B|^2) \frac{e^{2\kappa l} - 1}{2\kappa} + 2\text{Re}(AB^*)l \right] + \frac{k_z}{k_x^2} |R| \sin \phi_r \\
&= |R|^2 k_x k_z \frac{2\kappa l (\kappa^2 - k_x^2) + (\kappa^2 + k_x^2) \sinh(2\kappa l)}{\kappa (\kappa^2 + k_x^2)^2 \sinh^2(\kappa l)}, \tag{4.42}
\end{aligned}$$

and it matches the result from stationary-phase calculation.

4.5.3 Causality in lateral propagation

Here we will discuss on the causality in lateral direction by Goos-Hänchen effect using Eq. 4.38. In \hat{z} direction, the wave is propagating, no matter whether it is outside or inside the barrier. The lateral direction is different from the normal direction. The latter one is not propagation, but energy storage and release process. The lateral displacement need be causal as a movement of energy, in order to make physical senses with special relativity.

To prove the causality of the lateral shift, we need to show that the energy velocity at any given point (not the averaged velocity over some area) in the self-interference area v_{irz} or in the barrier v_{2z} is smaller than c . In an ideal lossless medium, $c = 1/\sqrt{\mu_0 \epsilon_0} = \omega/k_0 \geq \omega/k_2$. To begin with, we first focus on the velocity v_{irz} in front of the barrier. The time-averaged energy density of the self-interference field in Region 1 is

$$\begin{aligned}
w_{ir} &= \frac{1}{4} [\epsilon_1 (\mathbf{E}_i \cdot \mathbf{E}_r^* + \mathbf{E}_r \cdot \mathbf{E}_i^*) + \mu_0 (\mathbf{H}_i \cdot \mathbf{H}_r^* + \mathbf{H}_r \cdot \mathbf{H}_i^*)] \\
&= \frac{k_z^2}{\omega^2 \mu_0} |R| \cos(\phi_r + 2k_x x). \tag{4.43}
\end{aligned}$$

The lateral self-interference energy velocity becomes

$$v_{irz} = \frac{S_{irz}}{w_{ir}} = \frac{\frac{k_z |R|}{\omega \mu_0} \cos(\phi_r + 2k_x x)}{\frac{k_z^2 |R|}{\omega^2 \mu_0} \cos(\phi_r + 2k_x x)} = \frac{\omega}{k_z}, \quad (4.44)$$

for every position. Actually it is the same lateral velocity as the incident or reflected waves. In other words, in Region 1, the lateral power of incident, reflected, and self-interference terms moves with a uniform velocity. Since $k_z > k_2 \geq k_0$, we have $v_{irz} < c$. The \hat{x} component of the self-interference energy flux is oscillatory and can be eliminated in the manner by averaging over a distance l , so the energy velocity is also causal on the normal direction in Region 1.

The time-averaged energy density of the total field in Region 2 is

$$\begin{aligned} w_2 &= \frac{1}{4} [\epsilon_2 |\mathbf{E}_a + \mathbf{E}_b|^2 + \mu_0 |\mathbf{H}_a + \mathbf{H}_b|^2] \\ &= \frac{k_z^2}{2\omega^2 \mu_0} [|A|^2 \exp(-2\kappa x) + |B|^2 \exp(2\kappa x)] + \frac{k_2^2}{\omega^2 \mu_0} \text{Re}(AB^*). \end{aligned} \quad (4.45)$$

It is important to note that both $|A|^2 \exp(-2\kappa x)$ and $|B|^2 \exp(2\kappa x)$ are always real numbers for all x positions. Then the inequality applies:

$$|A|^2 \exp(-2\kappa x) + |B|^2 \exp(2\kappa x) \geq 2|A||B|, \quad (4.46)$$

and also we have

$$\text{Re}(AB^*) = |A||B| \cos(\phi_A - \phi_B) \leq |A||B|. \quad (4.47)$$

Recall that $k_z > k_2$ for the FTIR condition. Therefore the energy density stored in

the barrier gap has a minimum of

$$\begin{aligned}
w_2 &= \frac{k_2 k_z}{2\omega^2 \mu_0} [|A|^2 \exp(-2\kappa x) + |B|^2 \exp(2\kappa x)] + \frac{k_2^2}{\omega^2 \mu_0} \text{Re}(AB^*) \\
&\quad + \frac{k_z(k_z - k_2)}{2\omega^2 \mu_0} [|A|^2 \exp(-2\kappa x) + |B|^2 \exp(2\kappa x)] \\
&\geq \frac{k_2 k_z}{2\omega^2 \mu_0} [|A|^2 \exp(-2\kappa x) + |B|^2 \exp(2\kappa x)] + \frac{k_2^2}{\omega^2 \mu_0} \text{Re}(AB^*) + \frac{k_z(k_z - k_2)}{\omega^2 \mu_0} |A||B| \\
&> \frac{k_2 k_z}{2\omega^2 \mu_0} [|A|^2 \exp(-2\kappa x) + |B|^2 \exp(2\kappa x)] + \frac{k_2^2}{\omega^2 \mu_0} \text{Re}(AB^*) + \frac{k_2(k_z - k_2)}{\omega^2 \mu_0} |A||B|,
\end{aligned} \tag{4.48}$$

and similarly, the Poynting vector S_{2z} in Eq. (4.39) has a maximum

$$\begin{aligned}
S_{2z} &= \frac{k_z}{2\omega \mu_0} [|A|^2 \exp(-2\kappa x) + |B|^2 \exp(2\kappa x)] + \frac{k_2}{\omega \mu_0} \text{Re}(AB^*) + \frac{k_z - k_2}{\omega \mu_0} \text{Re}(AB^*) \\
&\leq \frac{k_z}{2\omega \mu_0} [|A|^2 \exp(-2\kappa x) + |B|^2 \exp(2\kappa x)] + \frac{k_2}{\omega \mu_0} \text{Re}(AB^*) + \frac{k_z - k_2}{\omega \mu_0} |A||B|
\end{aligned} \tag{4.49}$$

By dividing Eq. (4.49) by Eq. (4.48) at their upper/lower limits, we have the limit for v_{2z}

$$v_{2z} = \frac{S_{2z}}{w_2} < \frac{\omega}{k_2} \leq c. \tag{4.50}$$

It is seen that the \hat{z} direction propagation velocity is also causal for any points inside the barrier in Region 2.

The lateral shift s is accomplished by two parts of causal lateral energy movement v_{irz} and v_{2z} as in Eq. (4.38).

On the other hand, there is tunneling instead of propagation in the normal direction from $x = 0$ to $x = l$ across the barrier. We cannot directly apply this energy velocity method to tunneling. Without propagation, it no longer has explicit physical meanings. The tunneling time is given by group delay, the time difference between the peak of the incident wave packet enters and exits the barrier. Our next task is

to decide the tunneling time that a pulse peak is delayed during FTIR tunneling, i.e. group delay.

4.6 Tunneling group delay for pulses

We are able to calculate the group delay time with the Goos-Hänchen shift given above. Again, we emphasize the quasi-static condition for the laser pulse tunneling, with a pulse duration much longer than the tunneling group delay. Operationally, if a wave packet attains a peak at time $t = 0$ at the entrance $x = 0$ of a barrier, the group delay tells us the time at which a wave-packet peak appears at the exit $x = L$. However, the peak at $x = L$ and the peak at $x = 0$ need not be related by causal translation; indeed there is no requirement that they be the same peak [135, 159].

Another measure of the duration of a tunneling event is the dwell time [135, 139]. This is the time spent in the barrier, distributed over both entrance and exit channels. Because the dwell time does not differentiate between input and exit channels, it is not considered a traversal time [130, 137]. Like the group delay, however, it also saturates with barrier length.

In general the group delay and dwell time differ by a quantity known as the self-interference delay [140]. This self-interference delay has been calculated explicitly for 1-D quantum tunneling of nonrelativistic [140] and relativistic particles [143], as well as for the tunneling of classical electromagnetic waves through undersized waveguides [136] and photonic band-gap structures [160]. For the case of frustrated total internal reflection which is inherently a 2-D tunneling problem, we independently derive an explicit expression for the self-interference delay in FTIR by calculating the energy density in the overlap between incident and internally reflected waves in the fiber core of incidence. This demonstrates explicitly the physical meaning of the self-interference delay as an additional dwell time in front of the barrier due to the overlap between incident and reflected waves.

To begin with, we will explore the energy dwell time and the self-interference time respectively, and then show that their sum is exactly the group delay for FTIR tunneling.

4.6.1 Energy dwell time and self-interference time

Using Eq. (4.36), we can calculate the energy dwell time inside the barrier:

$$\begin{aligned}\tau_d &= k_z^2 \frac{e^{2\kappa l} - 1}{k_x \omega} \frac{|A|^2 e^{-2\kappa l} + |B|^2}{2\kappa} + \frac{2k_z^2 l}{k_x \omega} \text{Re}[AB^*] \\ &= |R|^2 k_x \frac{2k_z^2 \kappa l (\kappa^2 - k_x^2) + k_z^2 (\kappa^2 + k_x^2) \sinh(2\kappa l)}{\omega \kappa (\kappa^2 + k_x^2)^2 \sinh^2(\kappa l)}.\end{aligned}\quad (4.51)$$

The temporarily stored energy will get released from both the reflection and transmission side of the barrier, after its dwell time is reached. For tunneling, it is not wave traversal time from one side to another side where a propagation velocity is physically defined. Instead, the barrier performs as a lumped element and the dwell time describes the time between the energy entering and exiting the barrier.

Using Eq. (4.37), we can get the self-interference time

$$\begin{aligned}\tau_i &= \frac{\frac{k_z^2}{\omega^2 \mu_0} |R| \sin \phi_r}{\frac{k_x}{2\omega \mu_0}} \\ &= \frac{k_z^2 |R| \sin \phi_r}{k_x^2 \omega} = \frac{\text{Im}(R)}{\omega} \tan^2 \theta.\end{aligned}\quad (4.52)$$

Equation (4.52) represents an explicit and independent calculation of the self-interference delay for a 2-D tunneling problem, starting from its physical meaning as a delay due to the interaction energy in front of the barrier. It shows how the ratio of transverse-to-longitudinal components of the wave vector modifies the basic $1/\omega$ dependence of the self-interference delay.

The interference delay is directly proportional to the stored energy in the overlap

of incident and reflected waves in front of the barrier. This energy saturates since it is proportional to the reflection coefficient, which saturates with barrier length.

4.6.2 Group delay

The transmission coefficient is $T = |T| \exp(-i\phi_t)$. Meanwhile, there is a lateral Goos-Hänchen shift s as well as a longitudinal shift of l . The incident wave phase at the barrier entrance ($x = 0, z = 0$ in Fig. 4.4) is $\Phi_I = k_z z + k_x x = 0$, while the transmitted wave phase at the barrier exit ($x = l, z = s$) is $\Phi_T = -\phi_t + k_z s + k_x l$. The phase change from the incident to the transmitted wave includes two components. The first one is the Fresnel coefficients and the longitudinal phase shift $-\phi_t + k_x l$. The other comes from the transverse Goos-Hänchen shift $k_z s$. The group delay, calculated as the frequency derivative of the total phase shift in the $\exp(-i\omega t)$ time-harmonic system, is given by

$$\tau_g = \frac{\partial \phi_T}{\partial \omega} = \frac{\partial(k_x l - \phi_t)}{\partial \omega} + \frac{\partial k_z}{\partial \omega} s + k_z \frac{\partial s}{\partial \omega}. \quad (4.53)$$

From Eq. (4.19), we have

$$\phi_t = k_x l - \frac{\pi}{2} - \tan^{-1} \left[\frac{2k_x \kappa \cosh(\kappa l)}{(\kappa^2 - k_x^2) \sinh(\kappa l)} \right]. \quad (4.54)$$

After substituting the value of ϕ_t and s from Eq. (4.19) and (4.42) and some simplifications, we get the derivatives

$$\frac{\partial(k_x l - \phi_t)}{\partial \omega} = \frac{2k_x \kappa^2 l (k_x^2 - \kappa^2) / \omega}{4k_x^2 + (k_x^2 - \kappa^2)^2 \sinh^2(\kappa l)}, \quad (4.55)$$

so the value of τ_g is given by

$$\tau_g = \frac{2k_x^2 \kappa^2 l (\kappa^2 - k_x^2) + k_z^2 (k_x^2 + \kappa^2) (k_x^2 + i\kappa^2) \sinh(2\kappa l)}{\omega k_x \kappa [4k_x^2 \kappa^2 \cosh^2(\kappa l) + (k_x^2 - \kappa^2)^2 \sinh^2(\kappa l)]}. \quad (4.56)$$

This result matches the one from stationary-phase method in Section 4.5.1 [151].

Also, it is possible to define the barrier exit as ($x = 0, z = s$) for the reflected wave. In this case, the group delay is

$$\tau_g' = \frac{\partial \Phi_R}{\partial \omega} = \frac{\partial(-\phi_r + k_z s)}{\partial \omega}. \quad (4.57)$$

With the value of ϕ_r from Eq. (4.19), it is seen that the group delay for the reflected wave is exactly the same, i.e. $\tau_g' = \tau_g$.

From Eq. (4.51), (4.52) and (4.56), it is possible to verify the relationship

$$\tau_g = \tau_d + \tau_i. \quad (4.58)$$

For TM polarized incidences, the same relationship holds.

From the definition of τ_d and τ_i in Eq. (4.36) and (4.37), it is seen that τ_g can be represented as $\tau_g = \left(\int_{-\infty}^0 w_{ir} dx + \int_0^l w_2 dx \right) / S_{ix}$. If we consider the energy stored inside barrier w_2 (by evanescent fields) and in front of the barrier w_{ir} (by self-interference) as a whole, the group delay in FTIR is exactly the lifetime of this total amount of energy. The physical meaning of Eq. (4.58) is that the group delay describes a process of energy temporary storage and release both inside and in front of the barrier, instead of a propagation.

The tunneling group delay shares the same status as the dwell time in that it is a property of an entire wave function with forward and backward components which cannot be disentangled. As a result, in the presence of reflections, neither time is a transit time and cannot be used to calculate a physically meaningful velocity in the tunneling longitudinal direction. While the dwell time is never interpreted as a traversal time because it does not differentiate between entrance and exit channels, it has hitherto not been recognized that the group delay shares the same status. The group delay is a property of an entire wave function with transmitted and reflected

components, both of which are needed for tunneling to occur. They both represent the lifetime of stored energy in the cavity formed by the cladding between the cores, and in the region of beam overlap [137, 138, 142].

4.7 Conclusion

Both τ_g and s are functions of ω , therefore different frequency components will have slightly different tunneling group delay and lateral displacement. However, the size of the directional coupler is small. Depending on the incident angle, a typical value for the group delay τ is in the order of 10fs and Goos-Hächen shift s is in microns. Comparing to the cavity roundtrip length (e.g. 8m) and time (e.g. 40ns), both s and τ_g are too small to introduce some non-negligible impact. So the beam combining models in Chapters II and III directly use the coupled-mode transfer matrix Eq. (4.7), without taking the detail dynamic tunneling processes into account.

From either stationary-phase or energy flux conservation viewpoint, both reflected and transmitted waves share the same Goos-Hänchen shift s and the same group delay τ_g . We have pointed out that Goos-Hänchen shift is contributed from the lateral energy flow by self-interference in Region 1 and by the evanescent waves in Region 2. Also, the reflected and transmitted waves have an identical group delay τ_g , whose physical meaning is justified. Instead of traverse time, it is storage time for energy above and inside the barrier, which do not differentiate the direction to exit.

The conclusion that s and τ_g are identical for reflected and transmitted wave guarantees that a quasi-static optical pulse does not break up during the tunneling process. Fig. 4.6 indicates the ray optics of coupling, where an incident ray (or locus) from the upper fiber gets divided into reflected and transmitted rays by FTIR (red and green lines) at $z = 0$. Since the reflected and transmitted rays experience exactly the same optical path inside two identical fiber cores, they meet again at the same position $z = b + s + s'$. Then each of them splits into two parts again

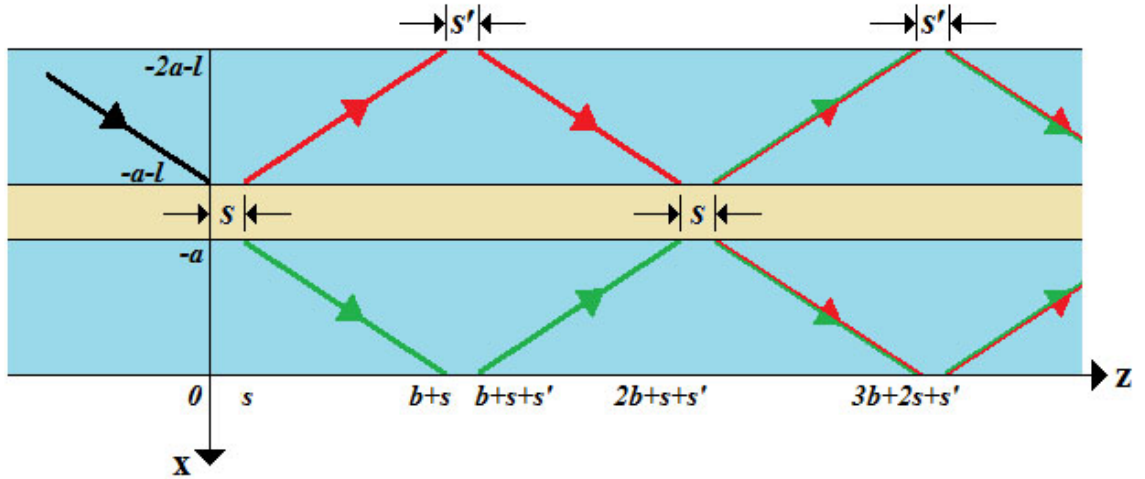


Figure 4.6: FTIR ray figure of beam combining in a directional coupler, where s is the Goos-Hänchen shift for FTIR and s' is the Goos-Hänchen shift for TIR.

and hence exchanges the power between two fiber cores. All rays reach the barrier interface again at $z = b + 2s + s'$, no matter which path it has taken. Such pattern of exchanging repeats until the end of the directional coupler. If the lateral shift or the tunneling time were different for reflected and transmitted waves, then a pulse beam would split into multiple beams or multiple pulses. The physical nature of s and τ_g on energy storage and release, provides perfect synchronizations spatially and temporarily among all different reflection/transmission paths.

In conclusion, we have shown that the group delay and the dwell time in FTIR differ by the self-interference delay. This self-interference delay was obtained by calculating the energy in the overlap between the incident and reflected waves in front of the barrier. It is gratifying to see that this independently calculated delay is exactly equal to the difference between the previously published expressions for the group delay and the dwell time. The result thus confirms the physical reality of this self-interference delay and resolves the disparity between the two established definitions of tunneling time. The saturation of the group delay with barrier length (Hartman effect) is due to the saturation of the energy stored in the barrier and in the overlap between incident and reflected waves in front of the barrier. All of the three delay

times described here result from the interaction between forward and backward waves. Because of this, none of them can be used to calculate a propagation velocity for only a transmitted or reflected component. The results of this study have been published in Physical Review A [138].

CHAPTER V

Summary and Future work

5.1 Summary

This dissertation has explored the passive combining of mode-locked fiber lasers for scaling up energy, intensity, and pulse repetition rate.

With the dynamic model of simultaneous passive coherent beam combining and mode locking for an array of coupled fiber lasers, it is shown in agreement with experiment, that a pair of coherently combined fiber lasers will produce packets of mode-locked pulses whose repetition rate can be tuned by varying the length difference between the fibers. Because of beating, coherent beam combining performs a role of frequency combs and selects the array modes.

Unlike conventional solitons, dissipative solitons can also propagate in gain medium with normal dispersion, if there is saturable absorption and spectral filtering. Dissipative soliton fiber lasers in all normal dispersion cavity provides a more stable and robust solution from wave-breaking, carrying more energy per pulse. Higher peak intensity can be produced through dissipative solitons after pulse compression.

Dissipative solitons in a coherently beam combined fiber laser array with normal dispersion lead to a stable pulse train. The pulse packets have a modulation repetition rate related to the roundtrip time, while the pulses have a much faster repetition rate inside each packet. Commensurate fiber lengths degenerate the pulse packet modula-

tion, and a regular pulse train with uniform pulse intensities and high repetition rate is achieved.

As the kernel device in coherent beam combining, directional couplers put two parallel fiber cores within a few wavelengths with each other to let the power tunnel through. With a study on the FTIR tunneling process, we interpreted the physical meaning for both group delay and Goos-Hänchen shift. In the quasi-static condition, the tunneling process between two fiber cores is the storage and release of incident energy and it does not related to a “superluminal” velocity across the barrier. The lateral propagation is also shown to be causal.

5.2 Future Work

The major problem for passive device is that beam combining efficiency drops fast with the growth of the number of channels. Passive beam combining allows the oscillating laser power to select the mode with lowest loss by itself without artificial control. With an increasing number of channels, the density of modes reduces rapidly. As discussed in Chapter III, a 50:50 directional coupler generates a frequency comb when connecting two channels in different lengths. Only these array modes as the common modes for both channels are selected and almost all other modes vanish. For four-channel combining, we add one more layer of frequency comb on the discrete spectrum already filtered with frequency combs. If the number of channels is even higher, such as 8 or 16, the mode density will be so low that there may not be enough array modes left no matter how broad the gain bandwidth is. Then some non-array-modes get selected as the optimized result with least loss from the interplay of saturable absorption and beam combining, breaking the regular shape of a pulse train. Moreover, the irregular pulse train with quasi-random pulse intensities and distributions undermines the signal synchronization among channels and lowers the combining efficiency.

To compensate the mode density problem from beam combining and generate an ideal pulse train for even incommensurate fiber lengths, probably we need to compensate the number of modes after each 50:50 directional coupler, i.e. the frequency comb. This is one possible direction for future work. After the frequency comb in each layer of coherent beam combining, we may want to temporarily reduce the pulse repetition rate by some means without losing power. It is equivalent to inserting more modes in the spectrum. Then we add the next layer of frequency comb and repeat the mode density compensation. If the mode density can be maintained above some level in the presence of a large number of channels, it may be possible to overcome the bottleneck to scale up the laser power with high efficiency, and generate a regular pulse train with high pulse energy and peak intensity.

APPENDIX

APPENDIX A

Numerical Methods

In this appendix, I list a typical mpi-f90 (Message Passing Interface Fortran 90) code I have used for parallelly computing the numerical solution of the mode locked fiber laser array. It was originally developed by Wu et al. in 2009 [44] aimed for cw operation in coherent beam combining. Then I added the saturable absorption part to this code for mode locking simulation. The basic idea is applying SSFM algorithm to solve the NLSE for each channel in the array (parallel at each calculation node) and then gather together to process some lumped elements of the array, such as the directional coupler, the saturable absorber and the partial mirror.

Since the code uses random number generator (RNG) and FFT, it is necessary to load modules including PGI (version 12.3 or up), OPENMPI (version 1.6.0 or up) and FFTW (version 3.3.2 or up) onto the calculation server to run correctly.

```

program BeamC2
use mpi
!!!!!!!!!!!!!!!!!!!!!!!!!!!!!!!!!!!!!!!!!!!!!!!!!!!!!!!!!!!!!!!!!!!!!!
! compile with Fortran 90 mpi !
! !
! % mpif90 -o exefile file.f90 -L$FFTW_LINK -lfftw3 -lacml !
! % mpirun -np #processors exefile !
! !
!!!!!!!!!!!!!!!!!!!!!!!!!!!!!!!!!!!!!!!!!!!!!!!!!!!!!!!!!!!!!!!!!!!!!!

implicit none
! MPI Constants
integer numprocs, ierr, master, myid, tag, comm
real*8 Cpu_start, Cpu_end, Cpu_total
real*8 Wall_start, Wall_end, Wall_total

! FFTW constants
integer*8 planf, planb
integer*8 FFTW_FORWARD, FFTW_BACKWARD
integer*8 FFTW_ESTIMATE, FFTW_MEASURE

! Common Constants
integer*4 M
integer*4 npts, dnpts
integer*4 rtstps, RT, countj
integer*4 mod_rt
real*8 c0, wvlngth
real*8 Psat
real*8 alpha
real*8 spodr
real*8 beta2, bcff
real*8 n1
real*8 kpl
real*8 dlmin, dlmax, dlordr
complex*16 i, iGammaN

! Specify the number of nodes needed in addition to the master node
data M/1/

! Variables
integer*4 flid(0:M,4)
integer*4 nstps
integer*4 k, kk, jrt, jstp
real*8 pi
real*8 L(0:M)
real*8 refl(0:M)
real*8 h, Twindow
real*8 effP
real*8 findmax

```

```

real*8 findmin
real*8 simpson, p_i, t_window
complex*16 g0(0:M)
complex*16 los, g, Gav, d_los, alpha_L
character*80 fmt, ganfmt
character*20 flestr(3)
common /simpson_cff/ p_i, t_window
real*8 Psat_L

! Set FFTW constants
data FFTW_FORWARD/-1/, FFTW_BACKWARD/1/
data FFTW_ESTIMATE/0/, FFTW_MEASURE/1/

! Set Common Constants
data master/0/
data npts/262144/ ! NOTE: npts has to be to the order of 2
data dnpts/1/
data rtstps/72/, RT/4000/
data mod_rt/200/
data c0/3.0D8/
data wvlength/1.545D-6/
data Psat/0.6D-3/
data alpha/5.8D-2/
data spodr/1.0D-14/
data beta2/-0.003D-24/, bcff/0.013D-24/
data n1/1.5D0/
data kpl/0.5D0/
data i/(0.0,1.0D0)/
data iGammaN/(0.0,0.003D0)/

! For the saturate absorber
data alpha_L/9.0D-1/
data Psat_L/3.3D-1/

! Common Vectors
real*8 omega(1:npts), omega2(1:npts), time(1:npts)
real*8 linphse(1:npts), gvdphse(1:npts), ttlphse(1:npts)
real*8 angl(1:npts)
complex*16 Ef(1:npts), Et(1:npts)
complex*16 losDp(1:npts)
complex*16 Ef_0(1:npts)

! Vectors used by master
real*8 EffP_buff(0:M)
real*8 ave(0:M), std(0:M), pwer(0:M,1:500)
real*8 angl_buff(1:(M+1)*npts)
complex*16 Gav_buff(0:M)
complex*16 Ef_buff(1:(M+1)*npts)
complex*16 Ef_out(1:(M+1)*npts)

```

```

! Set Variables
pi = dacos(-1.0)
L = (/8.083D0, 8.063D0/)
refl = (/0.2D0, 0.0/)
g0 = cmplx(2.67D0,0)
p_i = pi
write(fmt,*) '(,npts,E15.7)'
write(ganfmt,*) '(3E15.7)'

! Initialize MPI
comm = MPI_COMM_WORLD
call MPI_Init(ierr)
call MPI_Comm_rank(comm, myid, ierr)
call MPI_Comm_size(comm, numprocs, ierr)

! Initialize FFTW
call dfftw_plan_dft_1d(planf,npts,Et,Ef,FFTW_FORWARD,FFTW_ESTIMATE)
call dfftw_plan_dft_1d(planb,npts,Ef,Et,FFTW_BACKWARD,FFTW_ESTIMATE)

! Set ranks-dependent variables
if (myid.EQ.master) then
Twindow = findmax(L,M)*n1/c0*1
end if
h = L(myid)/rtstps
los = cmplx(-alpha/2*h/2.0,0.0)
call MPI_Bcast( Twindow, &
1, &
MPI_REAL8, &
master, &
comm, &
ierr)
t_window = Twindow

! Setup output file
if (myid.EQ.master) then
do k = 0,M
flid(k,:) = (/ (kk*10, kk=1,4) /) + k*100
write (flestr(1),'(A,I1,A)') 'time',k,'.txt'
write (flestr(2),'(A,I1,A)') 'freq',k,'.txt'
write (flestr(3),'(A,I1,A)') 'gain',k,'.txt'
write (flestr(4),'(A,I1,A)') 'angl',k,'.txt'
open (flid(k,1), FILE=flestr(1), STATUS='NEW')
open (flid(k,2), FILE=flestr(2), STATUS='NEW')
open (flid(k,3), FILE=flestr(3), STATUS='NEW')
open (flid(k,4), FILE=flestr(4), STATUS='NEW')
end do
open (330, FILE="time.txt", STATUS='NEW')
open (340, FILE="freq.txt", STATUS='NEW')

```



```

end if

! Measure Time & Initialize random number generator
Wall_start=MPI_Wtime()
call cpu_time(Cpu_start)

! Setup of propagation vectors (rank-dependent)
time = /(k-1-npts/2, k=1,npts)/)*Twindow/(npts-1)
omega = /(k-1,k=1,npts/2), &
(k-npts-1,k=npts/2+1,npts)/)*2*pi/Twindow
omega2 = omega*omega
linphse = omega*n1*h/2.0/c0
gvdphse = omega2*beta2/2.0*h/2.0
ttlphse = modulo(linphse + gvdphse + &
n1*2*pi/wvlngh*h/2.0, 2*pi)
losDp = cmplx(-omega2*bcff/2.0*h/2.0,0.0) + los

! Prepare for loop & output time and freq
call signedRNG(Ef_0, npts, spodr, myid)
Ef = Ef_0
g = g0(myid)
Gav = cmplx(0,0)

! Collected by master
call MPI_Gather( Ef, npts, MPI_DOUBLE_COMPLEX, &
Ef_buff, npts, MPI_DOUBLE_COMPLEX, &
master, comm, ierr)
if (myid.EQ.master) then
g = (0.0,0.0)
write(330,fmt) (time(kk)*1e9, kk=1,npts,dnpts)
write(340,fmt) (omega(kk)/2/pi/1e9, kk=1,npts,dnpts)
do k=0,M
Ef = Ef_buff(k*npts+1:(k+1)*npts)
call dfftw_execute_dft(planb, Ef, Et)
Et = Et/npts
effP = simpson(Et,npts,1)
angl = modulo(ATAN2(imag(Ef),real(Ef)),2*pi)
write(flid(k,1),fmt) (cdabs(Et(kk))**2, kk=1,npts,dnpts)
write(flid(k,2),fmt) (cdabs(Ef(kk))**2, kk=1,npts,dnpts)
write(flid(k,3),ganfmt) L(k), refl(k), real(2*g/h)
write(flid(k,4),fmt) (angl(kk), kk=1,npts,dnpts)
end do
end if

! Main Loop !
do 66 jrt=1,RT

! Random number as ASE
call signedRNG(Ef_0, npts, spodr, myid)

```

```

Ef = Ef + Ef_0
do jstp = 1,rtstps

! Calculate effective power
call dfftw_execute_dft(planb, Ef, Et)
Et = Et/npts
effP = simpson(Et,npts,1)
g = g0(myid)/2/(1+effP/Psat/Twindow)*h

! freq domain
Ef = Ef*cdexp(g/2 + losDp + cplx(0,ttlphse))

! time domain
call dfftw_execute_dft(planb, Ef, Et)
Et = Et/npts
Et = Et*cdexp(iGammaN*cdabs(Et)**2*h)

! freq domain
call dfftw_execute_dft(planf, Et, Ef)
Ef = Ef*cdexp(g/2 + losDp + cplx(0,ttlphse))

! average gain and puer
Gav = Gav + g
end do
Gav = Gav*2/rtstps/h
call dfftw_execute_dft(planb, Ef, Et)
Et = Et/npts
effP = simpson(Et,npts,1)
angl = modulo(ATAN2(imag(Ef),real(Ef)),2*pi)

! Collected by master
call MPI_Gather( Gav, 1, MPI_DOUBLE_COMPLEX, &
Gav_buff, 1, MPI_DOUBLE_COMPLEX, &
master, comm, ierr)
call MPI_Gather( Ef, npts, MPI_DOUBLE_COMPLEX, &
Ef_buff, npts, MPI_DOUBLE_COMPLEX, &
master, comm, ierr)
call MPI_Gather( EffP, 1, MPI_REAL8, &
EffP_buff, 1, MPI_REAL8, &
master, comm, ierr)
call MPI_Gather( angl, npts, MPI_REAL8, &
angl_buff, npts, MPI_REAL8, &
master, comm, ierr)

! Through 50:50 coupler
if (myid.EQ.master) then

! coupler
Ef_out(1:npts) = &

```

```

sqrt(kpl)*Ef_buff(1:npts) &
-i*sqrt(1-kpl)*Ef_buff(npts+1:2*npts)
Ef_out(npts+1:2*npts) = &
-i*sqrt(1-kpl)*Ef_buff(1:npts)+ &
sqrt(kpl)*Ef_buff(npts+1:2*npts)

!saturable absorber
call dfftw_execute_dft(planb, Ef_out(1:npts), Et)
Et = Et/npts
do countj = 1,npts
Et(countj) = Et(countj)*cdexp(-alpha_L/(1+(cdabs(Et(countj)))**2 &
+cdabs(Et(modulo(countj+1,npts)))**2+cdabs(Et(modulo(countj+2,npts))
)**2&
+cdabs(Et(modulo(countj+3,npts)))**2)/4/Psat_L))
end do
call dfftw_execute_dft(planf, Et, Ef_out(1:npts))

! store feedback in Ef_buff
SELECT CASE(refl(0).GT.refl(1))
CASE(.True.)
Ef_buff = refl(0)/sqrt(2.0)* &
(/Ef_out(1:npts), Ef_out(1:npts)/)
CASE(.False.)
Ef_buff = refl(1)/sqrt(2.0)* &
(/Ef_out(npts+1:2*npts), Ef_out(npts+1:2*npts)/)
END SELECT

! Output by master
if (modulo(jrt,mod_rt).EQ.0) then
do k = 0,M
Gav = Gav_buff(k)
Ef = Ef_out(k*npts+1:(k+1)*npts)*dsqrt(1-refl(k)**2)
call dfftw_execute_dft(planb, Ef, Et)
Et = Et/npts
effP = simpson(Et,npts,1)
angl = angl_buff(k*npts+1:(k+1)*npts)
write(flid(k,1),fmt)(cdabs(Et(kk))**2, kk=1,npts,dnpts)
write(flid(k,2),fmt)(cdabs(Ef(kk))**2, kk=1,npts,dnpts)
write(flid(k,3),ganfmt) effP_buff(k)/Twindow, &
effP/Twindow, real(Gav)
write(flid(k,4),fmt) (angl(kk),kk=1,npts,dnpts)
write(*,*) jrt, k, effP_buff(k)/Twindow, &
effP/Twindow, real(Gav)
end do
end if
end if

! Feedback reflected wave
Gav = cplx(0,0)

```

```

call MPI_Scatter( Ef_buff, npts, MPI_DOUBLE_COMPLEX, &
Ef, npts, MPI_DOUBLE_COMPLEX, &
master, comm, ierr)

! End of Main Loop
66 enddo

! Calculate elapsed time
Wall_end=MPI_Wtime()
call cpu_time(Cpu_end)
Wall_total = Wall_end - Wall_start
call MPI_Reduce( Cpu_end-Cpu_Start, &
Cpu_total, &
1, &
MPI_REAL8, &
MPI_SUM, &
master, &
comm, &
ierr)

! Record CPU time and Wall time
! Ideally CPU time is (M+1) times of Wall time
if (myid.EQ.master) then
write(*,*) "Cpu_time= ", Cpu_total, "sec."
write(*,*) "Wall_time= ", Wall_total, "sec."
end if

! finalize FFTW
call dfftw_destroy_plan(planf)
call dfftw_destroy_plan(planb)

! finalize MPI
call MPI_FINALIZE(ierr)
end program BeamC2

```

BIBLIOGRAPHY

BIBLIOGRAPHY

- [1] C. J. Koester and E. Snitzer. Amplification in a fiber laser. *Appl. Opt.*, 3:1182–1186, 1964.
- [2] G. P. Agrawal. *Nonlinear Fiber Optics*. Academic Press, San Diego, CA, 2001.
- [3] Rüdiger Paschotta. *Field Guide to Laser Pulse Generation*. SPIE Press, Bellingham, WA, 2008.
- [4] V. Dominic, S. MacCormack, R. Waarts, S. Sanders, S. Bicknese, R. Dohle, E. Wolak, P.S. Yeh, and E. Zucker. 110w fibre laser. *Electron. Lett.*, 35:1158–1160, 1999.
- [5] J. Nilsson, J. K. Sahu, Y. Jeong, W. A. Clarkson, R. Selvas, A. B. Grudinin, and S. Alam. High power fiber lasers: new development. *Advances in Fiber Devices, Proceedings of SPIE*, 4974:50–59, 2003.
- [6] Y. Jeong, J. Sahu, D. Payne, and J. Nilsson. Ytterbium-doped large-core fiber laser with 1.36 kw continuous-wave output power. *Opt. Express*, 12:6088–6092, 2004.
- [7] F. Röser, J. Rothhard, B. Ortac, A. Liem, O. Schmidt, T. Schreiber, J. Limpert, and A. Tünnermann. 131 w 220 fs fiber laser system. *Opt. Lett.*, 30:2754–2756, 2005.
- [8] D. J. Richardson, J. Nilsson, and W. A. Clarkson. High power fiber lasers: current status and future perspectives. *J. Opt. Soc. Am. B*, 27:B63–B92, 2010.
- [9] Ursula Keller. Recent developments in compact ultrafast lasers. *Nature*, 424:831–838, 2003.
- [10] A. Tünnermann. High-power cw fiber lasers present and future. *Laser Technik Journal*, 2:54–56, 2005.
- [11] G.A. Mourou and T. Tajima. More intense, shorter pulses. *Science*, 331:41–42, 2011.
- [12] Robert W. Boyd. *Nonlinear Optics*. Academic Press, 2008.
- [13] V. E. Zakharov and A. B. Shabat. Exact theory of two-dimensional self-focusing and one-dimensional self-modulation of waves in nonlinear media. *Sov. Phys. JETP*, 34:62, 1972.

- [14] L. F. Mollenauer, R. H. Stolen, and J. P. Gordon. Experimental observation of picosecond pulse narrowing and solitons in optical fibers. *Phys. Rev. Lett.*, 45:1095–1098, 1980.
- [15] V. N. Serkin and A. Hasegawa. Novel soliton solutions of the nonlinear schrödinger equation model. *Phys. Rev. Lett.*, 85:4502–4505, 2000.
- [16] N. Akhmediev and A. Ankiewicz, editors. *Dissipative Solitons*. Springer, 2005.
- [17] N. Akhmediev and A. Ankiewicz, editors. *Dissipative Solitons: From Optics to Biology and Medicine*. Spring, 2008.
- [18] W. Chang, A. Ankiewicz, J. M. Soto-Crespo, and N. Akhmediev. Dissipative soliton resonances. *Phys. Rev. A*, 78:023830, 2008.
- [19] Ph. Grelu and N. Akhmediev. Dissipative solitons for mode-locked lasers. *Nat. Photon.*, 6:84–92, 2012.
- [20] M. E. Fermann, V. I. Kruglov, B. C. Thomsen, J. M. Dudley, and J. D. Harvey. Self-similar propagation and amplification of parabolic pulses in optical fibers. *Phys. Rev. Lett.*, 84:6010–6013, 2000.
- [21] J. M. Dudley, C. Finot, D. J. Richardson, and G. Millot. Self-similarity in ultrafast nonlinear optics. *Nat. Phys.*, 3:597–602, 2007.
- [22] F. . Ilday, J. R. Buckley, W. G. Clark, and F. W. Wise. Self-similar evolution of parabolic pulses in a laser. *Phys. Rev. Lett.*, 92:213902, 2004.
- [23] Christophe Finot, John M. Dudley, Bertrand Kibler, David J. Richardson, and Guy Millot. Optical parabolic pulse generation and applications. *IEEE J. Quantum Electronics*, 45:1482–1489, 2009.
- [24] R. H. Stolen, E. P. Ippen, and A. R. Tynes. Raman oscillation in glass optical waveguide. *Appl. Phys. Lett.*, 20:62–64, 1972.
- [25] H. A. Haus and M. Nakazawa. Theory of the fiber raman soliton laser. *J. Opt. Soc. Am. B*, 4:652–660, 1987.
- [26] C. A. Codemard, P. Dupriez, Y. Jeong, J. K. Sahu, M. Ibsen, and J. Nilsson. High-power continuous-wave cladding-pumped raman fiber laser. *Opt. Lett.*, 31:2290–2292, 2006.
- [27] D. Grischkowsky and A. C. Balant. Optical pulse compression based on enhanced frequency chirping. *Appl. Phys. Lett.*, 41:1–3, 1982.
- [28] W. J. Tomlinson, R. H. Stolen, and A. M. Johnson. Optical wave breaking of pulses in nonlinear optical fibers. *Opt. Lett*, 10:457–459, 1985.

- [29] H. E. Lassen, F. Mengel, B. Tromborg, N. C. Albertsen, and P. L. Christianse. Evolution of chirped pulses in nonlinear single-mode fibers. *Opt. Lett.*, 10:34–36, 1985.
- [30] W. J. Tomlinson, R. H. Stolen, and C. V. Shank. Compression of optical pulses chirped by self-phase modulation in fibers. *J. Opt. Soc. Am. B*, 1:139–149, 1984.
- [31] R. Y. Chiao and C. H. Townes. Stimulated brillouin scattering and coherent generation of intense hypersonic waves. *Phys. Rev. Lett.*, 12:592–595, 1964.
- [32] E.P. Ippen and R.H. Stolen. Stimulated brillouin scattering in optical fibers. *Appl. Phys. Lett.*, 21:539–541, 1972.
- [33] Y. Koyamada, S. Sato, S. Nakamura, H. Sotobayashi, and W. Chujo. Simulating and designing brillouin gain spectrum in single mode fibers. *J. Lightwave Technology*, 2:631–639, 2004.
- [34] Benjamin Ward and Justin Spring. Finite element analysis of brillouin gain in sbs-suppressing optical fibers with non-uniform acoustic velocity profiles. *Opt. Express*, 17:15685–15699, 2009.
- [35] Justin Spring and Benjamin Ward. Brillouin gain suppression in photonic crystal fibers with random acoustically microstructured cores. *Opt. Lett.*, 35:31–33, 2010.
- [36] Y. Imai and N. Shimada. Dependence of stimulated brillouin scattering on temperature distribution in polarization-maintaining fibers. *IEEE Photon. Technol. Lett.*, 5:1335–1337, 1993.
- [37] J. Hansryd, F. Dross, M. Westlund, P. A. Andrekson, and S. N. Knudsen. Increase of the sbs threshold in a short highly nonlinear fiber by applying a temperature distribution. *J. Lightwave Technology*, 19:1961–1967, 2001.
- [38] S. J. Augst, T. Y. Fan, and A. Sanchez. Coherent beam combining and phase noise measurements of ytterbium fiber amplifiers. *Opt. Lett.*, 29:474–476, 2004.
- [39] H. Bruesselbach, D. C. Jones, M. S. Mangir, M. Minden, and J. L. Rogers. Self-organized coherence in fiber laser arrays. *Opt. Lett.*, 30:1339–1341, 2005.
- [40] W. Ray, J. L. Rogers, and K. Wiesenfeld. Coherence between two coupled lasers from a dynamics perspective. *Opt. Express*, 17:9357–9368, 2009.
- [41] V. Roy, M. Piche, F. Babin, and G. W. Schinn. Nonlinear wave mixing in a multilongitudinal-mode erbium-doped fiber laser. *Opt. Express*, 13:6791–6797, 2005.
- [42] D. Sabourdy, V. Kermene, A. Desfarges-Berthelemot, L. Lefort, A. Barthelemy, P. Even, and D. Pureur. Efficient coherent combining of widely tunable fiber lasers. *Opt. Express*, 11:87–97, 2003.

- [43] T. B. Simpson, F. Doft, P. R. Peterson, and A. Gavrielides. Coherent combining of spectrally broadened fiber lasers. *Opt. Express*, 15:11731–11740, 2007.
- [44] T. Wu, W. Chang, A. Galvanauskas, and H. G. Winful. Model for passive coherent beam combining in fiber laser arrays. *Opt. Express*, 17:19509–19518, 2009.
- [45] T. Wu, W. Chang, A. Galvanauskas, and H. G. Winful. Dynamical, bidirectional model for coherent beam combining in passive fiber laser arrays. *Opt. Express*, 18:25873–25886, 2010.
- [46] W. Chang, T. Wu, H. G. Winful, and A. Galvanauskas. Array size scalability of passively coherently phased fiber laser arrays. *Opt. Express*, 18:9634–9642, 2010.
- [47] Donna Strickland and Gerard Mourou. Compression of amplified chirped optical pulses. *Opt. Comm.*, 56:219–221, 1985.
- [48] Almantas Galvanauskas. Mode-scalable fiber-based chirped pulse amplification systems. *IEEE J. Sel. Top. Quantum Electron.*, 7:504–516, 2001.
- [49] J. Limpert, F. Röser, T. Schreiber, and A. Tünnermann. High-power ultrafast fiber laser systems. *IEEE J. Sel. Top. Quantum Electron.*, 12:233–244, 2006.
- [50] Amos Martinez and Shinji Yamashita. Multi-gigahertz repetition rate passively modelocked fiber lasers using carbon nanotubes. *Opt. Express*, 19:6155–6163, 2011.
- [51] Shiquan Yang, E.A. Ponomarev, and Xiaoyi Bao. 80-ghz pulse generation from a repetition-rate-doubled fm mode-locking fiber laser. *IEEE Photon. Technol. Lett.*, 17:300–302, 2005.
- [52] A. E. Siegman. *Lasers*. University Science Books, 1986.
- [53] A. B. Grudinin, D. J. Richardson, and D. N. Payne. Passive harmonic mode-locking of a fibre soliton ring laser. *Electron. Lett.*, 29:1860–1861, 1993.
- [54] A. B. Grudinin and S. Gray. Passive harmonic mode locking in soliton fiber lasers. *J. Opt. Soc. Am. B*, 14:144–154, 1997.
- [55] Chiming Wu and N.K. Dutta. High-repetition-rate optical pulse generation using a rational harmonic mode-locked fiber laser. *IEEE J. Quantum Electron.*, 36:145–150, 2002.
- [56] Mable P. Fok, W. W. Tang, and Chester Shu. Higher order repetition rate multiplication for multiwavelength pulsed source. *IEEE Photon. Technol. Lett.*, 18:466–468, 2006.

- [57] K. Yiannopoulos, K. Vyrsoinos, D. Tsiokos, E. Kehayas, N. Pleros, G. Theophilopoulos, T. Houbavlis, G. Guekos, and H. Avramopoulos. Pulse repetition frequency multiplication with spectral selection in fabry-pérot filters. *IEEE J. Quantum Electron.*, 40:157–165, 2004.
- [58] S. Gee, F. Quinlan, S. Ozharar, and P. J. Delfyett. Simultaneous optical comb frequency stabilization and super-mode noise suppression of harmonically mode-locked semiconductor ring laser using an intracavity etalon. *IEEE Photon. Technol. Lett.*, 17:199–201, 2005.
- [59] P. Petropoulos, M. Ibsen, M. N. Zervas, and D. J. Richardson. Generation of a 40-ghz pulse stream by pulse multiplication with a sampled fiber bragg grating. *Opt. Lett.*, 25:521–523, 2000.
- [60] R. Slavík and S. LaRochelle. Design of 10-to-40 ghz and higher pulse-rate multiplication by means of coupled fabry-perot resonators. *Opt. Comm.*, 247:307–312, 2005.
- [61] D. E. Leaird, S. Shen, A. M. Weiner, A. Sugita, M. Ishii S. Kamei, and K. Okamoto. Generation of high-repetition-rate wdm pulse trains from an arrayed-waveguide grating. *IEEE Photon. J.*, 13:221–223, 2001.
- [62] J. Lhermite, D. Sabourdy, A. Desfarges-Berthelemot, V. Kermene, and A. Barthelemy. Tunable high-repetition-rate fiber laser for the generation of pulse trains and packets. *Opt. Lett.*, 32:1734–1736, 2007.
- [63] Chao Zhang, Wei zung Chang, Almantas Galvanauskas, and Herbert G. Winful. Simultaneous passive coherent combining and mode locking in fiber laser arrays. In *CLEO:2011 - Laser Applications to Photonic Applications*, page JWA28. Optical Society of America, 2011.
- [64] C. Zhang, W. Chang, A. Galvanauskas, and H. G. Winful. Simultaneous passive coherent beam combining and mode locking of fiber laser arrays. *Opt. Express*, 20:16245–16257, 2012.
- [65] D. Anderson, M. Desaix, M. Lisak, and M. L. Quiroga-Teixeiro. Wave breaking in nonlinear-optical fibers. *J. Opt. Soc. Am. B*, 9:1358–1361, 1992.
- [66] Nikolai B. Chichkov, Katharina Hausmann, Dieter Wandt, Uwe Morgner, Jörg Neumann, and Dietmar Kracht. High-power dissipative solitons from an all-normal dispersion erbium fiber oscillator. *Opt. Lett.*, 35:2807–2809, 2010.
- [67] B. Wang and A. Sanchez. All-fiber passive coherent combining of fiber lasers. *Opt. Eng.*, 50:111606, 2011.
- [68] A. Shirakawa, T. Saitou, T. Sekiguchi, , and K. Ueda. Coherent addition of fiber lasers by use of a fiber coupler. *Opt. Express*, 10:1167–1172, 2002.

- [69] D. Sabourdy, A. Desfarges-Berthelemot, V. Kermene, and A. Barthelemy. Coherent combining of q-switched fiber lasers. *Electron. Lett.*, 40:1254–1255, 2004.
- [70] M. E. Fermann and I. Hartl. Ultrafast fiber laser technology. *IEEE J. Sel. Top. Quantum Electron.*, 15:191–206, 2009.
- [71] T. Y. Fan. Laser beam combining for high-power, high-radiance sources. *IEEE J. Sel. Top. Quantum Electron.*, 11:567–577, 2005.
- [72] S. J. Augst, J. K. Ranka, T. Y. Fan, and A. Sanchez. Beam combining of ytterbium fiber amplifiers. *J. Opt. Soc. Am. B*, 24:1707–1715, 2007.
- [73] J. Q. Cao, J. Hou, Q. S. Lu, and X. J. Xu. Numerical research on self-organized coherent fiber laser arrays with circulating field theory. *J. Opt. Soc. Am. B*, 25:1187–1192, 2008.
- [74] S. P. Chen, Y. G. Li, K. C. Lu, and S. H. Zhou. Efficient coherent combining of tunable erbium-doped fibre ring lasers. *J. Opt. A*, 9:642–648, 2007.
- [75] J. L. Rogers, S. Peles, and K. Wiesenfeld. Model for high-gain fiber laser arrays. *IEEE J. Quantum Electron.*, 41:767–773, 2005.
- [76] T. M. Shay, V. Benham, J. T. Baker, B. Ward, A. D. Sanchez, M. A. Culpepper, D. Pilkington, J. Spring, D. J. Nelson, and C. A. Lu. First experimental demonstration of self-synchronous phase locking of an optical array. *Opt. Express*, 14:12015–12021, 2006.
- [77] E. Desurvire. Analysis of erbium-doped fiber amplifiers pumped in the $i-4(15/2)-i-4(13/2)$ band. *IEEE Photon. Technol. Lett.*, 1:293–296, 1989.
- [78] C. R. Giles, E. Desurvire, and J. R. Simpson. Transient gain and cross talk in erbium-doped fiber amplifiers. *Opt. Lett.*, 14:880–882, 1989.
- [79] L. E. Hargrove, R. L. Fork, and M. A. Pollack. Locking of laser modes induced by synchronous intracavity modulation. *Appl. Phys. Lett.*, 5:4, 1964.
- [80] Herman A. Haus. Theory of mode locking with a fast saturable absorber. *J. Appl. Phys.*, 46:3049–3058, 1975.
- [81] H. A. Haus. Mode-locking of lasers. *IEEE J. Sel. Top. Quantum Electron.*, 6:1173, 2000.
- [82] H. A. Haus, J. G. Fujimoto, and E. P. Ippen. Structures of additive pulse mode locking. *J. Opt. Soc. Am. B*, 8:2068–2076, 1991.
- [83] E. P. Ippen. Principles of passive mode locking. *Appl. Phys. B*, 58:159, 1994.
- [84] W. E. Lamb Jr. Theory of an optical laser. *Phys. Rev.*, 134:A1429, 1964.

- [85] F. Krausz and T. Brabec. Passive mode locking in standing-wave laser resonators. *Opt. Lett.*, 18:888, 1993.
- [86] O. E. Martínez and R. L. Fork. Theory of passively mode-locked lasers including self-phase modulation and group-velocity dispersion. *Opt. Lett.*, 9:156, 1984.
- [87] G. H. C. New. Pulse evolution in mode-locked quasi-continuous lasers. *IEEE J. Quantum Electron.*, 10:115, 1974.
- [88] B. K. Garside and T. K. Lim. Laser mode locking using saturable absorbers. *J. Appl. Phys.*, 44:2335, 1973.
- [89] Donnell T. Walton and Herbert G. Winful. Passive mode locking with an active nonlinear directional coupler: Positive group-velocity dispersion. *Opt. Lett.*, 18:720–722, 1993.
- [90] Herbert G. Winful and Donnell T. Walton. Passive mode locking through nonlinear coupling in a dual-core fiber laser. *Opt. Lett.*, 17:1688–1690, 1992.
- [91] R. Paschotta. Passive mode locking with slow saturable absorbers. *Appl. Phys. B*, 73:653, 2001.
- [92] N. Akhmediev, J. M. Soto-Crespo, and Ph. Grelu. Roadmap to ultra-short record high-energy pulses out of laser oscillators. *Phys. Lett. A*, 372:3124–3128, 2008.
- [93] B. Oktem, C. Igdr, and F. . Ilday. Soliton-similariton fibre laser. *Nat. Photon.*, 4:307–311, 2010.
- [94] W. H. Renninger, A. Chong, and F. W. Wise. Dissipative solitons in normal-dispersion fiber lasers. *Phys. Rev. A*, 77:023814, 2008.
- [95] X. Liu. Mechanism of high-energy pulse generation without wave breaking in mode-locked fiber lasers. *Phys. Rev. A*, 82:053808, 2010.
- [96] R. Wang, Y. Dai, L. Yan, J. Wu, K. Xu, Y. Li, and J. Lin. Dissipative soliton in actively mode-locked fiber laser. *Opt. Express*, 20:6406–6411, 2012.
- [97] W. H. Renninger, A. Chong, and F. W. Wise. Pulse shaping and evolution in normal-dispersion mode-locked fiber lasers. *IEEE J. Sel. Top. Quant. Electron.*, 18:389–398, 2012.
- [98] A. Chong, W. H. Renninger, and F. W. Wise. All-normal-dispersion femtosecond fiber laser with pulse energy above 20 nj. *Opt. Lett.*, 32:2408–2410, 2007.
- [99] A. Chong, W. H. Renninger, and F. W. Wise. Properties of normal-dispersion femtosecond fiber lasers. *J. Opt. Soc. Am. B*, 25:140–148, 2008.

- [100] Z. X. Zhang and G. X. Dai. All-normal-dispersion dissipative soliton ytterbium fiber laser without dispersion compensation and additional filter. *IEEE Photon. J.*, 3:1023–1029, 2011.
- [101] Andy Chong, Joel Buckley, Will Renninger, and Frank W. Wise. All-normal-dispersion femtosecond fiber laser. *Opt. Express*, 14:10095–10100, 2006.
- [102] Akira Hasegawa and Frederick Tappert. Transmission of stationary nonlinear optical pulses in dispersive dielectric fibers. i. anomalous dispersion. *Appl. Phys. Lett.*, 23:142–144, 1973.
- [103] Akira Hasegawa and Frederick Tappert. Transmission of stationary nonlinear optical pulses in dispersive dielectric fibers. ii. normal dispersion. *Appl. Phys. Lett.*, 23:171–172, 1973.
- [104] Govind P. Agrawal, P. L. Baldeck, and R. R. Alfano. Optical wave breaking and pulse compression due to crossphase modulation in optical fibers. *Opt. Lett.*, 14:137, 1989.
- [105] Frank W. Wise, Andy Chong, and William H. Renninger. High-energy femtosecond fiber lasers based on pulse propagation at normal dispersion. *Laser Photon. Rev.*, 2:58–73, 2008.
- [106] W. H. Renninger, A. Chong, and F. W. Wise. Self-similar pulse in an all-normal-dispersion laser. *Phys. Rev. A*, 82:021805, 2010.
- [107] X. Wu, D. Y. Tang, H. Zhang, and L. M. Zhao. Dissipative soliton resonance in an all-normal-dispersion erbium-doped fiber laser. *Opt. Express*, 17(7):5580–5584, Mar 2009.
- [108] G. Q. Chang, H. G. Winful, A. Galvanauskas, and T. B. Norris. Self-similar parabolic beam generation and propagation. *Phys. Rev. E*, 72:016609, 2005.
- [109] Igor S. Aranson and Lorenz Kramer. The world of the complex ginzburg-landau equation. *Rev. Mod. Phys.*, 74:99–143, 2002.
- [110] A.M. Dunlop, W.J. Firth, and E.M. Wright. Time-domain master equation for pulse evolution and laser mode-locking. *Optical and Quantum Electronics*, 32:1131–1146, 2000.
- [111] Chengying Bao, Xiaosheng Xiao, and Changxi Yang. Pulse shaping effects of fast saturable absorbers in dissipative soliton fiber lasers. *Opt. Comm.*, 308:20–25, 2013.
- [112] J. Nathan Kutz, Brandon C. Collings, Keren Bergman, Sergio Tsuda, Steven T. Cundiff, Wayne H. Knox, Philip Holmes, and Michael Weinstein. Mode-locking pulse dynamics in a fiber laser with a saturable bragg reflector. *J. Opt. Soc. Am. B*, 14:2681–2690, 1997.

- [113] J. M. Soto-Crespo, N. N. Akhmediev, and V. V. Afanasjev. Stability of the pulselike solutions of the quintic complex ginzburg-landau equation. *J. Opt. Soc. Am. B*, 13:1439–1449, 1996.
- [114] J. Ye, H. Schnatz, and L. W. Hollberg. Optical frequency combs: from frequency metrology to optical phase control. *IEEE J. Sel. Top. Quantum Electron.*, 9:1041–1058, 2003.
- [115] Steven T. Cundiff and Jun Ye. Colloquium: Femtosecond optical frequency combs. *Rev. Mod. Phys.*, 75:325–342, 2003.
- [116] Theodore Sizer II. Increase in laser repetition rate by spectral selection. *IEEE J. Quantum Electron.*, 25:97–103, 1989.
- [117] R. Holzwarth, M. Zimmermann, T. Udem, and T. W. Hansch. Optical clockworks and the measurement of laser frequencies with a mode-locked frequency comb. *IEEE J. Quantum Electron.*, 12:1493–1501, 2001.
- [118] H. A. Haus, W. P. Huang, S. Sawakami, and N. A. Whitaker. Coupled-mode theory of optical waveguide. *J. Lightwave Technology*, LT-5:16–23, 1987.
- [119] R.Y. Chiao, P.G. Kwiat, and A.M. Steinberg. Analogies between electron and photon tunneling: A proposed experiment to measure photon tunneling times. *Physica B*, 175:257, 1991.
- [120] V. L Maslennikov, V. A. Sychugov, A. V. Tishchenko, and B. A. Usievich. Light generation in a system of two coupled waveguides. *Sov. J. Quantum Electron.*, 22:1041–1044, 1992.
- [121] N. M. Lyndin, V. A. Sychugov, and B. A. Usievich. Spectral selectivity of radiation- and tunnel-coupled waveguide structures. *Tech. Phys.*, 1997:175–180, 1997.
- [122] I. O. Zolotovskii and D. I. Sementsov. Velocity of the pulse envelope in tunnel-coupled optical waveguides with strongly differing parameters. *Optics and Spectroscopy*, 101:114–117, 2006.
- [123] V. V. Malov and E. V. Lyalina. The theory of nonstationary processes in optical tunnel-coupled ring waveguide resonators. *Laser Physics*, 4:178–190, 1994.
- [124] D D Gusovskii, Evgenii M Dianov, A A Maier, V B Neustruev, E I Shklovskii, and Ivan A Shcherbakov. Nonlinear light transfer in tunnel-coupled optical waveguides. *Sov. J. Quantum Electron.*, 15:1523–1526, 1985.
- [125] P. Eckle, A. N. Pfeiffer, C. Cirelli, A. Staudte, R. Drner, H. G. Muller, M. Bttiker, and U. Keller. Attosecond ionization and tunneling delay time measurements in helium. *Science*, 322:1525, 2008.

- [126] Mathew Tomes, Kerry J. Vahala, and Tal Carmon. Direct imaging of tunneling from a potential well. *Opt. Express*, 17:19160–19165, 2009.
- [127] F. Goos and H. Hänchen. Ein neuer und fundamentaler versuch zur total reflexion. *Ann. Physik*, 1:333–346, 1947.
- [128] R. Landauer. Light faster than light. *Nature*, 365:692–693, 1993.
- [129] R. Landauer and Th. Martin. Barrier interaction time in tunneling. *Rev. Mod. Phys.*, 66:217–228, 1994.
- [130] E. H. Hauge and J. A. Støvneng. Tunneling times: a critical review. *Rev. Mod. Phys.*, 61:917, 1989.
- [131] Aephraim M. Steinberg. How much time does a tunneling particle spend in the barrier region? *Phys. Rev. Lett.*, 74:2405–2409, 1995.
- [132] Aephraim M. Steinberg and Raymond Y. Chiao. Subfemtosecond determination of transmission delay times for a dielectric mirror (photonic band gap) as a function of the angle of incidence. *Phys. Rev. A*, 51:3525–3528, 1995.
- [133] A. A. Stahlhofen and G. Nimtz. Evanescent modes are virtual photons. *Europhys. Lett.*, 76:189–195, 2006.
- [134] H. G. Winful. Energy storage in superluminal barrier tunneling: Origin of the hartman effect. *Opt. Express*, 10:1491–1496, 2002.
- [135] H. G. Winful. Nature of superluminal” barrier tunneling. *Phys. Rev. Lett.*, 90:023901, 2003.
- [136] H. G. Winful. Group delay, stored energy, and the tunneling of evanescent electromagnetic waves. *Phys. Rev. E*, 68:016615, 2003.
- [137] H. G. Winful. Tunneling time, the hartman effect, and superluminality: A proposed resolution of an old paradox. *Phys. Rep.*, 436:1, 2006.
- [138] H. G. Winful and C. Zhang. Tunneling delay time in frustrated total internal reflection. *Phys. Rev. A*, 79:023826, 2009.
- [139] T. E. Hartman. Tunneling of a wave packet. *J. Appl. Phys.*, 33:3427, 1962.
- [140] H. G. Winful. Delay time and the hartman effect in quantum tunneling. *Phys. Rev. Lett.*, 91:260401, 2003.
- [141] J.C. Martinez and E. Polatdemir. Origin of the hartman effect. *Phys. Lett. A*, 351:31–36, 2006.
- [142] H. G. Winful. The meaning of group delay in barrier tunnelling: a re-examination of superluminal group velocities. *New J. Phys.*, 8:101, 2006.

- [143] H. G. Winful, M. Ngom, and N. M. Litchinitser. Relation between quantum tunneling times for relativistic particles. *Phys. Rev. A*, 70:052112, 2004.
- [144] H. G. Winful. Physical mechanism for apparent superluminality in barrier tunneling. *IEEE J. Sel. Top. Quantum Electron.*, 9:17, 2003.
- [145] Amnon Yariv. Coupled-mode theory for guided-wave optics. *IEEE J. Quantum Electron.*, QE-9:919–933, 1973.
- [146] Amnon Yariv and Pochi Yeh. *Optical Waves in Crystals: Propagation and Control of Laser Radiation*. Wiley-Interscience, 2002.
- [147] Frederique de Fornel. *Evanescent Waves : From Newtonian Optics to Atomic Optics*. Springer, 2001.
- [148] A. M. Steinberg and R. Y. Chiao. Tunneling delay times in one and two dimensions. *Phys. Rev. A*, 49:3283–3295, 1994.
- [149] Jie-Long Shi, Chun-Fang Li, and Qi Wang. Theory of the goos-hänchen displacement in total internal reflection. *Intern. J. Mod. Phys. B*, 21:2777, 2007.
- [150] C.-F. Li and Q. Wang. Duration of tunneling photons in a frustrated-total-internal-reflection structure. *J. Opt. Soc. Am. B*, 18:1174–1179, 2001.
- [151] C.-F. Li. Comment on photonic tunneling time in frustrated total internal reflection. *Phys. Rev. A*, 65:066101, 2002.
- [152] J. L. Agudin. Time delay of scattering processes. *Phys. Rev.*, 171:1385–1387, 1968.
- [153] A. Ghatak and S. Banerjee. Temporal delay of a pulse undergoing frustrated total internal reflection. *Appl. Opt.*, 28:1960, 1989.
- [154] B. Lee and W. Lee. Tm-polarized photon tunneling phase time in a frustrated-total-internal-reflection structure. *J. Opt. Soc. Am. B*, 17:777, 1997.
- [155] K. J. Resch, J. S. Lundeen, and A. M. Steinberg. Total reflection does not occur in negative time. *IEEE J. Quantum Electron.*, 37:794, 2001.
- [156] R. H. Renard. Total reflection: new evaluation of goos-hänchen shift. *J. Opt. Soc. Am.*, 54:1190, 1964.
- [157] K. Yasumoto and Y. Oishi. A new evaluation of the gooshänchen shift and associated time delay. *J. Appl. Phys.*, 54:2170, 1983.
- [158] E.O. Schultz-DuBois. Energy transport velocity of electromagnetic propagation in dispersive media. *Proceedings of the IEEE*, 57:1748–1757, 1969.
- [159] S. Doiron, A. Hache, and H. G. Winful. Direct space-time observation of pulse tunneling in an electromagnetic band gap. *Phys. Rev. A*, 76:023823, 2007.

- [160] G. D'Aguanno, N. Mattiucci, M. Scalora, M. J. Bloemer, and A. M. Zheltikov. Density of modes and tunneling times in finite one-dimensional photonic crystals: A comprehensive analysis. *Phys. Rev. E*, 70:016612, 2004.